NOTE TO USERS

Characterization of Insulator Layers in Magnetic Tunneling Junctions with Applications in Memory Devices

Ciwei Ren

A Thesis

in

The Department

of

Electrical and Computer Engineering

Presented in Partial Fulfillment of the Requirements
for the Degree of Master of Applied Science at
Concordia University
Montreal, Quebec, Canada

April 2007

Your file Votre référence
ISBN: 978-0-494-34719-5
Our file Notre référence
ISBN: 978-0-494-34719-5

ABSTRACT

Characterization of Insulator Layers in Magnetic Tunneling Junctions with Applications in Memory Devices

Ciwei Ren

Magnetic tunnel junctions (*MTJ*s) are electrical devices that display a large change in resistance when an external magnetic field applied to the junctions. *MTJ*s have applications in non-volatile memory element in Magnetic Random Access Memory (MRAM).

MTJ is composed of two ferromagnetic metallic electrodes and one insulating layer. The insulating layer is inserted in between the two electrodes. When a voltage is applied between the two electrodes, a tunneling current will flow through the insulating layer. An applied magnetic field can change the current direction due to influences on ferromagnetic material causing a change in resistance. The tunneling magnetoresistance (*TMR*) is a measure of the sensitivity of the device to magnetic fields.

It is common that an aluminium oxide (Al_2O_3) tunneling barrier, which is made by oxidation of a thin layer of aluminium (*Al*), is used in most *MTJ*s design. Several oxidation processes have been applied to achieve high quality barrier layers. Typical processes are oxidations in atmosphere, in a pure oxygen environment, oxygen reactive sputtering and RF plasma. By applying these techniques, several groups have reported the *TMR* ratios greater than 30%. The main disadvantage of these processes is that the oxidation rate is very fast, and usually it takes not more than 1~40 seconds to complete the oxidation. It is difficult to control the thickness of oxidation layer, which yields an

Al_2O_3 layer either under-oxidized or over-oxidized.

Aluminium nitride (*AlN*) is an insulating material which can take the place of Al_2O_3 in these devices. The nitridation process of *Al* films is expected to progress much slower than the oxidation process of *Al* films, due to the lower diffusion coefficient of nitrogen in the insulating layer compare to that of oxygen. The research objective of this work is to investigate the effect of nitridation of the insulator layers in MTJ devices. For this, different methods are used to nitridize the insulator layer which is chosen to be as a thin layer of *Al*. The effect of post-processing annealing is also studied. The tunneling junction resistances versus external magnetic field, and tunneling junction I~V characteristic for different samples were measured, compared and discussed. Finally, conclusions are made to compare these techniques with those already available in practise.

Acknowledgements

First of all I would like to thank my supervisor, Dr. Mojtaba Kahrizi, for his helpful advices, comments and supports during my research. Dr. Kahrizi's many insightful discussions during the development of the ideas in this thesis and comments on the thesis are very helpful.

Thanks to Dr. Badilescu for the valuable advice she has given me during this project.

I would also like to thank Mr. Shailesh Prasad and all my colleagues at Concordia University, Micro Devices & Microfabrication lab for their constructive discussions, helps and friendships. It was wonderful to work with them.

I also achnowledge "Le Fonds québécois de la recherche sur la nature et les technologies (FQRNT)" for rewarding me a scholarship for 16 months.

I would like to thank my parents, my wife and my daughter, for their understanding and their supports during my long term studying.

Table of Contents

List of Figures

List of Tables

CHAPTER 1

INTRODUCTION

1.1 Motivation of the Research

With the widely use of portable digital electronics and wireless communication devices, the demand of solid-state memories, concerning the type, speed, size, power consumption and cost, continues to increase.

Researches are working aggressively to address these issues. That is why nowadays there are so many types of memory on the market. Typically they are static random access memory (SRAM), dynamic random access memory (DRAM), and flash memory, ferrorelectric random access memory (FRAM) and magnetoresistive random access memory (MRAM). Among them, MRAM, based on integration of magnetic tunnel junction (*MTJ*) material and complimentary metal oxide semiconductor (CMOS) techniques, has the potential to be competitive with all existing semiconductor memories because of its non-volatile, fast speed and endurance properties.

1.2 Development of Magnetic Memories

"Magnetic memories have existed since the beginning of the computer era. The random access memories (RAM) based on magnetoresistance based on thin film processing were developed in early 1980s. These memories exploited the fact that the resistance of a ferromagnetic conductor depends on the angle between the magnetization and current, an effect called anisotropic magnetization magnetoresistance

(AMR). AMR memories have small resistance change (<2%), which leads to low density and high current demands" [1].

In 1988, much larger magnetoresistance values were observed in multilayered films. This is actually the beginning of giant magnetoresistance (GMR) era. GMR memory is composed by two ferromagnetic layers separated by one nonmagnetic layer. The resistance change for GMR memory is in the range of 4% ~ 8%, which is still too low and limits their application potential.

The development of *MTJ* in 1995 offered MRAM a higher resistance and improved the resistance change. Table 1 shows the features of MRAM compared to several other major memory technologies. Each one of these technologies has some advantages and also some shortcomings. None of them is suitable for several applications.

Table 1 Comparison of current and projected specifications of MRAM to other embedded memory technologies at the 90-nm node [2]

	SRAM	DRAM	FLASH	FRAM	MRAM
Performance (MHz)	50-2,000	20-100	20-100	15-50	**75-125**
Non-volatile	No	No	Yes	Yes	**Yes**
Endurance	$>10^{15}$	$>10^{15}$	$<10^{6}$ write	$<10^{13}$	**$>10^{15}$**
Refresh	No	Yes	No	No	**No**
Cell size (μm^2)	1-1.3	0.25	0.2-0.25	0.4	**0.15-0.25**

The terminologies used in Table 1 are defined as below:

Non-volatile memory is a memory that can retain the stored information even if it is not constantly supplied with electric power. The opposite is random access memory

(RAM), which when the memory power is shut down the stored information are volatised.

Memory endurance failures, caused by trap-up or dielectric breakdown, are the inability of the device to meet its specifications.

In MRAM, the tunneling oxide layer is scaled below ~100 Å, it becomes sensitive to stress. This effect increases greatly as tunnel dielectric thicknesses decrease. The stress can be annealed out at high temperature.

Refresh is a process used to restore the charge in DRAM cells at specific intervals.

Memory cell is a building block of computer memory, which can store one bit information. One memory cell may contain sense circuits to read and write the information, and charge circuit to refresh the information. Smaller memory cell size means more memory cells in a certain size wafer.

Table 1 shows that MRAM has one specific advantage over current types of computer memory: it is non-volatile. This means that, after writing information, no power is needed to keep the information. Using MRAM implies much lower power consumption, which is ideal for personal portable electronics devices. Flash memory is also non-volatile, but is too slow to serve as the working memory of personal computers.

1.3 Structure of the MRAM Cell

Figure 1.1 shows a popular architecture of the MRAM cells design with bits between orthogonal conductors (bit lines, B1 and B2, and digital lines, D1, D2 and D3) and each cell defined as one transistor and one *MTJ*. Bit lines, on top, are contacted

with the top electrodes of the bits. The bottom digital lines are isolated with no contact to any cells. The word lines (W1, W2 and W3) connect to the gate of transistors. When a voltage to a gate of transistor is applied through a word line, a current from a bit line pass through a magnetic tunneling junction forms a current path, so that the corresponding bit state can be sensed [3]. A bit line works with a digital line to switch the magnetic state of the cell on the intersection of these two lines. Only when both of these two lines pass currents, the magnetic state of the cell on the intersection of these two lines will be switched by the direction of the currents.

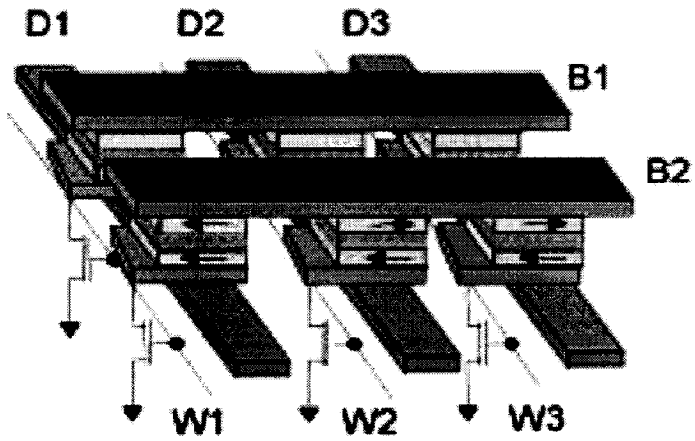

Figure 1.1 MRAM architecture [4]

MTJ material is made of at least two magnetic layers separated by a thin insulating tunnel barrier, usually aluminium oxide (Al_2O_3). The current of the cell flows perpendicular to the film plane via quantum mechanical tunneling through the tunnel barrier. Currently, with the development of the techniques and the materials, such as thin layer deposition technique and using different insulating material layer, the tunneling magnetoresistance (*TMR*) ratio may reach 30% ~ 50% at room temperature.

Figure 1.2 shows an *MTJ* material stack with two ferromagnetic layers (the free layer and the fixed layer) separated by a dielectric barrier (Al_2O_3 and *AlN* in this work) and an additional multilayer structure used to improve the fixed layer performance. The direction of polarization of the upper free layer is used for information storage. The resistance of the memory cell is either low or high depending on the relative magnetization, parallel or anti-parallel, of the free layer with respect to the fix layer. This design requires only the upper free layer magnetization to be reversed for a write operation, while the other layers are fixed. The ruthenium (*Ru*) layer provides very strong anti-ferromagnetic coupling between the fixed layer and pinned layer, creating a three-layer synthetic anti-ferromagnet that results in a magnetically rigid system to help to control the magnetic coupling to the free layer. Pinning is accomplished by using a layer of anti-ferromagnetic material, such as *FeMn* or *IrMn*, with strong exchange coupling to the adjacent ferromagnetic layer to prevent the moment of the fixed layer from switching during write operations [3].

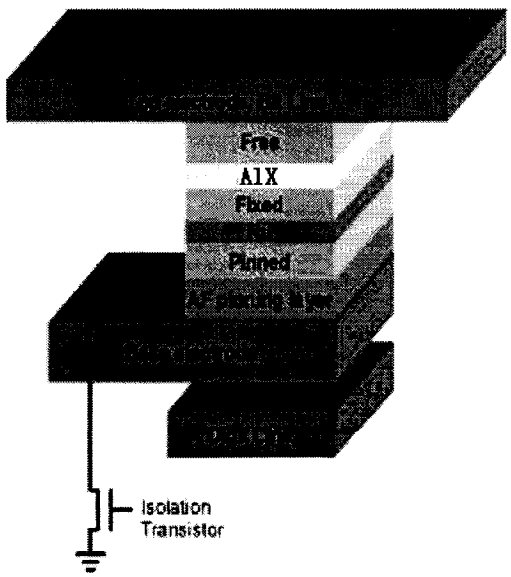

Figure 1.2 A 1T1MTJ MRAM cell [4]

Realizing of magnetic tunneling requires that the free layer shows a maximum rotation of magnetization at the time that the fixed layer shows a minimum rotation.

Consequently, the two layers must greatly differ in transition field. At the present time, the problem is solved by the following methods [5]:

(i) Selecting a suitable combination of two magnetic materials and their respective thicknesses;

(ii) Introducing an additional, anti-ferromagnetic layer (*FeMn*, *IrMn*, *CoO*, etc.) to increase the transition field of one ferromagnetic layer;

(iii) Making magnetic layers with different thickness. The thicker layer will contribute to a higher magnetic field for the same magnetic material.

According to above discussion, Cobalt Iron ($Co_{70}Fe_{30}$) and Nickel Iron ($Ni_{80}Fe_{20}$), two ferromagnetic materials were chosen in this research. $Co_{70}Fe_{30}$ has a stronger magnetic field than $Ni_{80}Fe_{20}$, so $Co_{70}Fe_{30}$ was chosen as a bottom ferromagnet layer and $Ni_{80}Fe_{20}$ was chosen as a top ferromagnet layer.

To maximize the polarization of perpendicular sense current, the insulating layer should be as thin as possible (to increase the tunneling probability), and the ferromagnetic materials should be as thick as possible.

A property that makes a *MTJ* material ideal for MRAM circuits is the resistance that can be adjusted, by adjusting the thickness of the insulating layer, in order to match the circuit's characteristics; the *TMR* ratio of MRAM is much higher than that of GMR. The key challenges for the successful implementation of the *TMR* are: controlling the

resistance uniformity; switching behaviour of magnetic bits; and integration of *MTJ* with standard CMOS technology.

1.4 Research Objectives

Currently, most of *MTJ*s in the market are made using an Al_2O_3 tunneling barrier, which is made by oxidation of a thin layer of aluminium (*Al*). Different oxidation methods have been applied to achieve high quality barrier layers. Typical processes are oxidations in atmosphere, in a pure oxygen environment, oxygen reactive sputtering and RF plasma. By applying these techniques, several groups have reported the *TMR*s ratio greater than 30 %. The disadvantage of these processes is that the rate of oxidation of *Al* is very high, only needs to oxidize for 1 ~ 4 seconds. Therefore, it is hard to control the thickness of the oxidation layer, which makes Al_2O_3 layer either under-oxidized or over-oxidized. The nitridation process of *Al* films is expected to progress much slower than the oxidation process of *Al* films, because of the lower diffusion coefficient of nitrogen in *Al*. One group has reported [6] to use reactive nitrogen sputtering and obtained the *TMR* ratio up to 49 %.

The research objectives of this work are to investigate the different nitridation methods as mentioned in oxidation part and the annealing process, to compare the *TMR* ratio and resistance with those in the oxidation process, and to find if it is possible to replace the Al_2O_3 with *AlN* in MRAM design

1.5 Thesis Outline

This thesis investigates the improvement of the *TMR* ratio using different insulating layers produces different processing techniques.

In Chapter 2, a theoretical approach to *MTJ* is discussed and explained.

Chapter 3 introduces samples preparation, masks preparation and the sputtering system.

Chapter 4 explains the experimental set-up and details on the experiment procedures.

Chapter 5 presents experimental results, characterization of fabricated devices and settings, follows by discussion on results.

Finally, in Chapter 6, conclusions and contributions are highlighted and some of future works to continue this research are suggested.

CHAPTER 2

MAGNETIC TUNNELING JUNCTION

2.1 Quantum Mechanical Tunneling

In classic mechanics the probability that particles with kinetic energy E pass a potential barrier with energy $E_b > E$ is zero. In quantum mechanics, particles, like electrons, have a finite probability of passing a potential barrier; this process is called quantum mechanical tunneling.

The various experimental results involving electromagnetic waves and particles could not be explained by classical laws of physics. Schrodinger equation, incorporated the principles of quanta introduced by Planck, and the wave-particle duality principle introduced by De Broglie, describe the motion of electrons in a crystal by wave theory. The one-dimensional Schrodinger's wave equation is given as [7]:

$$\frac{-\hbar^2}{2m}\cdot\frac{\partial^2\Psi(x,t)}{\partial x^2}+V(x)\Psi(x,t)=j\hbar\frac{\partial\Psi(x,t)}{\partial t} \qquad (2.1)$$

where $\hbar=\frac{h}{2\pi}$, h is Planck's constant, $h=6.625\times10^{-34}\,J-s=4.135\times10^{-15}\,eV-s$, $\Psi(x, t)$ is the wave function, $V(x)$ is the potential function assumed to be independent of time, m is the mass of the particle, and $j=\sqrt{-1}$. The wave function $\Psi(x, t)$ is used to describe the behaviour of the system.

We may determine the time-dependent portion of the wave function and the position-dependent portion of the wave function by using the technique of separation of variables. Assume the wave function can be written in the form

$$\Psi(x,t) = \psi(x)\phi(t)$$

where $\psi(x)$ is a function of the position x only and $\phi(t)$ is a function of time t only.

The solution of the time-dependent portion can be written in the form

$$\phi(t) = e^{-j\frac{\eta}{\hbar}t}$$

where η is called separation constant. We have $E = h\upsilon = \frac{h\omega}{2\pi}$. υ and ω are incident light frequency and angle frequency, respectively. Then $\omega = \frac{\eta}{\hbar} = \frac{E}{\hbar}$. So $E = \eta$.

The total solution can be written in the form

$$\Psi(x,t) = \psi(x)\phi(t) = \psi(x)e^{-j\frac{E}{\hbar}t} \qquad (2.2)$$

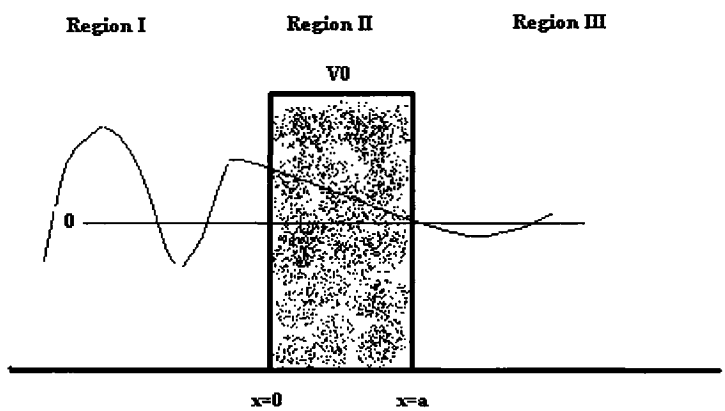

Figure 2.1 A wave function through a potential barrier

In the case when the total energy of an incident particle is $E < V_0$, the potential barrier function is shown in Figure 2.1, incident particles travel from left to the right and pass through the potential barrier. The time-independent wave equation can be written in different regions as follow:

Region I: (Free space) $\frac{\partial^2\psi(x)}{\partial x^2}+\frac{2mE}{\hbar^2}\psi(x)=0$

The solution to this differential equation can be written in the form

$$\psi_I(x)=A_I e^{\frac{jx\sqrt{2mE}}{\hbar}}+B_I e^{-\frac{jx\sqrt{2mE}}{\hbar}} \tag{2.3}$$

Region II: (Potential barrier) $\frac{\partial^2\psi(x)}{\partial x^2}+\frac{2m}{\hbar^2}(E-V_0)\psi(x)=0$

The solution to this differential equation can be written in the form

$$\psi_{II}(x)=A_{II} e^{\frac{x\sqrt{2m(V_0-E)}}{\hbar}}+B_{II} e^{-\frac{x\sqrt{2m(V_0-E)}}{\hbar}} \tag{2.4}$$

Region III: (Free space) $\frac{\partial^2\psi(x)}{\partial x^2}+\frac{2mE}{\hbar^2}\psi(x)=0$

The solution to this differential equation can be written in the form

$$\psi_{III}(x)=A_{III} e^{\frac{jx\sqrt{2mE}}{\hbar}}+B_{III} e^{-\frac{jx\sqrt{2mE}}{\hbar}} \tag{2.5}$$

The coefficient B_{III} in equation above represents a negative traveling wave in region III. However, once the particle incidents into region III, there is no potential to cause a reflection, so B_{III} becomes zero.

There are four boundary conditions for the boundaries at $x = 0$ and $x = a$:

$$\psi_I(0) = \psi_{II}(0)$$

$$\frac{\partial \psi_I(x)}{\partial x}\Big|_{x=0-} = \frac{\partial \psi_{II}(x)}{\partial x}\Big|_{x=0+}$$

$$\psi_{II}(a) = \psi_{III}(a)$$

$$\frac{\partial \psi_{II}(x)}{\partial x}\Big|_{x=a-} = \frac{\partial \psi_{III}(x)}{\partial x}\Big|_{x=a+}$$

Applying these boundary conditions, the equation (2.3), (2.4) and (2.5) can be solved in terms of the coefficient A_I. After solving these equations, the transmission coefficient T can be found as [5]:

$$T = \frac{A_3 \cdot A_3^*}{A_1 \cdot A_1^*}$$

For the special case when $E << V_0$, the transmission coefficient is [5]:

$$T \cong 16\left(\frac{E}{V_0}\right)\left(1-\frac{E}{V_0}\right)e^{-\frac{2a\sqrt{2m(V_0-E)}}{\hbar}} \qquad (2.6)$$

This equation implies that there is a finite probability that a particle penetrating the potential barrier and appearing in region III. This phenomenon is called tunneling.

In general, a tunneling device consists of two metal electrodes, separated by an insulating barrier layer, as shown in Figure 2.2. If a voltage V is applied over the electrodes, the tunnel current flows from the right electrode to the left electrode.

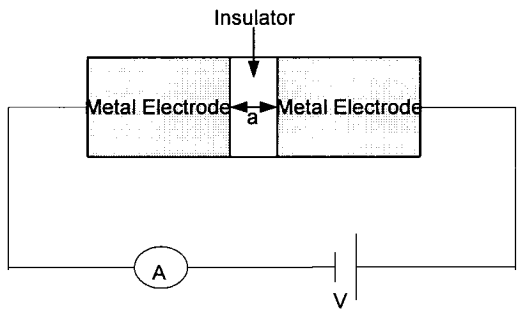

Figure 2.2 A metal-insulator-metal sandwich device

Using some approximations, the tunneling current at low temperature (T = 4.7K) with a biasing voltage (V) through an arbitrary barrier with an average height of ϕ and thickness a [8]:

$$J = J_0\{(\phi - V/2)\exp[-A(\phi - V/2)^{1/2}] - (\phi + V/2)\exp[-A(\phi + V/2)^{1/2}]\} \quad (2.7)$$

where J is the tunneling current density, V is the biasing voltage, $J_0 = (e^2/2\pi h)a^{-2}$ and $A = (4\pi a/h)(2m_e^*)^{1/2}$ are constants, e is the charge of an electron $(=1.6\times10^{-19} coulomb)$ and m_e^* is the electron effective mass. The low temperature is to make sure that thermal current could be neglected and to restrict the electron transport between electrodes to

the tunnel effect. This formula shows that the tunneling current increases with increasing voltage exponentially. At very low biasing voltage, equation (2.7) is simplified as:

$$J = J_0 V(A\phi^{1/2}/2 - 1)\exp(-A\phi^{1/2}) \tag{2.8}$$

The relationship between the biasing voltage and the tunneling current is linear at low biasing voltage.

2.2 Spin-dependent Tunneling

In magnetic tunnel junctions, say, sandwiches of the type F/I/F, where F stands for a ferromagnetic electrode and I for the insulating barrier, Jullière [10] for the first time in 1975 showed a large change of resistance of the junction by applying a magnetic field. It was shown that the tunneling current should depend on the relative orientation of the magnetizations of the two ferromagnetic electrodes. By applying an external magnetic field, one can modify the magnetizations angle between two ferromagnetic electrodes, which can give rise to a large magnetoresistance in tunneling junction [9].

If the electrodes are made of different ferromagnetic materials, such as Cobalt *(Co), Nickel (Ni), Iron (Fe)*, or of their alloys, the density of states for spin-up electrons and spin-down electrons are in general not equal, resulting in different up- and down-currents through the barrier. Jullière introduced a simple model to discuss the concept of spin-dependent tunneling [10]. In his model he assumed that the tunneling current is proportional to the density of states at the Fermi-level of each electrode. The energy

bands for the two spin-directions in a ferromagnetic material are different, which results in different densities of states at the Fermi level for spin up $(N\uparrow)$ and spin down $(N\downarrow)$ spin electrons, as shown in Figure 2.3.

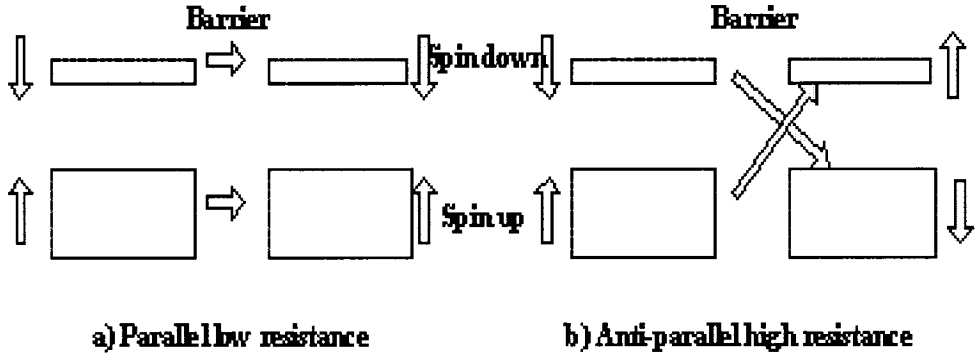

Figure 2.3 Simplified density of states diagram for an *MTJ* showing the transportation of the electrons. The resistance is low or high when the magnetic moments of the two layers are: (a) parallel or (b) anti-parallel. The majority band is in horizontal line (--) and the minority band is in vertical line (|). The arrows in (a) and (b) represents the current of electrons tunneling from the left electrode to the right electrode through a barrier.

For a normal tunneling process, like one in Figure 2.2, there are no spin-flip scattering mechanisms so the spin is conserved and the spin up/down electrons from one electrode must tunnel into the same states available in the other electrode. When a magnetic field is applied, the magnetizations of the layers are parallel, Figure 2.3 (a), the majority/minority band electrons tunnel across to the majority/minority band of the opposing electrode. When they are anti-parallel, Figure 2.3 (b), the majority/minority band electrons are forced to tunnel into the minority/majority band of the opposing electrode. The reduced number of states available for tunneling between the ferromagnetic layers when the layers are anti-parallel results in an increased tunneling resistance compared to when they are parallel. The higher *TMR* ratios (will be defined later in this section) are obtained with materials that have a greater imbalance in the

density of states at the Fermi-level. This imbalance is described by the spin polarization. The spin polarization P is defined as [9]:

$$P = \frac{N\uparrow - N\downarrow}{N\uparrow + N\downarrow}$$

where $N\uparrow$ and $N\downarrow$ are the densities of states at the Fermi level for spin up and spin down electrons.

The value of the polarization depends on the electrode material. The density of states in one electrode can be changed by switching the magnetic field direction of the electrode, giving rise to two situations: the magnetizations of the two electrodes are parallel or anti-parallel. The total current through the barrier can be calculated for each situation [9]:

$$a) I_{\uparrow\uparrow} \propto N\uparrow N\uparrow + N\downarrow N\downarrow = N\uparrow^2 + N\downarrow^2$$
$$b) I_{\uparrow\downarrow} \propto N\uparrow N\downarrow + N\uparrow N\downarrow = 2N\uparrow N\downarrow$$

where $I_{\uparrow\uparrow}$ and $I_{\uparrow\downarrow}$ are two tunnel currents caused by parallel and anti-parallel states, respectively. If $N\uparrow$ and $N\downarrow$ are unequal, these two tunnel currents are unequal. Thus, a change of the magnetization of one of the electrodes will result in a different current and hence a different resistance. A measure of the relative change in resistance, the tunneling magnetoresistance (*TMR*), is defined as [9]:

$$TMR \equiv \frac{R_{\uparrow\downarrow} - R_{\uparrow\uparrow}}{R_{\uparrow\uparrow}} = \frac{I_{\uparrow\uparrow} - I_{\uparrow\downarrow}}{I_{\uparrow\downarrow}} = \frac{2P_1P_2}{1 - P_1P_2} \qquad (2.9)$$

where P_1 and P_2 are the material polarization values in electrode 1 and 2, respectively. $R_{\uparrow\downarrow}$ and $R_{\uparrow\uparrow}$ are the magnetoresistance when the magnetic states in two ferromagnet electrodes are anti-parallel and parallel, respectively.

Many factors affecting the *TMR* ratio, such as the interfacial effect, are not yet been fully understood due to difficulties in fabricating and controlling the quality of the tunneling junctions. Impurities in the insulator or at the insulator–ferromagnet interface represent an important effect. The presence of impurities, such as *Co*, *Ni*, copper (*Cu*), and lead (*Pd*) based ions, in the insulating layer of Co/Al_2O_3 $/Ni_{80}Fe_{20}$ tunneling junctions has been reported to cause a reduction of the *TMR* ratio, due to the spin scattering. Another important interfacial effect is the increased polarization of ferromagnet (*FM*) electrodes by adding high-polarization materials at the insulator–ferromagnet interface. This increase follows from the influence of the ferromagnet-insulator coupling on the effective polarization of the *FM* electrode. A higher polarization value of the additional interlayer yields a higher effective polarization value of the ferromagnet electrode, and therefore a higher *TMR* ratio. E. Snoeck *et al.* [11] have reported an increase in the *TMR* ratio by up to 1.25 times by adding *Fe*-based ions in the insulator of tunneling junctions. According to the above formula, we need high spin polarization materials in order to get a higher *TMR*.

Table 2 shows the Curie temperature[1] and the spin polarization of *Fe, Co, Ni* and $Fe_{50}Co_{50}$. These magnetic materials and their alloys are commonly used as ferromagnetic electrodes in the research. In the tunneling process, it is assumed that this

[1]**Curie temperature, T_c**, of a ferromagnetic material, is the temperature above which it loses its characteristic ferromagnetic ability.

spin-polarization is completely conserved. Higher polarization value means a large difference in the densities of states of spin up and spin down electrons, which causes a large *TMR* ratio.

Table 2 Curie temperatures and spin polarizations of *Fe*, *Co*, *Ni* and *CoFe* [12] [13]

	Tc (K)	P
Fe	1044	44%
Co	1388	34% ~ 45%
Ni	628	33%
CoFe	N/A	47% ~ 53%

2.3 Magnetic Tunnel Junction Structure

A schematic draw of a magnetic tunnel junction is shown in Figure 2.4.

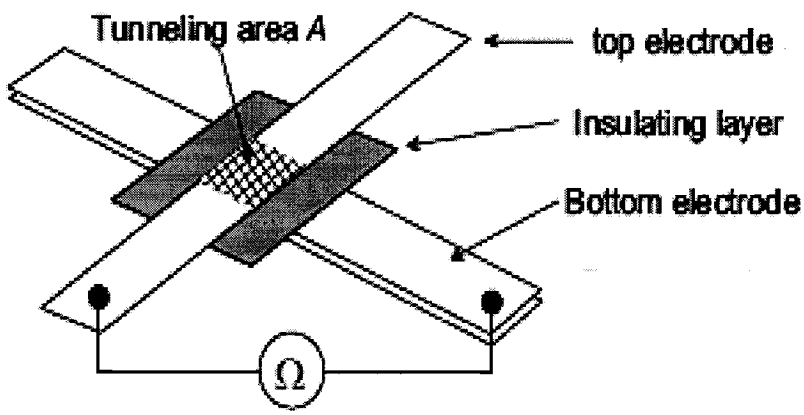

Figure 2.4 A simple *MTJ* structure [14]

On a clean silicon substrate, the bottom electrode (bottom ferromagnetic layer), including the buffer layer, is grown. The buffer layer, which is usually grown on the substrate to improve the adhesion of bottom electrode and makes the bottom electrode layer and silicon wafer well bonded, is an insert layer and is not shown in the diagram. The typical thickness of the buffer layer is 10 to 15 nm. Then the insulating layer is deposited, covering the bottom electrodes and finally, the top electrode is grown.

The insulating layer, Al_2O_3 or *AlN* in this research, can be created by two methods. The first method consists of the deposition of a thin *Al* layer and subsequent oxidation or nitridation of the layer. The oxidation can be done in air or in a pure oxygen environment. The nitridation can only be done in a pure nitrogen environment. The second method involves direct deposition, for instance, by reactive sputtering.

The tunneling barrier is the most important part in *MTJ*. The following issues must be taken into consideration during the fabrication of *MTJ*:

- The barrier must be homogeneous, without pinholes or impurities.
- The barrier must be smooth. Roughness of the thickness can cause inhomogeneous currents through the layer that can lead to local heating and breakdown of the barrier, creating a short circuit.
- The roughness of the barrier can cause a magnetic coupling problem between the two electrodes.
- The flatness at the interface between ferromagnetic electrode and insulating barrier affects the *TMR* ratio.

To prevent shortings between two ferromagnet electrodes, produced by pinholes in the insulating layer, the samples were oxidized or nitridized at room temperature, in dry

oxygen or nitrogen, after *Al* deposition. Dry oxidation and nitridation give a denser and higher quality layer than those of wet processing.

In addition to the tunneling barrier height and thickness, the area of the barrier influences the resistance of the tunnel junction as well, but this parameter will not be considered.

The non-volatile memory cell used in this work can store one bit of information without the necessity of refreshment to retain its state.

The structures of the two electrodes and of the barrier layer were done by photolithography masks pattern in the Micro Devices & Microfabrication Lab at ECE Department in Concordia University.

CHAPTER 3

EXPERIMENTAL BASICS AND SET-UPS

3.1 Literature Survey

E. Y. Chen *et al.* [8] compared the different oxidation methods, like thermal oxidation, reactive sputtering and plasma oxidation, for producing *MTJ*. They demonstrated that these different oxidation techniques can be used to produce *MTJ* material and *Al* metal film uniformity is critical to produce *MTJ* with uniform resistance across a large size wafer [8].

In plasma oxidation, oxygen plasma is exposed to a pre-deposited *Al* metal layer. This method has been widely used because it gives a uniform Al_2O_3 layer in a short oxidation time and, at the same time, high tunneling magnetoresistance (*TMR*). The problems caused by the plasma oxidation are the fabricated junctions have a high resistance area product (RA) value and the bottom ferromagnetic layer is easy to be oxidized [15]. Because of these shortcomings, plasma oxidation method is not considered in this research. Only thermal oxidation and reactive sputtering techniques are implemented in this research.

The diffusion coefficient of oxygen in an aluminium layer is higher than that of nitrogen (see Appendix C). To reduce the over-oxidation or under-oxidation of the bottom electrode, Satoru Yoshimura *et al.* [6] used nitridation to process an *Al* layer and compared the results with the oxidation process in microwave-excited plasma. They concluded that the optimized nitridation condition is less sensitive to the thickness of the *Al* layer compare to the oxidization process. In other words, the plasma nitridation

process provides a wider controllability compared to the oxidization process for ultra-thin barrier formation in *MTJ*s [16].

In this work, thermal nitridation and nitrogen reactive sputtering methods are used to compare with the aluminium oxidation using the same methods.

3.2 Samples and Masks Preparation

3.2.1 Samples preparation

Magnetic tunneling junctions are layered structures, deposited on a piece of clean silicon (*Si*) substrate. The substrate must be non-conducting to eliminate the parasitic current through the substrate, and for this purpose N-type doped silicon (100) wafers with high resistivity were chosen. Silicon samples are cut in 1" x 1" squares.

To remove dust, sodium, metal, native oxide and grease, which are the most known types of unwanted impurity contaminants during storage or fabrication, a cleaning process was applied to remove the surface contaminations. This cleaning process is done in following four steps:

1) In order to remove dust, sodium and organic contaminants, samples were boiled in 1:1 H_2SO_4:H_2O_2 solution for five minutes, then rinsed in de-ionized water;

2) In order to remove metallic contaminants, samples were boiled in 1:1:5 HCl:H_2O_2:H_2O solution for five minutes, then rinsed in de-ionized water;

3) In order to remove native oxide, samples were dipped in 1:50 HF:H_2O solution for 30 seconds, then rinsed in de-ionized water;

4) In order to remove particular contaminants, such as gold (*Au*), silver (*Ag*), *Cu*, *Ni*, etc., samples were kept in 1:1:5 $NH_4OH:H_2O_2:H_2O$ hot solution for five minutes, then rinsed in de-ionized water [17];

5) Blow-dry the samples with nitrogen gas to avoid silicon oxidation.

After the cleaning process, all the samples were stored in a clean vacuum box for future use.

3.2.2 Masks preparation

MTJ masks designs were done by Cadence software (CMOSIS5). There are six junctions on each sample. Figure 3.1 (a) shows the bottom electrodes and Figure 3.1 (b) shows the six junctions. The junction area is 150 μm × 300 μm. Figure 3.1 (c) shows the top electrodes and (d) shows the contacts, which are 1.4 mm × 1.4 mm in size. The dark part will block the ultra-violet (UV) light; while the white part will let the UV light pass through. The detail photolithography and UV alignment processes are explained in Chapter 4.

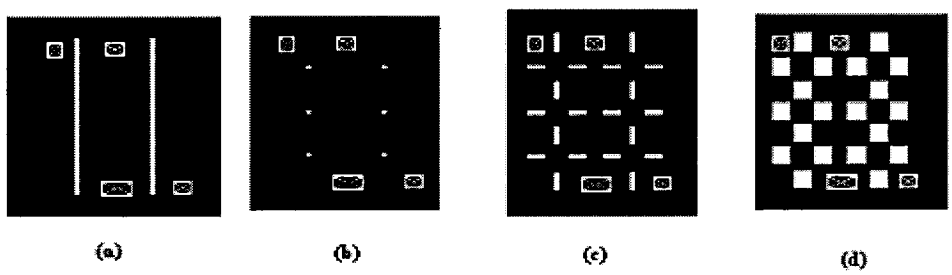

Figure 3.1 Masks design for the experimental
(a) bottom electrodes; (b) junctions; (c) top electrodes; (d) metal contacts

The designs were printed on a transparency. Masks were prepared in a dark room by using fixer and developer. All these steps are done in the Micro Devices & Microfabrication Lab.

3.3 Sputtering System Setting

A sputtering system, "MagSput-2G2" containing the two magnetron sputtering guns shown in Figure 3.2, is used in *MTJ*s fabrication. The system can be switched between DC and RF plasma. It has the capability to sputter different metals as well as insulators and semiconductors such as ceramics, silicon, and piezoelectric material. By varying the applied DC voltage and the current, power applied on the target can be controlled and varied. RF power is adjusted and tuned on panel. A quartz crystal monitor is used to measure the sputtering rate and film thickness. The resolution of the monitor is up to 0.1 angstrom (1 Å = 10^{-9} m).

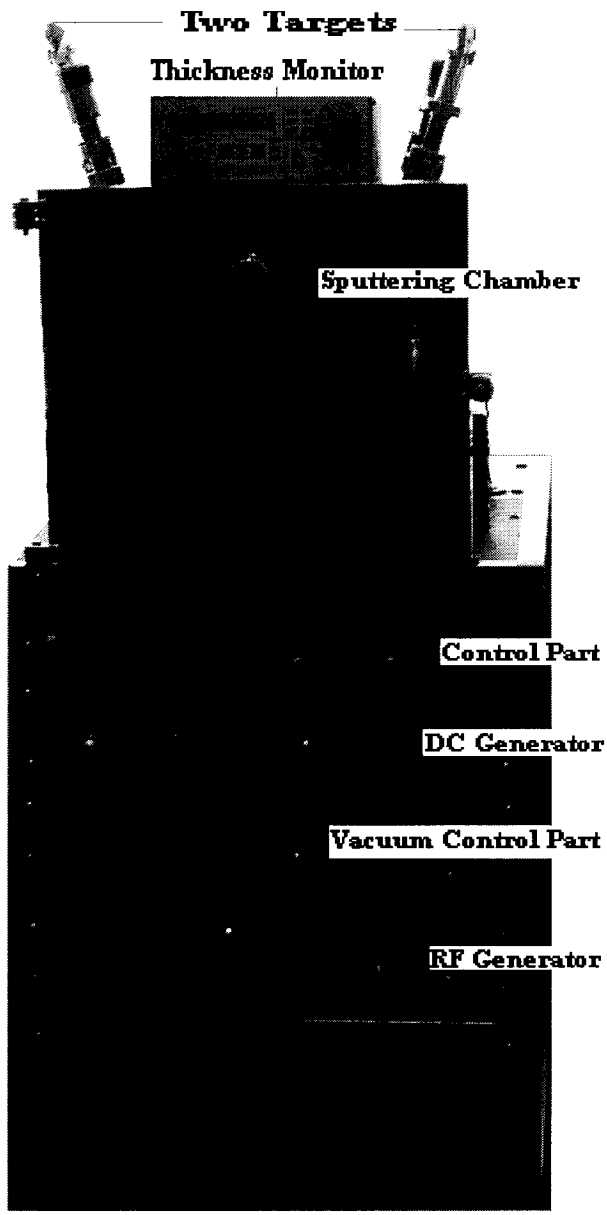

Figure 3.2 "MagSput-2G2" sputtering system

3.3.1 Principle of the sputtering

Sputtering is a physical process where atoms from a target material are stroked into the gas phase due to the bombardment of the material by energetic ions. It is commonly used for thin film deposition. Figure 3.3 shows the schematic diagram of the DC sputtering process.

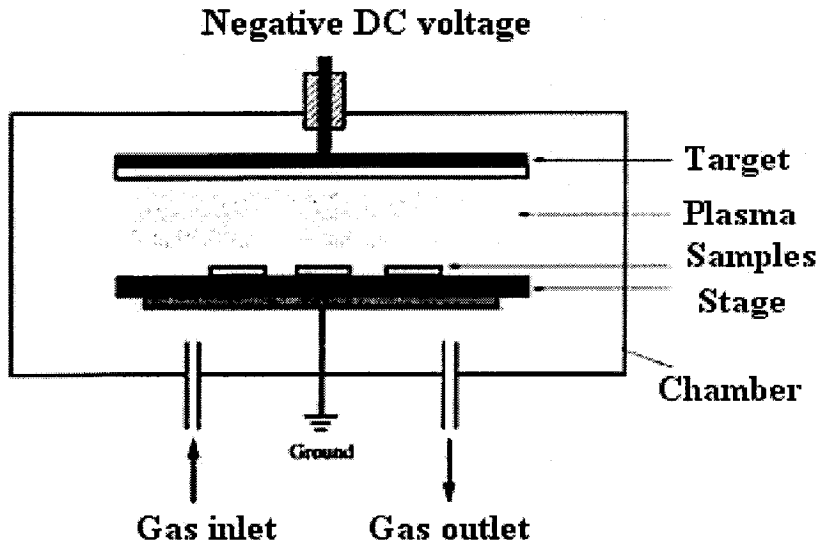

Figure 3.3 Schematic diagram of DC sputtering system [18]

In the sputtering system, an inert gas, such as argon gas in this research, is fed into the chamber at low pressure. A high negative voltage, from several hundred to several thousand volts, is applied on a top electrode (target). There are always some argon ions available in the gas chamber. Attracted by the high negative voltage, the positive argon ions are accelerated towards the target and strike the target material producing secondary electrons. These electrons bombard the argon atoms and cause a further ionization of the gas to sustain the plasma. The plasma contains argon atoms, and positive and negative ions. The target material is the source material to be deposited. The bottom stage and chamber are both grounded. The atoms extracted by argon ions, then travel through the plasma and strike the surface of the wafers and form the deposited film. The process is realized in a closed chamber, in which a high vacuum is made before the sputtering starts [18].

The chamber pressure p and the target to substrate distance d determine a break-

through voltage U_D following the equation $U_D = \frac{A \cdot p \cdot d}{\ln(p \cdot d) + B}$ [19]. Here A and B are material constants. The ionization probability increases with an increase in pressure and causes to increase the number of ions and the conductivity of the gas, and the break through voltage drops.

To increase the gas ionization rate, a ring magnet behind the target, called magnetron sputtering, is used, as shown in Figure 3.4. The electrons in the magnetic field are trapped over the target surface. They cause a higher ionization probability and hence form a plasma ignition at low pressures, which can be up to one hundred times smaller than for conventional sputtering. On the other hand, the lower pressure will cause less collision for the sputtered atoms on their way to the substrate, and higher deposition rates can be realized thereby.

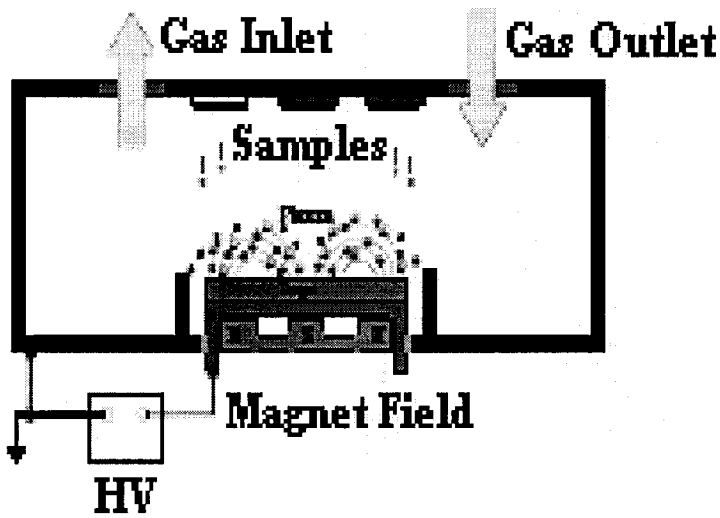

Figure 3.4 Magnetron sputtering system [19]

The bombardment of a non-conducting target with positive ions would lead to an

accumulation of positive charge on the target and subsequently to a shielding of the electrical field. Therefore the DC sputtering is restricted to conducting materials.

For reactive sputtering other gases like oxygen or nitrogen are mixed with the argon gas first, and then fed into the sputter chamber to produce oxide or nitride films.

3.3.2 The sputter parameters

The resulting film properties can be controlled mainly by the following parameters:

The sputter current determines mainly the deposition rate. Increasing the sputter current will result in an increase of the deposition rate.

The applied voltage determines the maximum energy with which sputtered particles can escape from the target. The applied voltage determines also the sputter yield, which is the number of sputtered particles per incoming ion. According to the suggestion of the manufacturer of the sputtering system, the applied voltage is always set to 1 kV. By adjusting the sputter current, the applied energy can be changed easily.

The pressure in the chamber determines the mean free path for the sputtered material. The mean free path is defined as the average distance the particle travels between collisions with other particles. Lower pressure means less particles inside the chamber, hence fewer collisions occur for the particles on their way from the target to the substrate. The low gas pressure also avoids the gas contamination of the sample.

The gas flow rate, which controls the argon gas flow, will affect the chamber pressure. The maximum gas flow rate in the sputtering system is 50 Cubic Centimetres per Minute (*CCM*). Decreasing the gas flow rate will decrease the chamber pressure and results in a high sputtering rate. There is a lower limit for the gas flow rate for a certain material. If the flow rate is too low, there are not enough particles inside the chamber.

The electrons from the target may have a lower probability to bombard the argon atom and cause a further ionization of the argon gas to sustain the plasma. The lowest gas flow rate in our system was found to be 10 *CCM* for *Al* sputtering. Once the gas flow rate is less than 10 *CCM*, the plasma diminishes very quickly. Although the gas low flow rate has a lot of benefits (low contamination, high sputtering rate and fine surface structure, etc.), sometime a higher gas flow rate is needed. In *Cu*, *Al* and *Ti* sputtering, a lower gas flow rate is used, while in $Co_{70}Fe_{30}$ and $Ni_{80}Fe_{20}$ sputtering, a higher gas flow rate is used as explained in Chapter 4.

The rotation of the substrate stage (discussed in Chapter 4), the substrate temperature and the deposition angle between substrate and target surface also affect structure of the sputtered film.

In conclusion, all the parameters such as the sputter current, the applied voltage, the pressure, and the gas flow rate, the rotation of the substrate stage, the substrate temperature and the deposition angle parameters affect the sputtering rate and the final film structure. In this research, the effects of all these parameters except the substrate temperature and the deposition angle have been studied, because these two parameters are fixed by the system manufacturer.

3.3.3 Introduction to "MagSput-2G2" sputtering system

In "MagSput-2G2" sputtering system, two targets are installed on two magnetron guns. Thus two layers or even three layers can be sputtered without breaking the vacuum. Two targets are mechanically bonded to cathodes, ensuring both electrical and thermal contact. During the sputtering, the target temperature reaches several hundred degrees; and this temperature can damage the insulate o-ring inside the cathode and

even deform the thin target. The cathodes and the targets are cooled by a water chiller to ensure they may not be damaged by the heat.

The substrate stage may be rotated. The stage is 5" in diameter, a large number of samples can be coated on it under highly reproducible conditions. The distance between target and substrate stage is fixed. To increase the sputtering rate, the distance is a very important parameter.

The sputtering rate and film thickness are measured using the FTM-2000 Rate/Thickness Monitor made by *Torr International Inc.* The instrument uses a proven quartz crystal sensor technology to measure the rate and the thickness in thin film disposition processes.

A high voltage power supply with arc suppression produced by *Glassman High Voltage Inc.* is used to apply high voltages (up to -1000 V / 600 mA) to the target. The films were produced in a constant current mode.

The base pressure of the chamber is $10^{-6} Torr$. A full range vacuum gauge to measure 760 to $10^{-8} Torr$ with all the controls interlock is used. All the input gases, such as argon, oxygen and nitrogen, are set at 14 to 16 pounds per square inch (psi). Additionally, the gas composition in the chamber can be monitored by a mass flow meter to determine the influence on the film growth.

Although the sputtering system vacuum is designed down to $10^{-8} Torr$, S. Miura *et al.* [20] have shown that the highest *TMR* ratio appears when the pressure of the sputtering chamber is $10^{-5} Torr$. The *TMR* ratio, which is about 10% when the pressure is lower than $10^{-7} Torr$, gradually increases with the increase of pressure and reaches a peak value of 27% at $P = 10^{-5} Torr$, and then reduces abruptly beyond $P = 10^{-4} Torr$.

To achieve a higher *TMR* ratio, the pressure of the sputtering chamber is maintained at $P = 3 \times 10^{-5} Torr$ in this research.

CHAPTER 4

EXPERIMENTS

4.1 Experimental Set-up

The magnetic tunneling junctions of *Si/Ti (10 nm)/Cu (100 nm)/*$Co_{80}Fe_{20}$ *(15 ~20 nm)/Al-X (~2.0 nm) /*$Ni_{70}Fe_{30}$ *(15~20 nm)* layers were prepared on a clean N-type (100) *Si* wafer and as it is shown in Figure 4.1. The masks and silicon wafers were prepared in the Micro Devices & Microfabrication Lab. Using four-step cleaning procedures, dusts, native silicon dioxide layer and of all contaminants were removed from the Si surface.

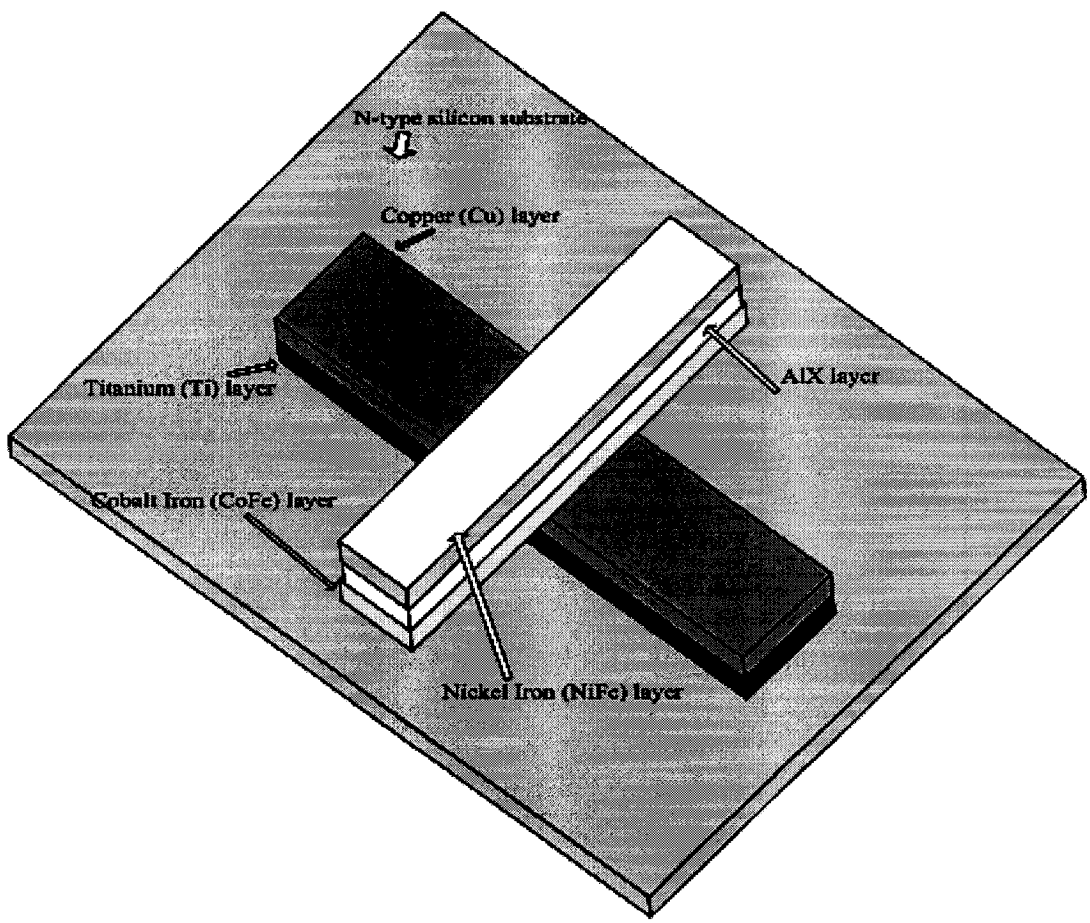

Figure 4.1 Composition of a single *MTJ*

4.1.1 Surface roughness

Transport between two metallic electrodes can be roughly classified into two types: tunneling and contacting.

When the separation of the two electrodes is in a few angstroms, electrons move between the electrodes by tunneling. The probability that an electron tunnels through a barrier of height V with barrier thickness a is given by [21]:

$$P(probability) \sim \exp\left[-c\frac{\sqrt{2mV}}{\hbar}a\right] \tag{4.1}$$

where c is a constant in order of unity, which depends on the shape of the barrier and the electronic wave-functions, usually takes 1 or 2, m is the mass of electron. Generally, a barrier is created by inserting an insulating layer between the two electrodes. In this case, the barrier height depends on the position of the edges of the gap of the insulating material with respect to the Fermi level of the electrodes.

According to the above formula, the tunneling probability decreases exponentially as the barrier height increases. A change of a few angstroms can greatly modify the tunneling probability. The conductance (G) between two ferromagnet electrodes is given by [21]:

$$G \sim \frac{e^2}{h}P \tag{4.2}$$

Base on what was explained above, the surface flatness of the insulating layer is crucial for the resistance measurement. Even a few angstroms difference, the resistance will have an exponential change. Figure 4.2 shows two surfaces measured by an optical imaging profilemeter. Figure 4.2 (a) shows a sample sputtered with the substrate stage without rotation, while Figure 4.2 (b) shows a sample sputtered with the substrate stage rotated at 20 rotations per minute (RPM). The lower level in Figure 4.2 is the silicon wafer, which seems to be very smooth. The top level is *Cu* which its surface becomes smooth when the stage is rotated (Figure 4.2 (b)), which leads to a uniform resistivity. Therefore, the rotation of the substrate stage is crucial for uniformity of the sputtered surface. At a high speed rotation, the sputtered surface is even more uniform. In the following experiments, the substrate was rotated at higher speed (40 RPM) except in the case of $Co_{80}Fe_{20}$ and $Ni_{70}Fe_{30}$ layers sputtering.

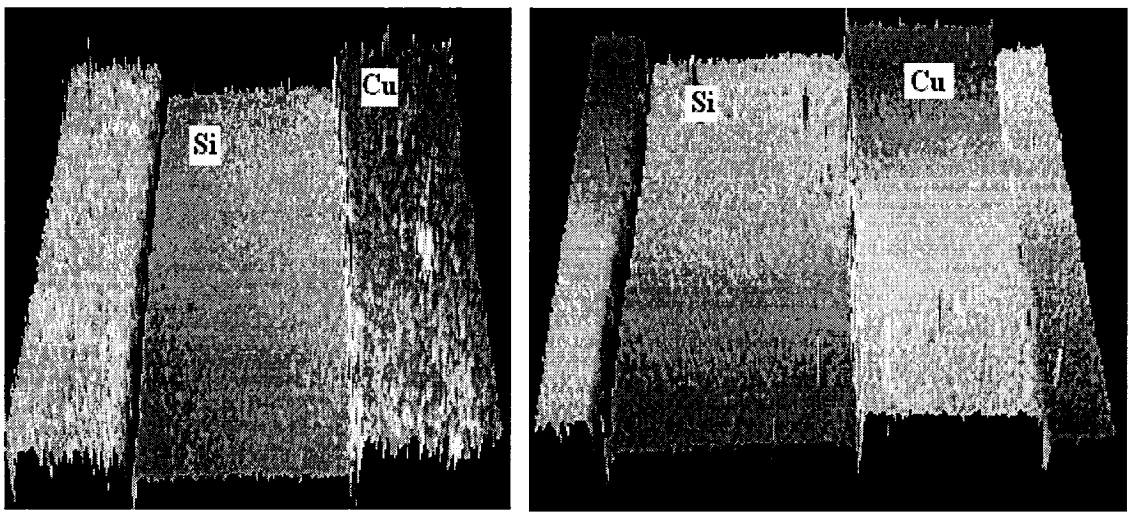

(a) (b)

Figure 4.2 Surface roughness measured by an optical profilemeter (a) substrate with no rotation (b) substrate rotated at 20 RPM

4.1.2 Bottom electrode layer processing

First, *Cu* is used as a bottom electrode and sputtered on a cleaned *Si* wafer. Then $Co_{80}Fe_{20}$ is sputtered on *Cu*. Observing through an optical imaging profilemeter, the *Cu* layer appeared etched by the $Co_{80}Fe_{20}$. The *Cu* layer can be easily removed by touching. The cause of this problem is because the *Cu* layer and the *Si* surface are not well bonded, and the $Co_{80}Fe_{20}$ is a very hard material. Once the high energy $Co_{80}Fe_{20}$ atoms reach the *Cu* surface, they strike the *Cu* atoms off the silicon surface, like an etching process. To make the *Cu* layer and the *Si* surface well bonded, an annealing process was performed right after the *Cu* layer was sputtered. The annealing process was performed in nitrogen environment to avoid *Cu* oxidation. *Cu* can be annealed below the eutectic point[2]. The eutectic point for *Cu* and *Si* is 805°C. The annealing was done at different temperatures of 800°C, 400°C, 200°C and 100°C; the resistance of the *Cu* layer after annealing was measured to be >1MΩ, ~ 1MΩ, 5.7Ω and 32.5Ω, respectively. Although a reasonable resistance was achieved after the annealing process, the adhesion of the *Cu* and the *Si* wafer did not seem to be good enough. This could be observed after the $Co_{80}Fe_{20}$ sputtering. Another consideration for the tunneling junction annealing temperature is the Curie temperature as mentioned in Table 2. The annealing temperature must below the Curie temperature to avoid the ferromagnetic materials lose its ferromagnetic ability. Since annealing at 200°C achieved a lowest resistance, this temperature was used as annealing temperature in the following experiments.

Control of the adhesion between a thin film and its substrate is crucial to the yield, performance, and reliability of devices in microelectronics fabrication. Titanium (*Ti*)

[2] **Eutectic point**: The composition of a liquid phase in invariant equilibrium with two or more solid phases. (Definition ©1989 CRC Press LLC)

and Tantalum (*Ta*) both are able to make a very good bonding with the *Si* surface. The use of *Ti* as a good adhesive between the *Si* wafer and *Au* layer has been reported [22]. However *Ti* is oxidizes easily in air. Usually *Au* sputtering is done *in situ* after *Ti* sputtered. In this work, we used *Ti* as a buffer layer between *Si* and *Cu* layers to perform the experiment.

First, 10nm *Ti* layer is deposited on cleaning *Si* wafers, and then 100nm *Cu* layer is sputtered on the *Ti* layer. Next, one wafer is kept in a vacuum chamber for future comparison; the other wafer was annealed at 200°C for 15 minutes in a nitrogen environment and then cooled down to the room temperature. Comparing these two wafers showed that the surface of the copper layer on the annealed wafer became very hard (the copper layer is harder to scratch by steel tweeze), well adhesive, and with lower resistance (3 ~ 6 Ω).

4.1.3 Applying masks on samples

To deposit the bottom electrode, a mask should be applied to a *Si* wafer. Applying the first mask, we have the freedom to put the mask anywhere on the wafer, while the following masks should be aligned with the first one. As the mask aligning marks were design on each mask as shown in Figure 3.1. Using several steps (Figure 4.3) of photolithography and ultraviolet (UV) mask exposure, the shape of the bottom electrode pattern were printed on the surface of the wafer, ready for sputtering.

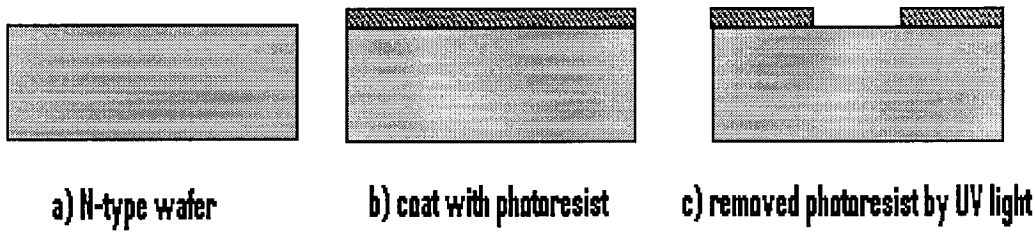

Figure 4.3 Process steps for photolithography and UV expose

The procedures for the photolithography process and UV exposure are shown below:

- Secure the sample on the spinner (Figure 4.3 (a));
- Clean the sample with nitrogen gas and turn on the spinner at 3000 RPM;
- Deposit 3 ~ 5 drops of photoresistive on the sample and let it spin for 30 seconds (Figure 4.3 (b));
- Put the sample in a force convection oven at 110°C for 30 minutes "soft bake";
- Expose the sample to UV light for 10 seconds under a certain mask;
- Put the sample in a developer solution for 1 minute; a pattern is displayed on the sample (Figure 4.3 (c));
- Rinse the sample in de-ionized (DI) water and dry it with nitrogen gas;
- Put the sample in a force convection oven at 110°C for 30 minutes "hard bake".

These procedures are repeated each time when a new mask is applied. "Soft bake" and "hard bake" are to make the photoresistive stronger to avoid scratch during the mask align and sputtering processes. To remove the remaining photoresistive, the sample was put into acetone solution (acetone will remove the photoresistive), cleaned with DI water and dried with nitrogen gas.

4.2 Experiment Procedures

4.2.1 Pre-sputtering cleaning

Before sputtering, the sputtering chamber is cleaned with acetone solution, and then kept under vacuum, inert gas flowed and plasma etched several times to reduce contamination from the chamber and target.

To prepare a system for sputtering deposition, one should run the system without the substrate exactly the same way as run the system with a substrate. This sort of precondition-running has following beneficial effects:

(1) The target surface layer is etched and cleaned;

(2) Chamber and fixtures are outgased by bombardment;

(3) Chamber and fixtures are coated with the material to be deposited, minimizing subsequent contamination.

The walls inside the chamber need to be cleaned regularly with isopropyl alcohol after removal of the deposits by scrubbing, if necessary. The chamber has to be kept under vacuum when is not in use. This will help in restarting and achieving a good performance for the subsequent depositions.

4.2.2 Sputtering procedures

Once the system is cleaned, it is ready for the sputtering. The following procedures have followed.

- Turn on the system main power, start flow the nitrogen gas to open the chamber door and put the sample inside the chamber;

- Close the chamber door by hand and turn on the mechanical pump; once the pump is on, inside pressure is lower, the chamber door is closed firmly;
- When the chamber pressure reaches below $3\times10^{-3}Torr$, start a water chiller and the diffusion pump to obtain a high vacuum (The water chiller will cool the diffusion pump and the targets);
- When the chamber pressure reaches $3\times10^{-5}Torr$; apply a high negative voltage to the target; set the sputter current to the middle; start the rotation of substrate stage;
- Turn on the argon gas and start flowing, plasma can be observed. Adjust a proper current and flow rate to get a stable plasma;
- Open the target shuttle, in order to allow plasma to reach the substrate. The sputtering rate and the film thickness can be read from the thickness monitor;
- Once the sample reaches the required thickness, close the target shuttle, the argon gas, high voltage supply, pumps and main power supply to stop the system.

These are the typical procedures for sputtering of one layer. To deposit a second layer *in situ*, simply apply the high voltage to the second target and start flowing argon gas. Plasma will generate automatically. Vacuum pumping usually takes 30 minutes for the mechanical pump and 90 minutes for the diffusion pump.

4.2.3 Soft materials sputtering

Table 3 shows the hardness of some materials used in this research. *Al* and *Cu* are soft material, which are easy to sputter. *Co*, *Ni*, *Fe* and *Ti* are hard material. They are

difficult to sputter. *Co*, *Ni* and *Fe* are ferromagnetic material, which may cause the magnetic field cancellation and make the sputtering rate very low (will discuss in section 4.3). In our designs since *Cu* is a bottom electrode, its thickness will not affect the final results.

Table 3 Materials hardness [23]

Material	Aluminium (*Al*)	Cobalt (*Co*)	Copper (*Cu*)	Nickel (*Ni*)	Iron (*Fe*)	Titanium (*Ti*)
Mohs Hardness[3]	2.75	5.0	3.0	4.0	4.0	6.0

Al layer thickness has an important effect on the final result. After the sputtering, it will be oxidized or nitridized as an insulating layer. Also, as we mentioned before (Equation 4.1 and 4.2) the relationship between the conductivity of the tunneling layer and the thickness of the layer is exponential. A change of a few angstroms can greatly modify the tunneling resistance. The sputtering rate for *Al* is 40 ~ 80 nm per minute in a normal operation. It is very difficult to control the sputter of 1.5 nm in a short time.

Many experiments were performed to reduce the *Al* sputtering rate. The sputtering current, the gas flow rate, the negative sputtering voltage and the sample-target distance are parameters which control the rate of deposition.

[3] **Mohs hardness** is measured on a scale from 1 to 10. The scale was made about 200 years ago by Friedrich Mohs. Softer minerals have low numbers and harder minerals have high numbers. (http://www.windows.ucar.edu/tour/link=/earth/geology/mohs.html)

First the sputtering current was changed. The experiment results showed that when the sputtering current decreases from 250 *mA* to 80 *mA*, the sputtering rate decreases linearly from 3.1 Å/s to 1.1 Å/s.

Next the gas flow rate was changed. The experiment results showed that when the gas flow rate was increased from 7.5 *CCM* to 30 *CCM*, the sputtering rate decreased from 5.7 Å/s to 2.7 Å/s. Increasing the gas flow rate also increases the chamber pressure. As expected, an increase in the chamber pressure (with the other conditions maintained) results in a decrease in the deposition rate. As the gas flow rate increases, there are more particles inside the chamber, which causes the reduction of the mean free path λ. The mean free path is related to the gas temperature, T, and the chamber pressure, P, as [24]:

$$\lambda = \frac{0.01A(1.5kE)^{\frac{1}{4}}}{6}\frac{T^{\frac{5}{4}}}{P}$$

$$A = \frac{0.012}{\sqrt{M_g}}\left(1+\frac{1}{\mu}\right)^{\frac{1}{2}}\left(1+\mu^{\frac{2}{3}}\right)^{\frac{3}{4}}$$

where M_g is the Molar mass[4] of the gas, μ is the ratio of the mass of the gas to that of the sputtered material, and k is the Boltzmann constant (=8.617 x 10^{-5} *eV/K*).

The total energy depends on the average kinetic energy, E, of the ejected atoms from the target, the sputtering yield, Y, and the sputtering current, I. After each collision, energy is transferred to the gas. High pressure means a small mean free path, which

[4] **Molar mass**: the number of grams in one mole of a substance.

results in a large energy loss and a lower sputtering rate. A low sputtering rate is expected in this experiment, especially for *Al* sputtering. Researches showed that a high flow rate may result in a large grain size of the sputtered film. The large grain size film may cause pinholes, which are not desirable in this research. To reduce the pinhole effect, the gas flow rate must be kept as low as possible. However, lower gas flow rate causes a problem; the increase of the mean free path results in a lower probability of the electrons-gas atoms to generate ions, which the plasma may not be sustained. There is a threshold gas flow rate for the different materials, which is the lowest gas flow rate to sustain the plasma. For soft material, the electrons are easy to be stroked out by the argon ions; these electrons will hit the argon atoms to generate the more argon ions to sustain the plasma. For the hard material, the situation is opposite, so the threshold gas flow rate is higher. After several experiments, we optimized gas flow rate for the *Al* sputtering in this system as $10CCM$.

Changing the negative sputtering voltage is another method to change the sputtering rate. High voltage means a high energy which leads to a high sputtering rate. When the sputtering voltage rises from 500 V to 1 kV (in absolute value), the sputtering rate rises from 5.1 Å/s to 5.8 Å/s. This does not represent a large difference in the sputtering rates corresponding to the two voltages. Once the applied voltage decrease, the sputtering current must increase to maintain certain energy and the gas flow rate must increase to sustain the plasma. Therefore changing the sputtering voltage will affect all the system settings. To avoid this, the sputtering voltage was fixed at -1 kV in this work.

Finally, another parameter that can be manipulated is the sample-target distance. Decreasing this distance increases the sputtering rate linearly. Typically, the sputtering rate can be scaled with the pressure-distance product, *Pd*, in static state [24]. The scaling of the deposition rate with *Pd* is complicated, which related to the resulting gas heating and the pattern at the target. We will not discuss it in this work. To simplify the experiment setting, the distance is kept in maximum for *Al* sputtering (to have a small sputtering rate) and in minimum for $Co_{70}Fe_{30}$ and $Ni_{80}Fe_{20}$ sputtering (to have a large sputtering rate).

4.3 Sputtering Ferromagnetic Materials

4.3.1 Magnetron sputtering

Magnetron sputtering is the most widely used method for vacuum thin film deposition. In DC sputtering, not all of the electrons escaping from the target contribute to the ionized plasma glow area. The wasted electrons move around the chamber causing radiation, heating and other phenomena. A magnetron sputtering system (Figure 4.4) deals with the problem by placing magnetic field behind the target. This magnetic field captures the escaping electrons and confines them to the immediate vicinity of the target. The electrons fly to the substrate will experience the Lorentz Force [$\vec{F} = q(\vec{E} + \vec{v} \times \vec{B})$] (Figure 4.5), which makes them fly in a spiral shape and increases the probability of ionization of the argon atoms. The ion current (density of ionized argon atoms hitting the target) is increased by an order of magnitude over a

conventional sputtering system, resulting in faster deposition rates at lower pressure. The lower pressure in the chamber helps create a cleaner film. Target temperature is lower with magnetron sputtering, enhancing the deposition of high quality films.

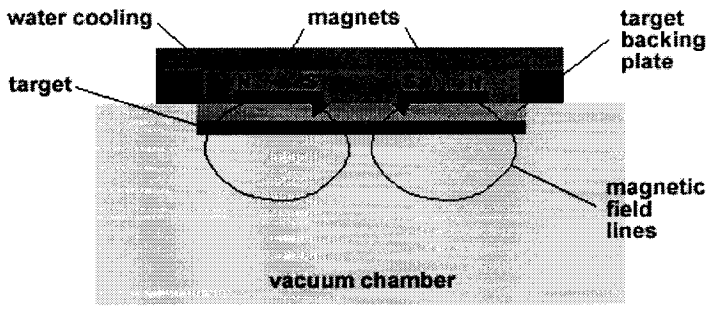

Figure 4.4 Schematic of a magnetron [25]

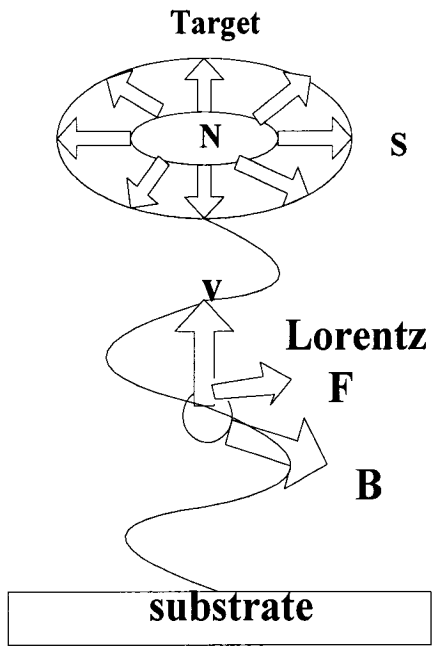

Figure 4.5 Scheme of a particle experiences Lorentz force

4.3.2 Ferromagnetic materials sputtering

Ferromagnetic is a material, in which the magnetic moments are all point in one direction at the present of an external magnetic field. It has a net magnetic moment and behaves like a bar magnet producing a magnetic field outside of it. *CoFe* (hard magnetic material: also referred to as permanent magnets) are magnetic materials that retain their magnetism even after the external magnetic field removed [26]. *NiFe* (soft magnetic material) are materials that are easily magnetised and demagnetised [26]. Both of these materials were used in this work.

Sputtering of ferromagnetic materials, such as *Co*, *Fe*, and *Ni*, can pose a special challenge, because these metals invariably absorb a portion of the magnetic field which controls the process and that inhibits maximum performance.

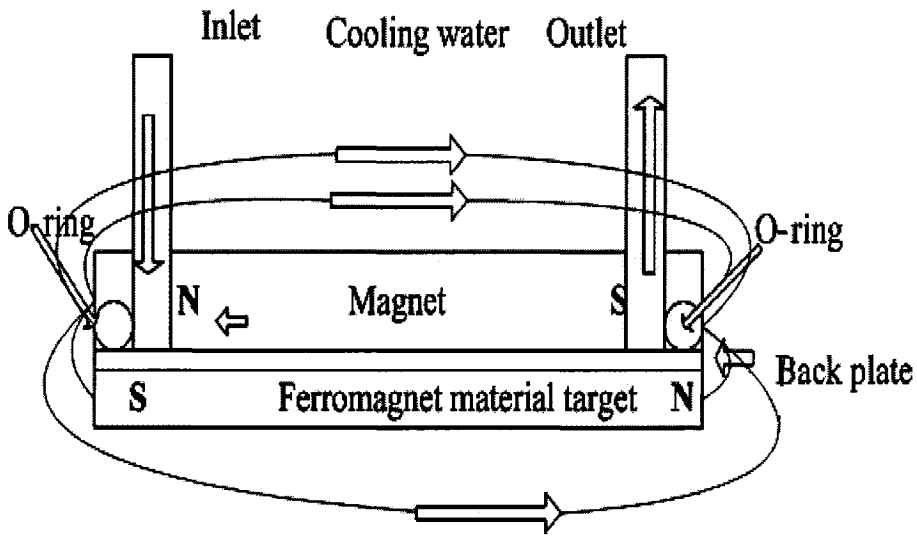

Figure 4.6 Scheme of a magnetic field reducing

When an external magnetic field applied on $Co_{70}Fe_{30}$ or $Ni_{80}Fe_{20}$, it produces a magnetic field outside of them. The magnetic field created to confine the electrons in the magnetron plasma is absorbed by the target materials themselves. Figure 4.6 shows the cancellation of a magnetic field. The ferromagnetic material is magnetised by the magnetron field placed behind the back plate, these two fields have opposite directions so they cancelled each other and result reduction of the total field strength on the target side. Depending upon the properties of the material this can cause problems. One problem is the limitation of the thickness of the target. Depending upon the magnetic saturation of the material, the thickness of the target need to be limited to a certain level that still enables a sufficient magnetic field (200-250 Gauss) to be penetrated through the target surface to maintain efficient sputtering plasma [27].

The second problem with conventional approaches to sputter ferromagnetic target is that the target utilisation is low compared to non-magnetic targets. The reason is the effect of the shape of the target erosion (Figure 4.7) on the magnetic field profile over the target surface. As the target erodes more in the centre of the target, there is less ferromagnetic material to absorb the magnetic field, and magnetic field is stronger there. This is a self propagating problem since the more material is sputtered, stronger the field there will be more erosion enhanced [27]. Due to the thin sputtered film layers (15 nm to 20 nm) the target erosion was neglected in this work.

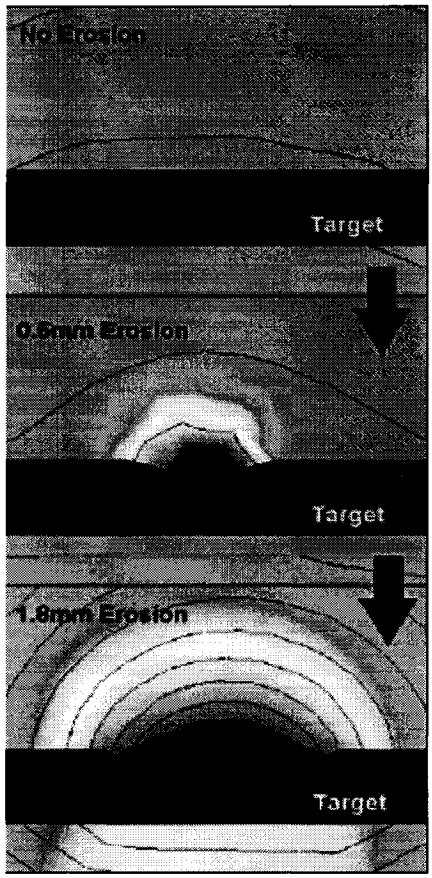

Figure 4.7 Ferromagnetic material target erosion [27]

From the experiments we know that the sputtering rate for $Co_{70}Fe_{30}$ is 0.04 Å/s and for $Ni_{80}Fe_{20}$ is 0.2 Å/s. To achieve 15 nm $Co_{70}Fe_{30}$ layer, almost sixty minutes sputtering time is needed, which is impossible for the system. A long time sputtering leads to high temperature on the target and the samples. The lower sputtering rate is caused by the extra field that reduces the effect of the magnetron field and the hardness of the material.

This problem is solved by reducing the targets thickness (the thicknesses of the $Co_{70}Fe_{30}$ and $Ni_{80}Fe_{20}$ targets are less than 1 mm) and reducing the target-substrate distance. Reducing the targets thickness will reduce the magnetic field produced by the

targets and hence increase the effect of the magnetron field. Reducing the target-substrate distance will increase the sputtering rate linearly (as mention before). In our experiments, the distance between target and substrate can not be measured very precisely. So the thicknesses of $Co_{70}Fe_{30}$ and $Ni_{80}Fe_{20}$ layers were evaluated by estimation. The actual target-substrate distance is reduced about two times of the original distance. Reducing the distance two times also reduces the sputtering time by four times, which means the sputtering time is reduced to 15 minutes.

The high temperature of the target is also harmful for the system. Because the target is very thin, the high temperature may deform the target and make the sputtered film non uniform. Also the high temperature may destroy the o-ring inside the cooling system, due to the large temperature difference between the cooling water and target-back plate assembly. To protect the target and the system, the sputtering system runs in one minute and cools in three minutes for sixty minutes. The total running time is still fifteen minutes for both $Co_{70}Fe_{30}$ and $Ni_{80}Fe_{20}$. The top electrode ($Ni_{80}Fe_{20}$) had a thicker layer compared to the bottom electrode ($Co_{70}Fe_{30}$), because of its higher sputtering rate.

CHAPTER 5

MEASUREMENTS AND RESULTS DISCUSSION

5.1 Oxidation and Nitridation of the Samples

The oxidation and nitridation of the *Al* layers were performed as follow: for the thermal oxidation, *Al* layers were oxidized by exposing the layers to a pure oxygen environment; the oxidation happens due to the bonding of aluminium and oxygen atoms. The alternative ways are, either to oxidize the surface of the layers in air, or to reactive sputter the surface with a mixture of argon and oxygen gases.

For the nitridation of the *Al* layers, the *Al* layer was exposed to a pure nitrogen environment (thermal nitridation), or it was reactive sputtered by a mixture of argon and nitrogen gases.

Figure 5.1 and 5.2 show the pictures of an oxidized sample (Al_2O_3) and a nitridized sample (*AlN*) respectively. On the left side, the image shows the pictures of the samples, and on the right side shows their surface, as measured by the optical profilemeter and the Scanning Electron Microscope (SEM). The samples were fabricated on *N*-type *Si* wafers. The light colors show the bottom electrodes while the dark colors show the top electrodes. *MTJ*s are located in between the bottom and the top electrodes. The light areas were made of layers of *Ti* and *Cu*, and the dark areas were made of layers of $Co_{70}Fe_{30}$, *Al* insulating and $Ni_{80}Fe_{20}$. The scratches, seen on the surface of the samples, are due to the movement of the probes during the measurements.

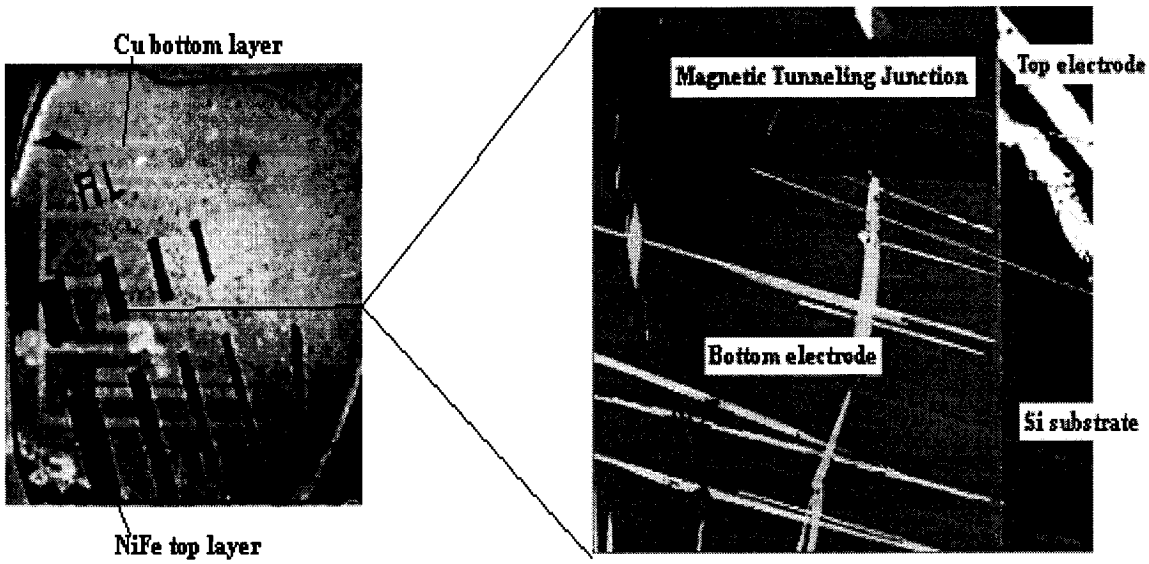

Figure 5.1 Oxidized Sample 1 [*Si/Ti/Cu/$Co_{70}Fe_{30}$/Al_2O_3 (2.4 nm)/$Ni_{80}Fe_{20}$*] with *Al* layer exposed to a pure oxygen environment for 10 minutes

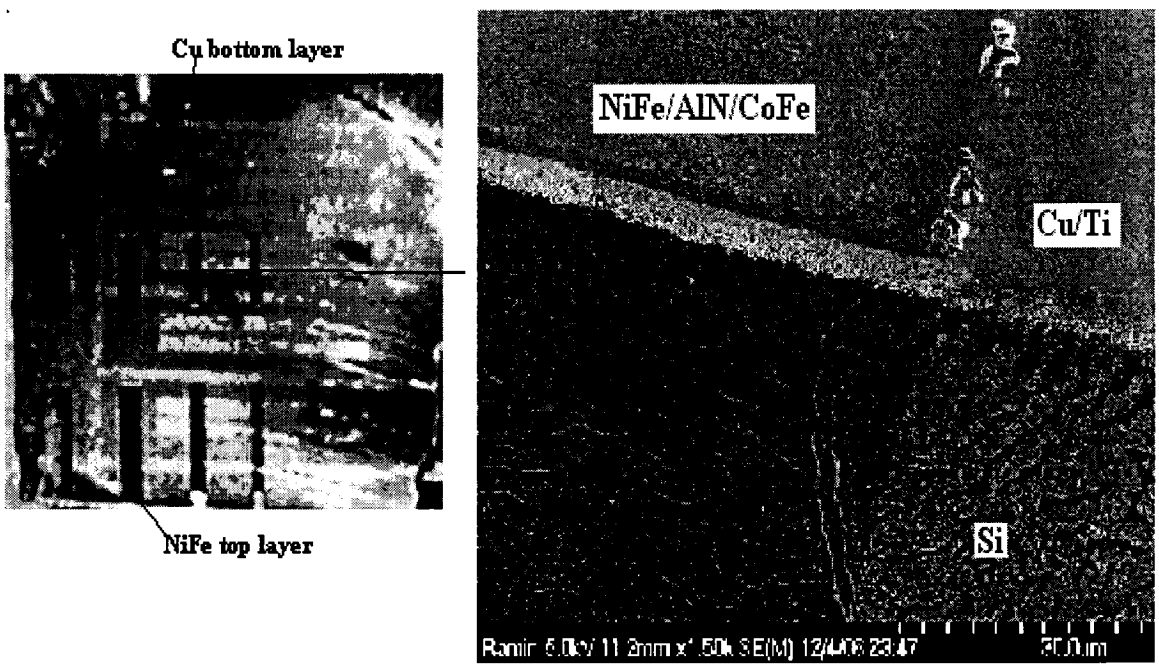

Figure 5.2 Nitridized Sample 3 [*Si/Ti/Cu/$Co_{70}Fe_{30}$/AlN (2.4 nm)/$Ni_{80}Fe_{20}$*] with *Al* layer exposed to a pure nitrogen environment for 30 minutes. Scan Electron Microscope picture shows the composite of the tunneling junction layers.

Figure 5.3 shows a picture taken from the optical profilmeter. The picture shows that the bottom electrode surface and the top electrode surface are flat, which demonstrates that the surface roughness of the device is very good and the grain size is small. The optical profilmeter can measure a step of different layers down to one micrometer, but our devices are in the nano size range. The optical profilmeter is not able to measure the size very accurately, so SEM was used to measure the junction thickness.

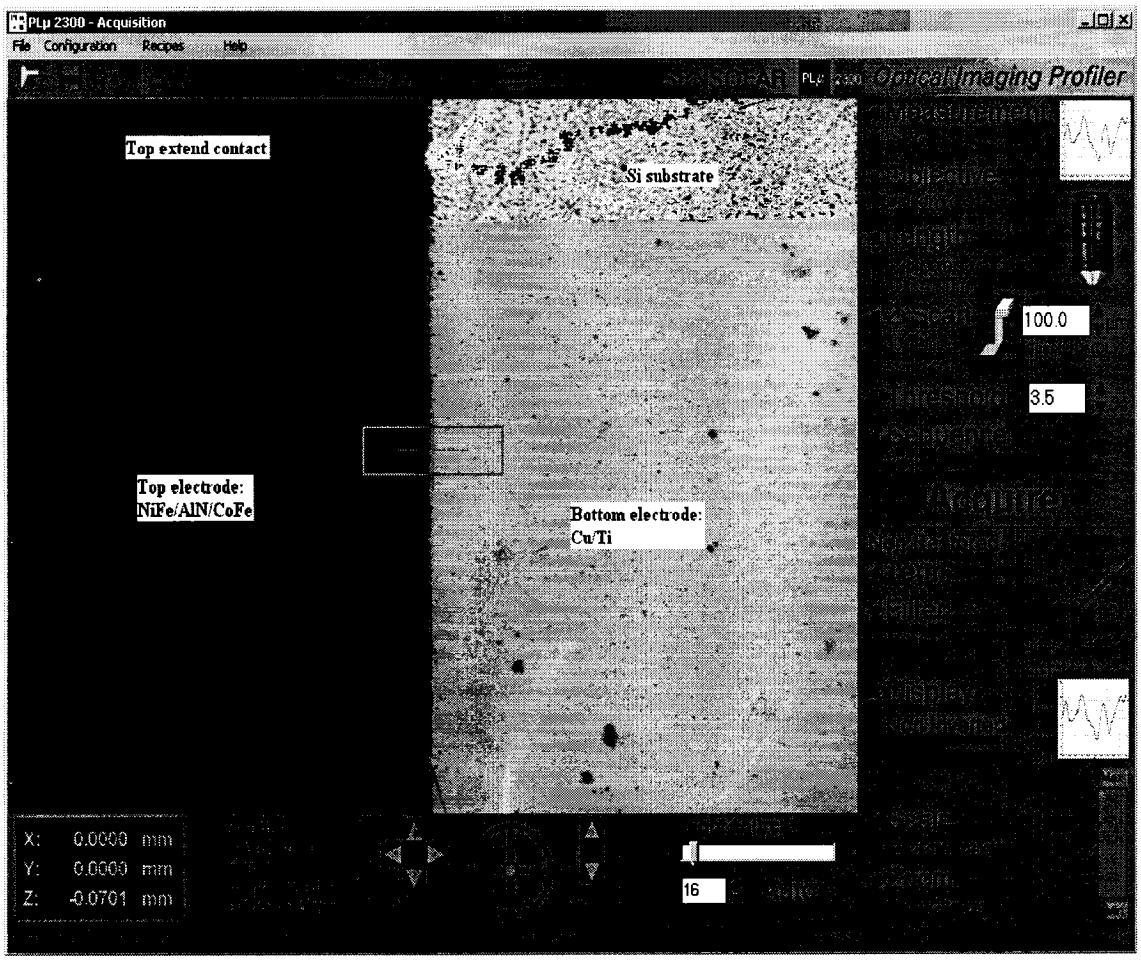

Figure 5.3 Optical profilemeter image picture

Figure 5.4 shows the SEM picture of a tunneling junction, which was taken from the same area as the optical profilmeter did. The dark area is a tunneling junction composed by $Co_{70}Fe_{30}$, *AlN* and $Ni_{80}Fe_{20}$ layers. The thickness of these layers is around 200 nm. From the sputtering thickness monitor, the thickness of *AlN* layer is 2.4 nm, so the thickness of *NiFe* and *CoFe* sputtered layers is around 200 nm, which is much higher than we were expecting. Increasing the thickness of ferromagnetic material layers will not affect the tunneling probability as shown in equation (4.1), but the magnitude of the external magnetic field will be affected. For a thick ferromagnetic material layer, a strong external magnetic field is needed to switch the internal magnetic field orientation.

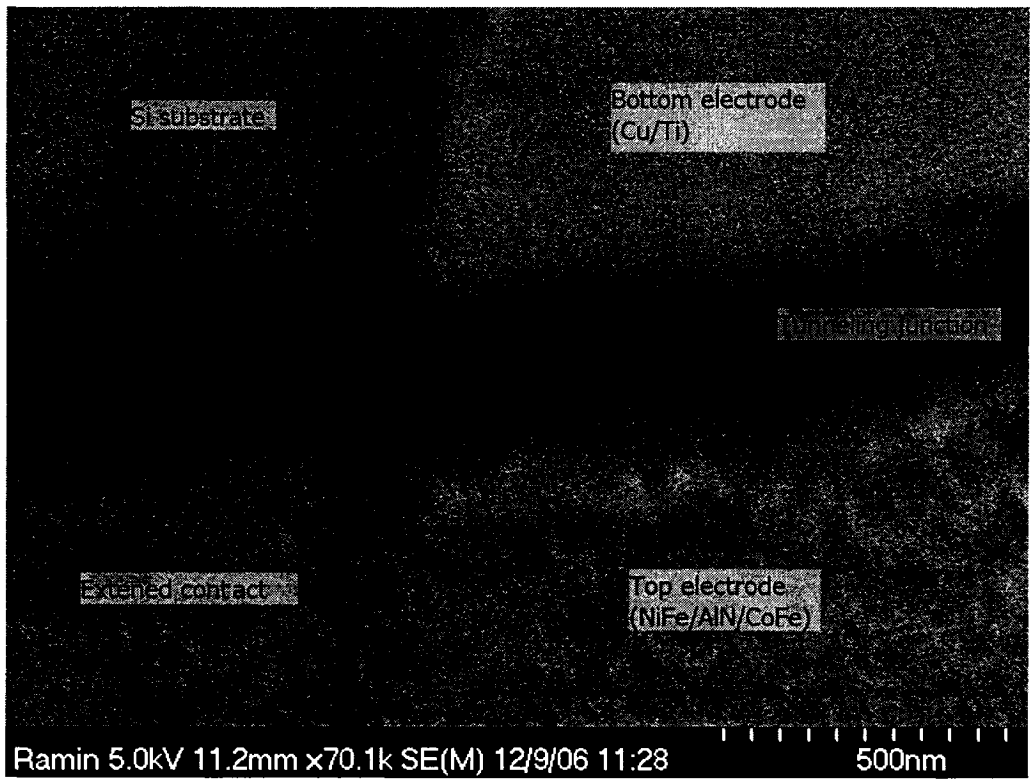

Figure 5.4 SEM picture shows the thickness of the tunneling junction between the top and the bottom electrodes. The thickness of *NiFe/AlN/CoFe* layers is 200 nm.

Table 4 shows list of the samples fabricated in this work. The table shows the thickness of the *Al* layers as well as the insulating layers process description during oxidation and nitridation.

Table 4 List of samples and processes description

Sample Number (thickness of aluminium layer)	Processes Description (insulating layer)
Sample 1 (2.4 nm)	Exposed to pure oxygen for 10 minutes
Sample 2 (2.4 nm)	Exposed to air for 10 minutes
Sample 3 (2.4 ~ 2.5 nm)	Exposed to pure nitrogen for 30 minutes
Sample 4 (2.5 nm)	Exposed to pure nitrogen for 15 minutes
Sample 5 (2.4 nm)	Exposed to pure nitrogen for 5 minutes
Sample 6 (2 nm)	12 % oxygen reactive sputtering
Sample 7 (2 nm)	12 % oxygen reactive sputtering
Sample 8 (2 nm)	12 % nitrogen reactive sputtering

The reactive sputtering is done by using Trace Gas Mixer to mix the gases. The mixer delivers precisely regulated gas mixtures into the sputtering chamber. There are two gas inlets for inputs, and one gas outlet for output. There are two regulators and two gas pressure meters to adjust and monitor the input gases on the mixer in order to control both the gas flow and the line pressure. For a precise gas mixture, it is important that both regulators are set identically to eliminate backpressure differencies that can severely compromise the accuracy of a gas mixture. In this work, the pressures of the two mixed gases were set to 15 psi. Two mass flow meters are used to control the ratio of mixed gases. The lowest scale of these mass flow meters is 3 Cubic Feet per Hour

(*CFH*) and the highest mass flow rate of the argon gas is 22 *CFH*. The lowest gas mixture ratio can be calculated as:

$$\text{The lowest gas mixture ratio} = \frac{O_2 or N_2}{Argon + O_2 or N_2} = \frac{3}{22+3} \times 100\% = 12\%$$

This lowest gas mixture ratio is used in this research. The mixed gas was fed to the sputtering system gas inlet. The sputtering system is able to control the gas flow rate by a mass flowmeter at the maximum of 50 *CCM*.

5.2 Annealing of the Samples

The annealing process is a heat treatment that affects the physical properties such as strength, hardness and removes the coarseness of grains in micro/nano-structures. The annealing process can greatly increase the *TMR* ratio as reported in the literatures [6] [16] [28].

In this research, all samples were annealed once they were characterized initially.

The annealing process was done in the Micro Devices & Microfabrication Lab. The annealing temperature was set at 200°C as discussed in section 4.1.2 to make sure that the bottom electrode has the minimum contact resistance. Prior to the loading of the samples, the furnace was warm up to 200°C. At this temperature, the furnace was flushed with the nitrogen gas for 15 minutes to remove the oxygen or any other residuals inside the furnace. Then the samples were loaded and kept in nitrogen

environment for 30 minutes. After 30 minutes, the furnace power was turned off and the samples were cooled down inside the furnace under nitrogen, to avoid oxidation of the samples. The samples were unloaded when the furnace temperature reached the room temperature.

Once the samples were annealed successfully, they were characterized again to compare the effect of annealing on the measured parameters.

5.3 Tunneling Junction Resistances vs. Applied Magnetic Field

5.3.1 Experimental setup

The arrangement for the tunneling junction resistances vs. the external magnetic field measurements is shown schematically in Figure 5.5. Two extended contacts were made for connecting the electrodes to *Cu* and $Ni_{80}Fe_{20}$ layers. Two micro-needle probes touched these two contacts. A FLUKE 8050A Digital Multimeter was used to measure the variation of the tunneling junction resistances vs. the external magnetic field. A permanent magnet bar was used to generate the external magnetic field. The magnet bar could move on the top of the junction without touching the surface. The external magnet induced a field varying from -200 Gauss to +200 Gauss. The magnetic field was measured using Hall Effect SYPRIS 5080 Gauss/Tesla Meter.

The magnet probe was placed as close to the tunneling junction as possible to reduce the magnetic field differences between the probe and the tunneling junction. All the measurements were done at room temperature. The measured data are presented in Appendix A.

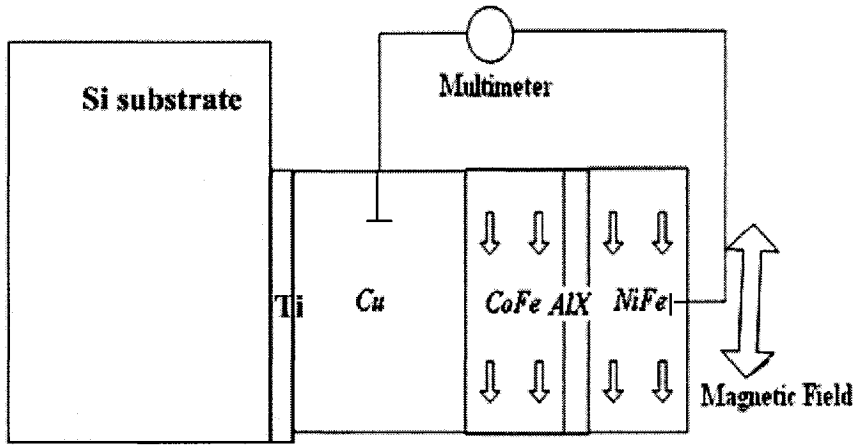

Figure 5.5 Experimental setup to measure the tunneling junction resistances vs. magnetic field (*Cu* layer is used as a bottom electrode and $Ni_{80}Fe_{20}$ layer is used as a top electrode. *AlX* is an insulating layer. An external magnetic field is applied and the magnetic states inside $Co_{70}Fe_{30}$ and $Ni_{80}Fe_{20}$ layers aligned with this field. A multimeter is used to measure the tunneling junction resistances vs. magnetic field)

5.3.2 Results and discussion

Sample 1: (2.4 nm *Al* layer exposed to pure oxygen for 10 minutes)

The tunneling junction resistances vs. magnetic field of Sample 1, before and after annealing are shown in Figure 5.6.

The horizontal axis shows the change of external magnetic field from -200 Gauss to +200 Gauss. The vertical axis shows the change of the tunneling junction resistances in kilo-ohms (kΩ).

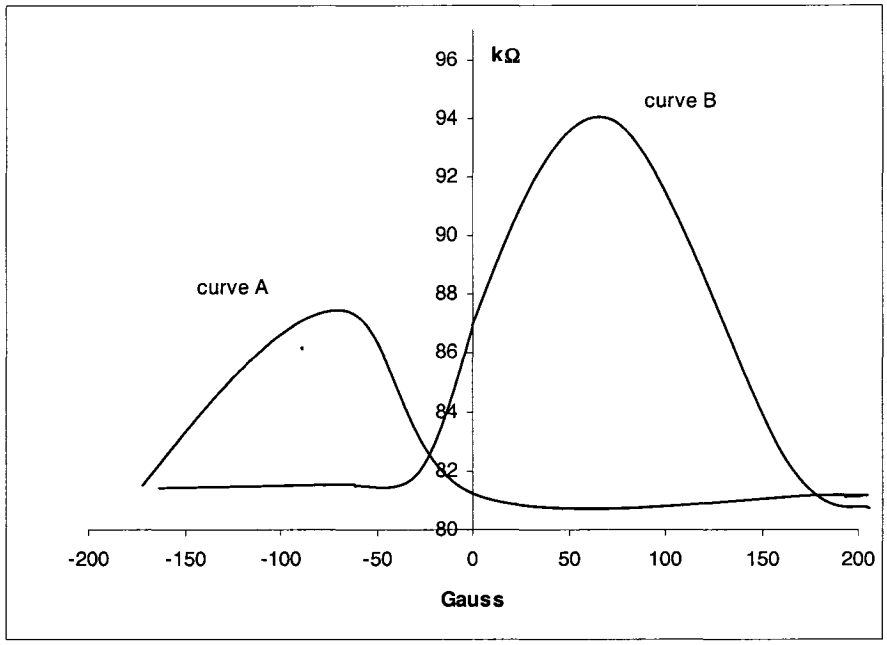

(a) Before annealing

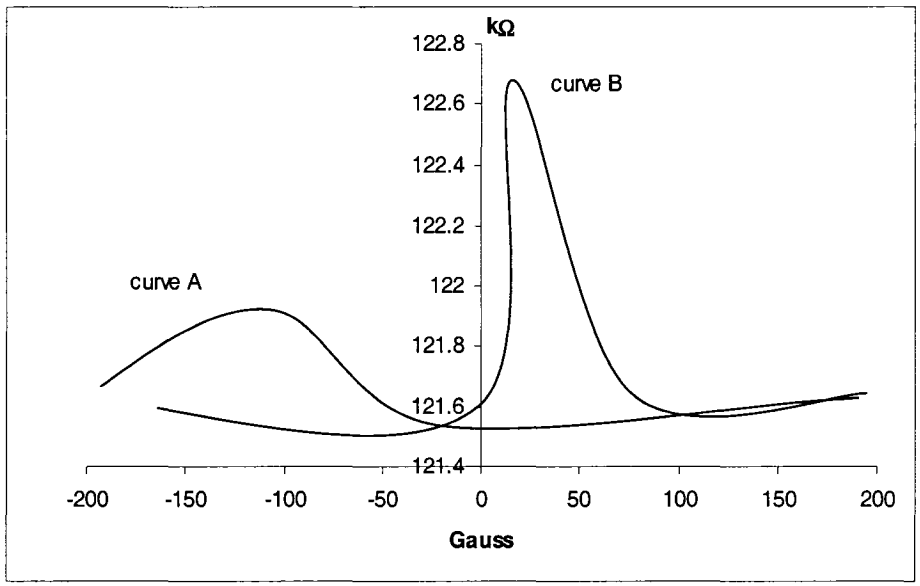

(b) After annealing

Figure 5.6 Tunneling junction resistances vs. magnetic field curves of Sample 1. Curve A represent the variation of the junction resistance vs. magnetic field when the external magnetic field is changed from +200 to -200 Gauss and curve B represent the variation of the junction resistance vs. magnetic field when the external magnetic field is changed from -200 to +200 Gauss.

The magnetic field direction is defined as positive when the magnetic fluxes go from the top electrode via insulating layer to the bottom electrode, and negative when the magnetic fluxes go from the bottom electrode to the top electrode.

Based on the discussion in section 2.2 and Figure 2.3 (b), the majority/minority band electrons are forced to tunnel into the minority/majority band of the opposing electrode in anti-parallel condition. The reduced number of states available for tunneling between the ferromagnetic layers when the layers are anti-parallel results in an increased tunneling resistance compared to parallel. The junction resistance is the highest when the magnetic states of the two layers, $Co_{70}Fe_{30}$ and $Ni_{80}Fe_{20}$, are in anti-parallel condition. The top layer, $Ni_{80}Fe_{20}$, is a soft ferromagnetic material; its magnetic state direction is easy to alert by the external magnetic field compared to layer of $Co_{70}Fe_{30}$, which is a hard ferromagnetic material.

In Figure 5.6, at +200 Gauss external magnetic field, the magnetic states of the two layers are aligned with the external magnetic field. Therefore the two magnetic states are parallel and the minimum tunneling junction resistance will be observed. The resistance remains the same until the external magnetic field becomes zero. At this stage, the magnetic state of $Ni_{80}Fe_{20}$ (soft ferromagnetic material) starts to switch in the direction opposite to the magnetic state of $Co_{70}Fe_{30}$ (hard ferromagnetic material). As a result, the tunneling junction resistance increases to its maximum as the external magnetic field increases toward negative direction. As the external magnetic field negatively increases, the junction resistance falls down slowly (because the variation of the magnetic states of the hard ferromagnet is very slow) to minimum again, as the magnetic states of the two layers becomes aligned again.

Figure 5.6 shows that on both graphs there are two peaks. The peaks on the right side of the vertical axis are caused by increasing of the magnetic field in positive direction. The peaks on the left side of the vertical axis are caused by increasing of the magnetic field in negative direction. The two peaks do not have the same height, and the positions are not symmetrical with respect to the vertical axis. That is due to the magnetic Hysteresis loop in the system which is not symmetrical.

"Hysteresis is well known in ferromagnetic materials. When an external magnetic field is applied to a ferromagnet, the ferromagnet absorbs some of the external field. Even when the external field is removed, the magnet will retain some field: it has become *magnetized.* The relationship between magnetic field strength (H) and magnetic flux density (B) is not linear in such material" [29].

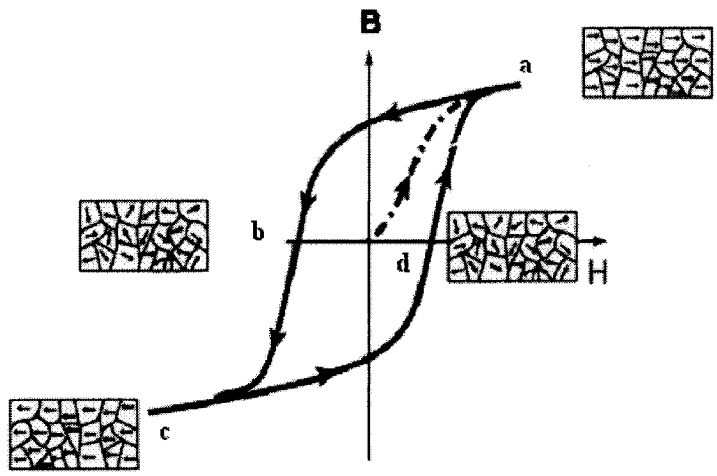

Figure 5.7 Hysteresis loop

In Figure 5.7, when the magnetic field strength (H) starts to decrease from a positive value to zero, and then decreases to a negative value, the induced magnetic flux

densities (B) on top and bottom electrodes will change along the "*abc*" curve. When the external magnetic field strength changes from a negative magnetic field to zero, and then to a positive magnetic field strength, the magnetic flux densities on the top and the bottom layers will not follow the same curve; an extra magnetic force is needed to overcome the remaining field, so the magnetic flux densities changes along the "*cda*" curve.

Each ferromagnetic material has its own Hysteresis loop. When they form a multilayer system, the final Hysteresis loop may display an asymmetrical shape, especially in *Co*-based ferromagnetic alloys. "The shape of Hysteresis loop depends on the time, the temperature, the applied field and the atmosphere during annealing, as well as on the composition and preparation of the starting material [30]". Hysteresis loop may shift up or down, and shift right or left by the different processing conditions. In our experiment, each sample has its unique Hysteresis loop, because each sample has a different processing condition. The asymmetrical shape of Hysteresis loop lead to different height of peaks as shown in Figure 5.6.

A theoretical tunneling junction resistance vs. magnetic field measurement curve is shown in Figure 5.8. The two curves show two equal peaks symmetrical around the zero magnetic field strength. In this case the Hysteresis loop of the system is assumed to be symmetrical. Figure 5.8 is compatible to Figure 5.6 in some points; both of them have a slow decrease in resistances and two peaks of resistances as the external magnetic field changes. Because of the limitation of the external magnetic field, the small resistance at higher magnetic field can not be observed in Figure 5.6. If we increase the magnetic field more, we can see small resistance (long tail) at a higher magnetic field.

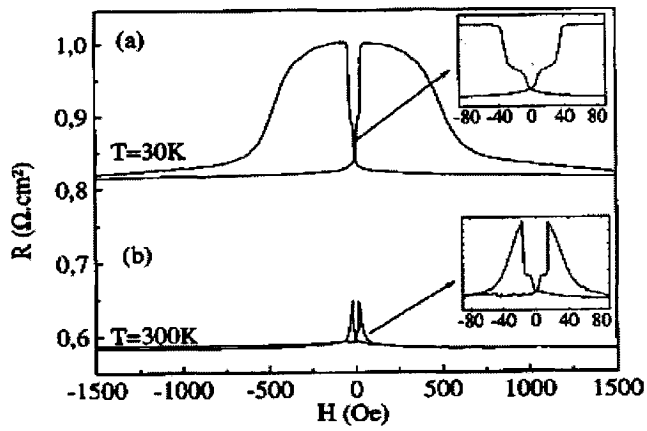

Figure 5.8 Theoretical tunneling resistances vs. magnetic field curve in *MTJ* [31]

Before annealing, the maximum tunneling resistance is 94.5 kΩ and the *TMR* ratio is 17.24%. After annealing, the maximum tunneling resistance is 127 kΩ and the *TMR* ratio is 4.77%. The increasing of the tunneling resistance and the decreasing of the *TMR* ratio after the annealing process is caused by the over-oxidation of the electrodes. The sample was oxidized in a higher oxygen concentration environment for 10 minutes after the *Al* layer was sputtered; the thin *Al* layer due to the high oxygen diffusion coefficient is well oxidized. There is a possibility that some oxygen atoms were trapped inside this layer. During the annealing process, these atoms may oxidize the top and the bottom electrodes, reduce the conductivity of the electrodes and cause an increase in the junction resistance. As show in Figure 5.9 (a), before annealing, the resistances of the two electrodes are negligible; the total resistance is caused by the magnetic tunneling resistance. After annealing, the top and the bottom electrodes are oxidized and the resistances of the two electrodes can not be neglected. The total resistance between the two electrodes is due by the magnetic tunneling resistance and resistances caused by the oxidation of the two electrodes (Figure 5.9 (b)).

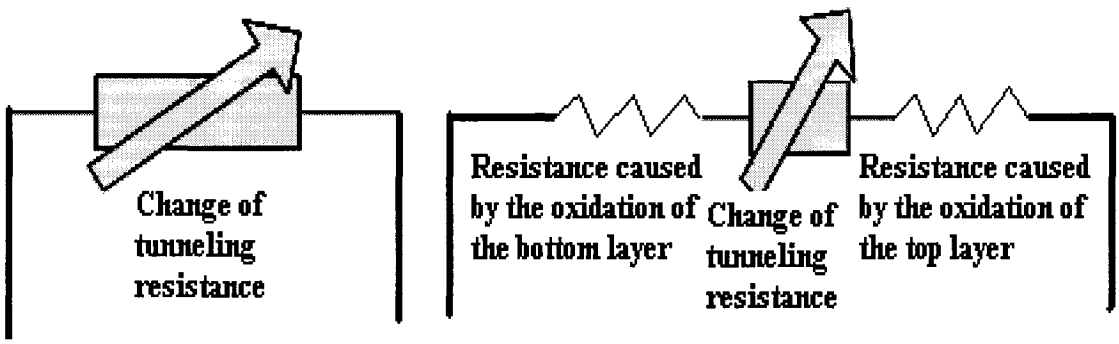

(a) (b)

Figure 5.9 Schematic show of the resistance change affected by annealing in over-oxidized condition (a) Before annealing; (b) After annealing

Sample 2: (2.4 nm *Al* layer exposed to air for 10 minutes)

The tunneling junction resistances vs. magnetic field for Sample 2, before and after annealing are shown in Figure 5.10.

Two symmetrical peaks are shown clearly and in the junction resistance before annealing curve. After annealing, the two peaks have different heights and are asymmetrical. Obviously, the shape of Hysteresis loop of the system was affected by the annealing process. The tunneling resistance increases after annealing as explained for Sample 1. Sample 2 was oxidized in air, so there are less oxygen atoms inside the *Al* layer, so the effect of oxidation of the top and the bottom electrodes is not very strong. The *TMR* ratio has increased from 1.71% to 12.96% (7.6 times), which demonstrate the effect of the annealing process.

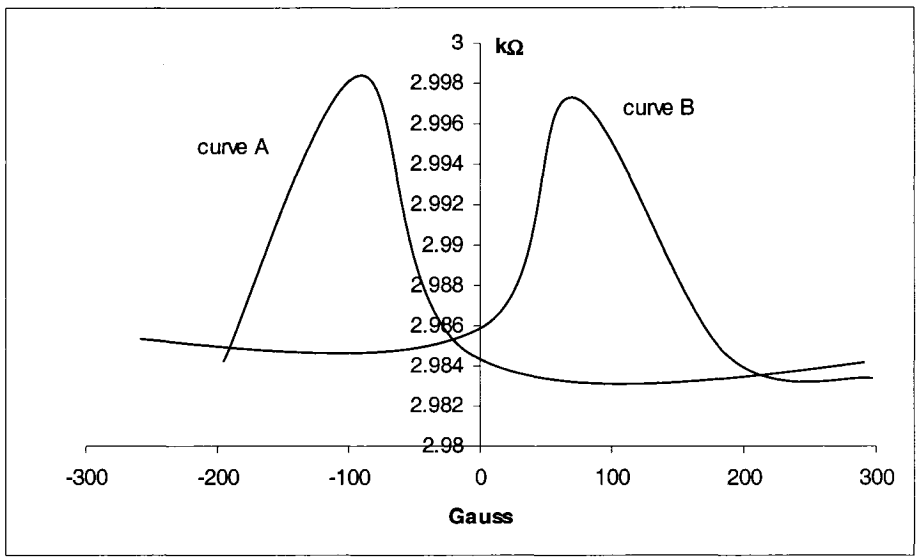

(a) Before annealing

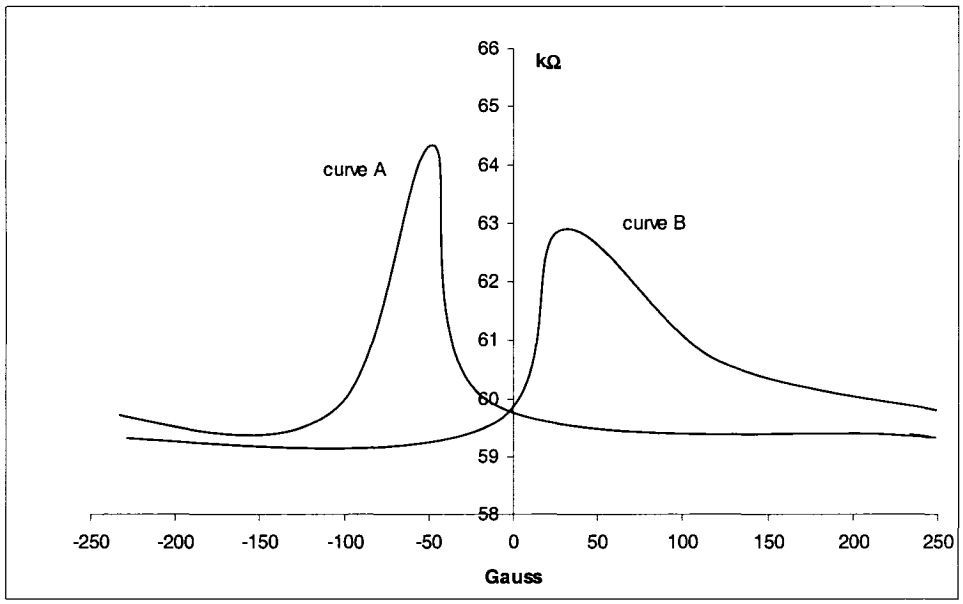

(b) After annealing

Figure 5.10 Tunneling junction resistances vs. magnetic field curves of Sample 2。 Curve A represent the variation of the junction resistance vs. magnetic field when the external magnetic field is changed from +200 to -200 Gauss and curve B represent the variation of the junction resistance vs. magnetic field when the external magnetic field is changed from -200 to +200 Gauss.

Sample 3: (2.4 ~ 2.5 nm *Al* layer exposed to pure nitrogen for 30 minutes)

The tunneling junction resistances vs. magnetic field of Sample 3, before and after annealing are shown in Figure 5.11.

The tunneling resistance is quite high, around 22 ~ 23 MΩ before annealing. After annealing, the tunneling resistance decreases to around 7 MΩ and the *TMR* ratio increases to 27.9%; this is the largest *TMR* ratio achieved in this work.

The two peaks have almost the same value and are symmetrical around the vertical axis before and after annealing.

Sample 4: (2.5 nm *Al* layer exposed to pure nitrogen for 15 minutes)

The tunneling junction resistances vs. magnetic field of Sample 4, before and after annealing are shown in Figure 5.12.

Before annealing, the two peaks have different height (4 kΩ). After annealing, the two peaks have a 0.4 kΩ difference and the tunneling resistance decreases. The *TMR* ratio decreased slightly after annealing, this may be caused by some unknown effect. The tunneling resistances are low before and after annealing, 0.9 MΩ and 113 kΩ. A reduced nitrogen expose time and the annealing process can reduce the tunneling resistance drastically. The shape of Hysteresis loop of the system was less affected by the annealing process just by looking at the symmetrical of the two peaks.

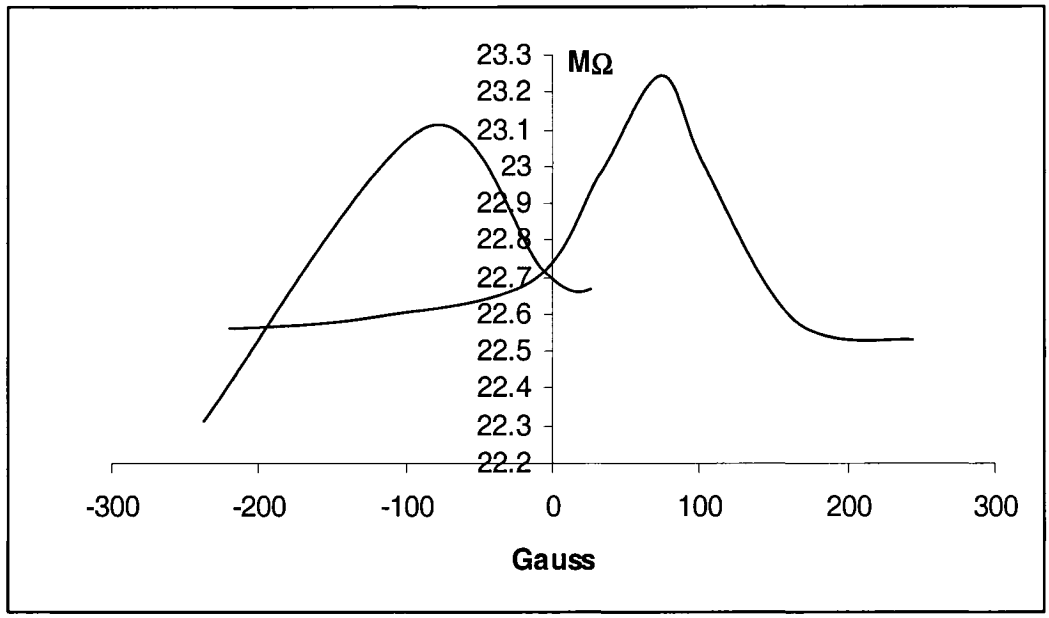

(a) Before annealing

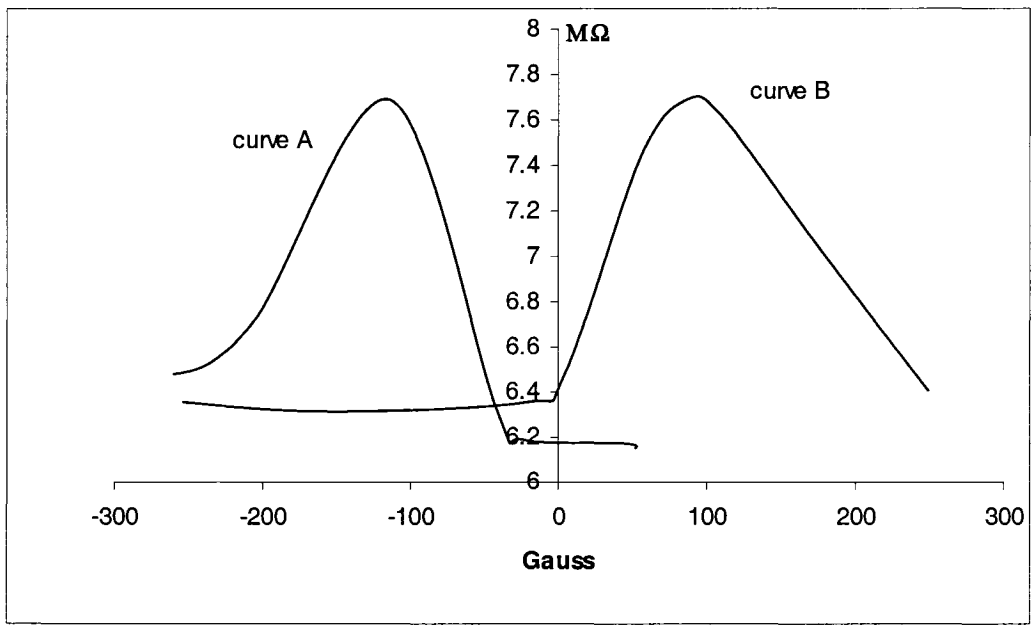

(b) After annealing

Figure 5.11 Tunneling junction resistances vs. magnetic field curves of Sample 3. Curve A represent the variation of the junction resistance vs. magnetic field when the external magnetic field is changed from +200 to -200 Gauss and curve B represent the variation of the junction resistance vs. magnetic field when the external magnetic field is changed from -200 to +200 Gauss.

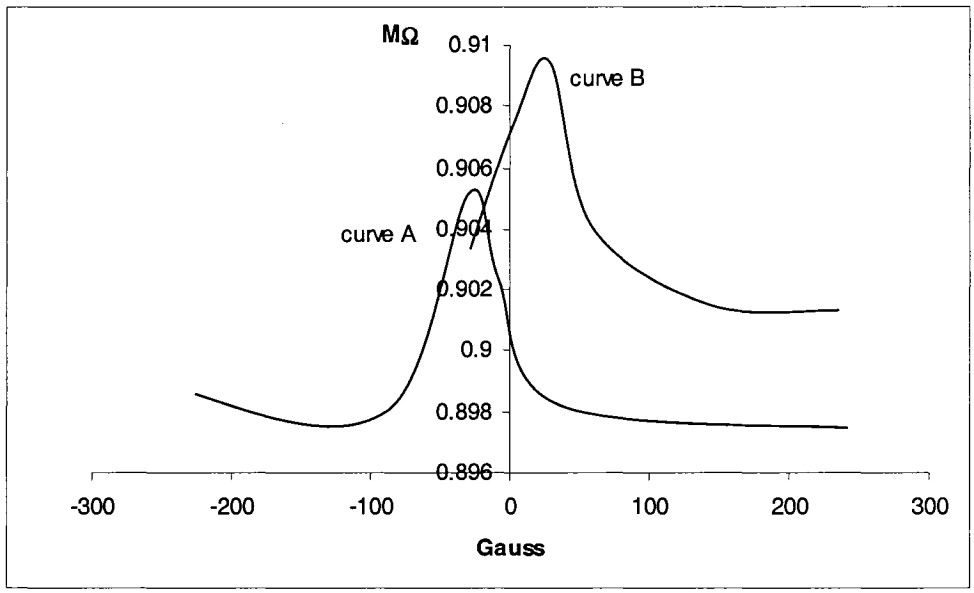

(a) Before annealing

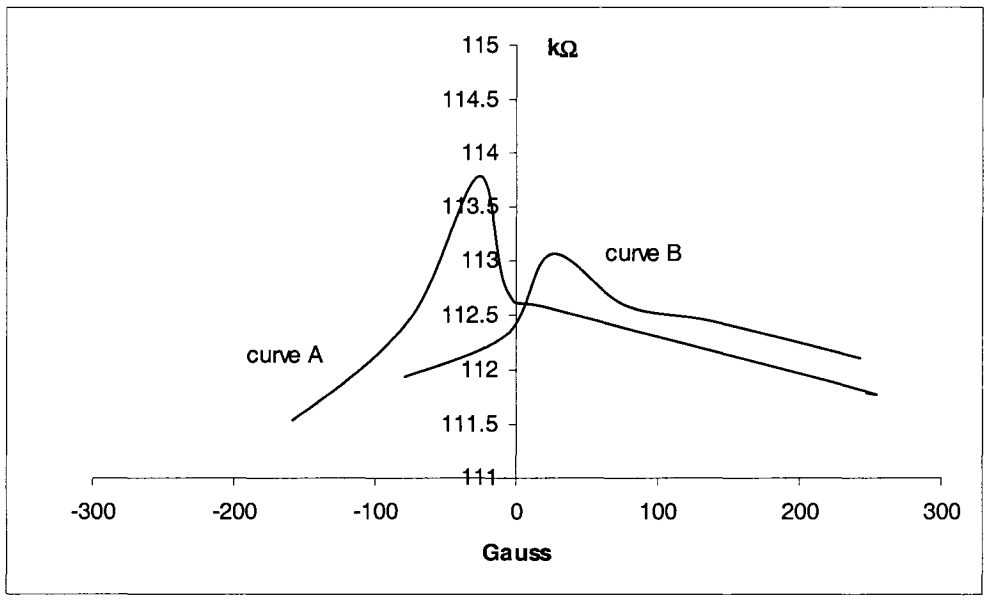

(b) After annealing

Figure 5.12 Tunneling junction resistances vs. magnetic field curves of Sample 4. Curve A represent the variation of the junction resistance vs. magnetic field when the external magnetic field is changed from +200 to -200 Gauss and curve B represent the variation of the junction resistance vs. magnetic field when the external magnetic field is changed from -200 to +200 Gauss.

Sample 5: (2.4 nm *Al* layer exposed to pure nitrogen for 5 minutes)

The tunneling junction resistances vs. magnetic field of Sample 5, before and after annealing are shown in Figure 5.13.

The two peaks of the tunneling resistance are clearly shown in Figure 5.13. The tunneling resistance decreases from 1.3 MΩ to 0.8 MΩ after annealing, but the *TMR* ratio increase from 2.77% to 23.97%, which is a 8.7 times increase. The two peaks have 4 kΩ and 30 kΩ differences before and after annealing. The differences are not very large compared to the absolute value of the resistance (~1 MΩ). The two peaks are still symmetrical around the vertical axis.

Sample 6: (2 nm *Al* layer 12 % oxygen reactive sputtering)

The variation of tunneling junction resistances vs. magnetic field of Sample 6, before annealing is shown in Figure 5.14.

As it is seen in Figure 5.14, no data could be observed for the sample before the annealing and even after the annealing; the results of Sample 6 are not acceptable. After annealing, although we can obtain the resistance data from the change of the magnetic field, they are not adequate. Since we have Sample 7 processed under same reactive sputtering conditions, the plot, after annealing, is not shown here.

The tunneling resistance is around 115 kΩ before annealing and decreases to 50 kΩ after annealing. The *TMR* ratio increases from 6.25% to 13% after annealing, which is expected.

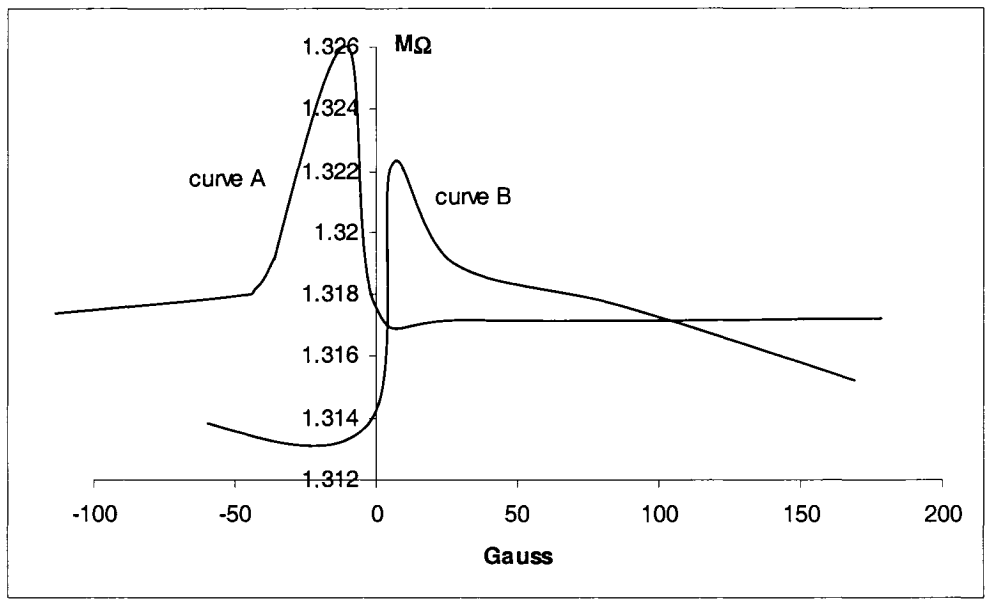

(a) Before annealing

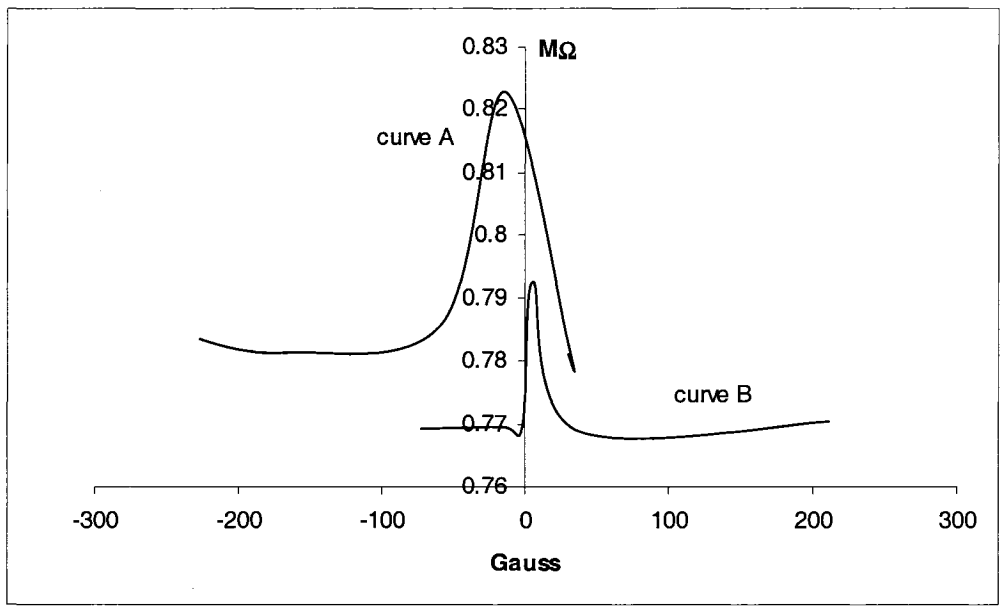

(b) After annealing

Figure 5.13 Tunneling junction resistances vs. magnetic field curves of Sample 5. Curve A represent the variation of the junction resistance vs. magnetic field when the external magnetic field is changed from +200 to -200 Gauss and curve B represent the variation of the junction resistance vs. magnetic field when the external magnetic field is changed from -200 to +200 Gauss.

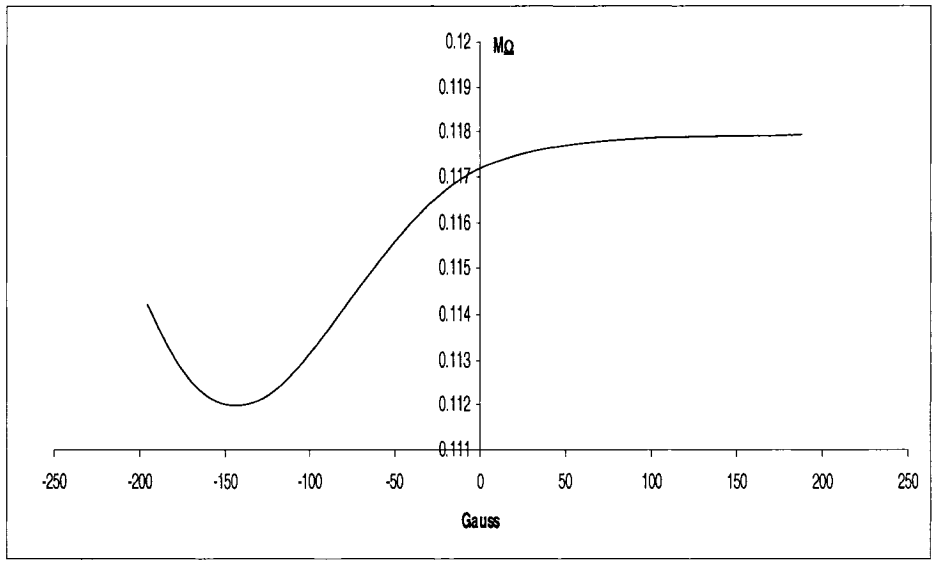

Before annealing

Figure 5.14 Tunneling junction resistances vs. magnetic field curve of Sample 6. The curve represents the variation of the junction resistance vs. magnetic field when the external magnetic field is changed from -200 to +200 Gauss.

Sample 7: (2 nm *Al* layer 12 % oxygen reactive sputtering)

The tunneling junction resistances vs. magnetic field of Sample 7, before and after annealing are shown in Figure 5.15.

Sample 7 is processed by the oxygen reactive sputtering; the resistance is around 60 kΩ after annealing, as for Sample 6 and acceptable. The *TMR* ratio is low (3.17%) even after annealing.

Figure 5.15 shows one peak before and after annealing, the other peak is not clear. There are no enough points to plot the tunneling resistances vs. magnetic field curve.

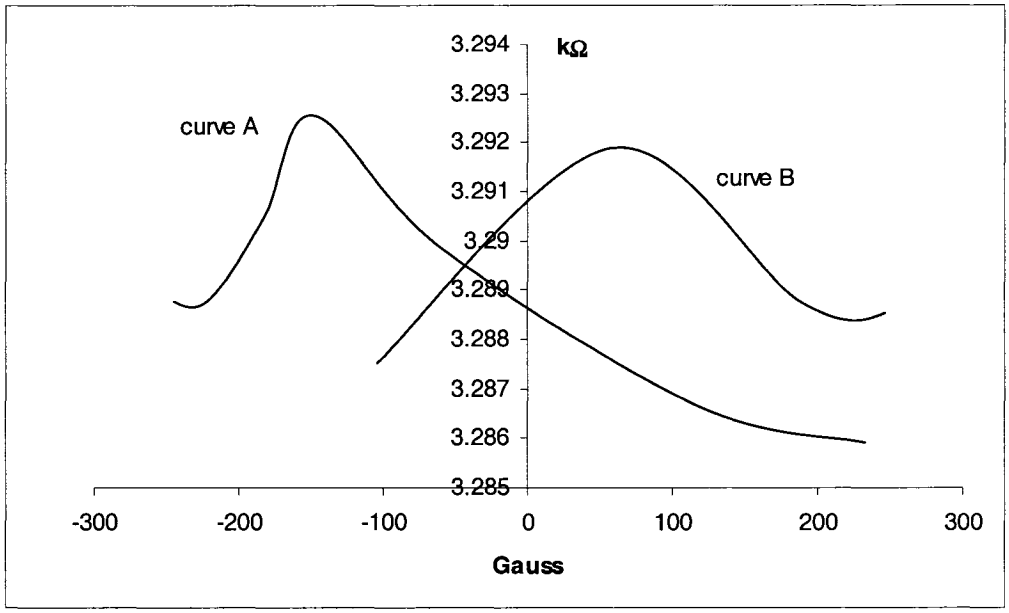

(a) Before annealing

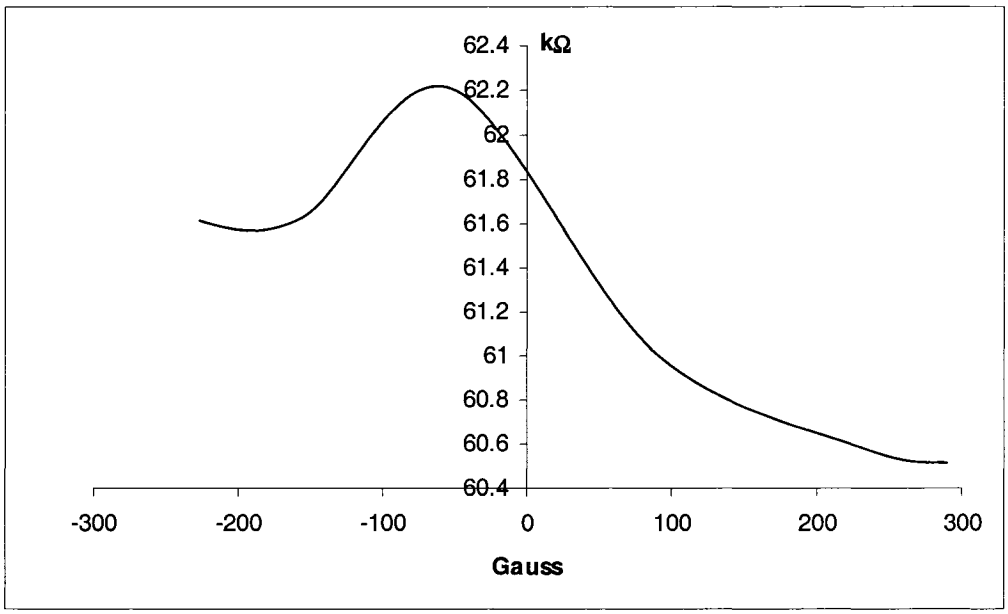

(b) After annealing

Figure 5.15 Tunneling junction resistances vs. magnetic field curves of Sample 7. Curve A represent the variation of the junction resistance vs. magnetic field when the external magnetic field is changed from +200 to -200 Gauss and curve B represent the variation of the junction resistance vs. magnetic field when the external magnetic field is changed from -200 to +200 Gauss.

Sample 8: (2 nm *Al* layer 12 % nitrogen reactive sputtering)

The variation of tunneling junction resistances vs. magnetic field of Sample 8, before annealing is shown in Figure 5.16.

Sample 8 is processed by the nitrogen reactive sputtering. After annealing, the sample shows some increase in the *TMR* ratio, but the tunneling resistance is very high (several hundreds mega-ohms), which is not suitable in any circuit design.

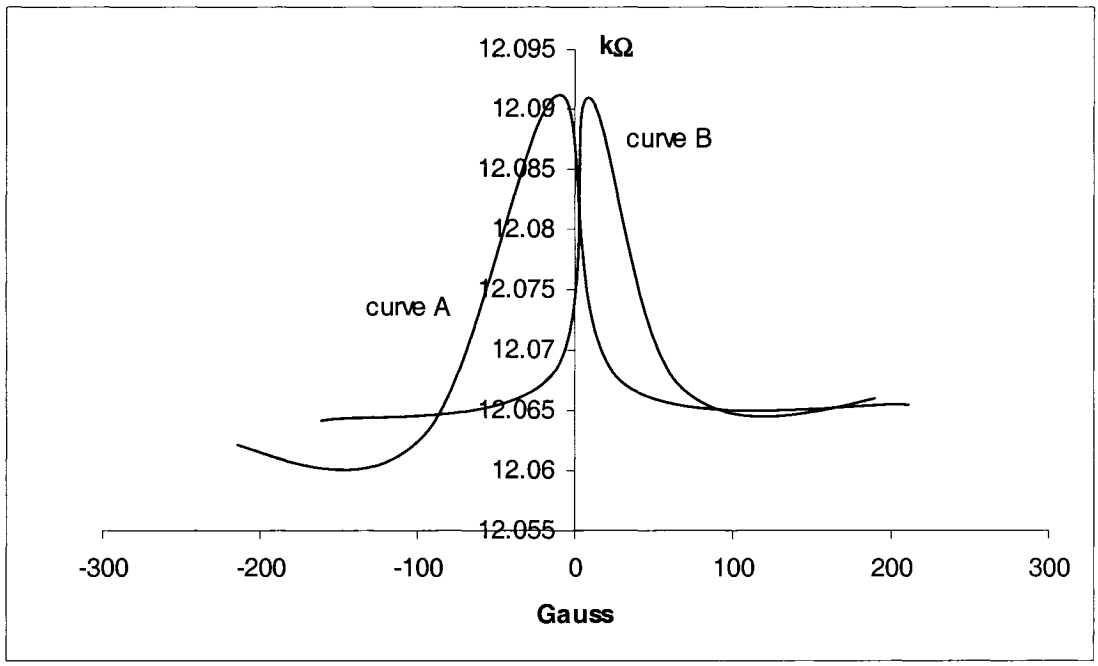

Before annealing

Figure 5.16 Tunneling junction resistances vs. magnetic field curve of Sample 8. Curve A represent the variation of the junction resistance vs. magnetic field when the external magnetic field is changed from +200 to -200 Gauss and curve B represent the variation of the junction resistance vs. magnetic field when the external magnetic field is changed from -200 to +200 Gauss.

5.3.3 Summary

Observing the tunneling resistances vs. magnetic field for all the samples discussed above, some peaks appear close to the vertical axis (at a small magnetic field) and the others away from the vertical axis (at a large magnetic field); this is caused by the different thickness of $Co_{70}Fe_{30}$ and $Ni_{80}Fe_{20}$ layers. The thickness of these layers can not be precisely controlled during the fabrication due to the hardness of these materials. A thin layer switches its magnetic state easier than a thick layer, which results in a peak close to the vertical axis.

The peaks of nitrogen processed samples have almost equal heights and symmetrical shape. The peaks of oxygen processed samples have unequal heights and asymmetrical shape.

Table 5 shows the *TMR* ratio of the samples before and after annealing process. Most of the samples show a good effect of the annealing process. The *TMR* ratios increase from two times to ten times. Observing Table 5, it can be seen that Sample 3 and Sample 5 have the largest *TMR* ratios, 27.93 % and 23.97 % after the annealing process, which are 5.62 and 8.65 times larger than the corresponding *TMR* ratios before the annealing process; these two samples both are aluminium nitridized.

Table 5 The *TMR* results of the samples before and after annealing processes

Sample	*TMR* before annealing	*TMR* after annealing
Sample 1 (*Al* layer oxidized in pure oxygen)	17.24%	4.77%
Sample 2 (*Al* layer oxidized in atmosphere)	1.71%	12.96%
Sample 3 (*Al* layer nitridized for 30 min.)	4.97%	27.93%
Sample 4 (*Al* layer nitridized for 15 min.)	2.92%	1.90%
Sample 5 (*Al* layer nitridized for 5 min.)	2.77%	23.97%
Sample 6 (*Al* layer oxygen reactive sputtered)	6.25%	13%
Sample 7 (*Al* layer oxygen reactive sputtered)	0.34%	3.17%
Sample 8 (*Al* layer nitrogen reactive sputtered)	0.91%	N/A

In Sample 2, Sample 6 and Sample 7, *Al* layer were oxidized by different methods. Many groups have worked on these methods. The results of this research agree with the results of other groups, but the *TMR* ratios are relatively lower. The cause of the lower *TMR* ratios is due to the thick insulating layer (2.4 nm); according to the solution of the Schrodinger's wave equation, the transmission coefficient is inverse proportional to the thickness of the insulating layer. The annealing process improves the *TMR* ratios.

The final value of the *TMR* ratio should be determined by the spin polarization or a well defined magnetic configuration contrast (parallel and anti-parallel alignments of ferromagnetic magnetic electrode magnetizations), and it is also influenced by the interface properties.

The disadvantage of the *AlN* insulating layer tunneling junction is the high resistance. Comparing the results of devices with Al_2O_3 layer tunneling junctions have relatively smaller resistance, several kilo-ohms, while *AlN* layer tunneling junctions have a large resistance, in the range of mega-ohms. In MTJ design, resistance-area product (RA) is another important parameter. A higher *TMR* ratio (usually larger than 30 %) and a lower RA value (less than $100\,k\Omega\mu m^2$) are the most desirable. Large resistance means a large time delay ($\tau = RC$), which is not favourable in circuits design.

The reactive sputtering is not successful. The *TMR* ratio is not large enough and the tunneling resistance is too large.

5.4 Current-voltage (I ~ V) Characteristic Measurements

5.4.1 I ~ V characteristic measurement setting

The arrangement of the I ~ V characteristic measurements of the tunneling junction is schematically shown in Figure 5.17. Two micro-needle probes touch the surface of extended contacts as mentioned before. The samples and the probes were placed in HP 16055A Test Fixture to avoid the high frequency interference during the measurement. The input and output terminals of the Test Fixture were connected to the Keithley 2400 Sourcemeter. A computer was used to connect to the Sourcemeter via a GPIB card to program the operation of the Sourcemeter and to store the measured data. The measurements were done at room temperature. The measured data are presented in Appendix B.

Sourcemeter provides precision voltage and current sourcing as well as measurement capabilities. It is both a highly stable DC power source and a true digital multimeter. The power source characteristics include low noise, precision, and read back. The multimeter capabilities include high repeatability and low noise. In operation, it can act as a voltage source, a current source and a multimeter. Source voltage starts from 5 μV to 210 V and measure voltage starts from 1 μV to 211 V. In this experiment, the applied voltage started from 0 V to 500 mV. The voltage changed with increment of 10 mV. The current of the tunneling junction corresponding to these voltages were measured. All the Sourcemeter settings and measured data were stored in the computer for future analysis. The measurements are able to run automatically once the program is set. Based on the analyses given in Chapter 2, the tunneling current density at T = 0 K through an arbitrary barrier with an average barrier height of φ and barrier thickness a is given by

$$J = J_0\left\{(\phi - V/2)\exp[-A(\phi - V/2)^{1/2}] - (\phi + V/2)\exp[-A(\phi + V/2)^{1/2}]\right\} \quad (2.7)$$

This formula shows that the tunneling current will increase with increasing voltage exponentially if the other conditions are kept constant.

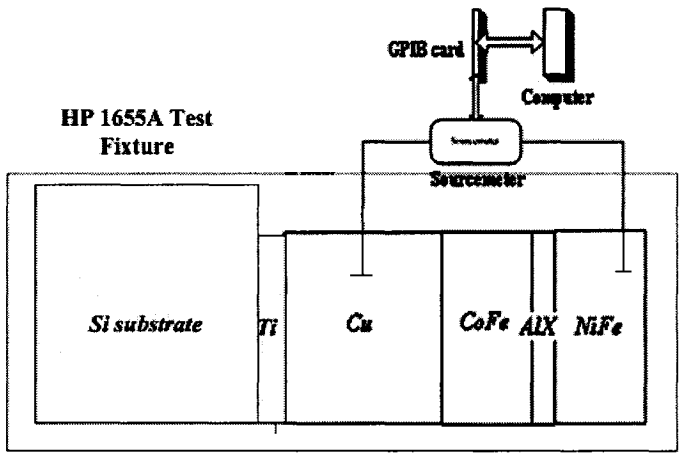

Figure 5.17 Set up of I ~ V characteristic of the tunneling junction

5.4.2 I ~ V characteristic measurements, results and discussion

Based on equation (2.7), the quality of the tunnel junction can be verified by current-voltage characteristic measurements. If the I ~ V characteristic curve is not an exponential curve, the current will not be due to tunneling and the electrodes may be shorted

Sample 1:

I ~ V curves of Sample 1, before and after annealing, are shown in Figure 5.18. The curves are not smooth and at some points the current goes to negative, possibly because of the noise signal. Although the device was placed in a test fixture to avoid high frequency noise, there is still possible some noise signal is involved into the measurement setting.

From the tendency of the curves, the current increases exponentially with increasing the voltage. After annealing, the current increases also exponentially as the voltage increases from 200 mV to 500 mV.

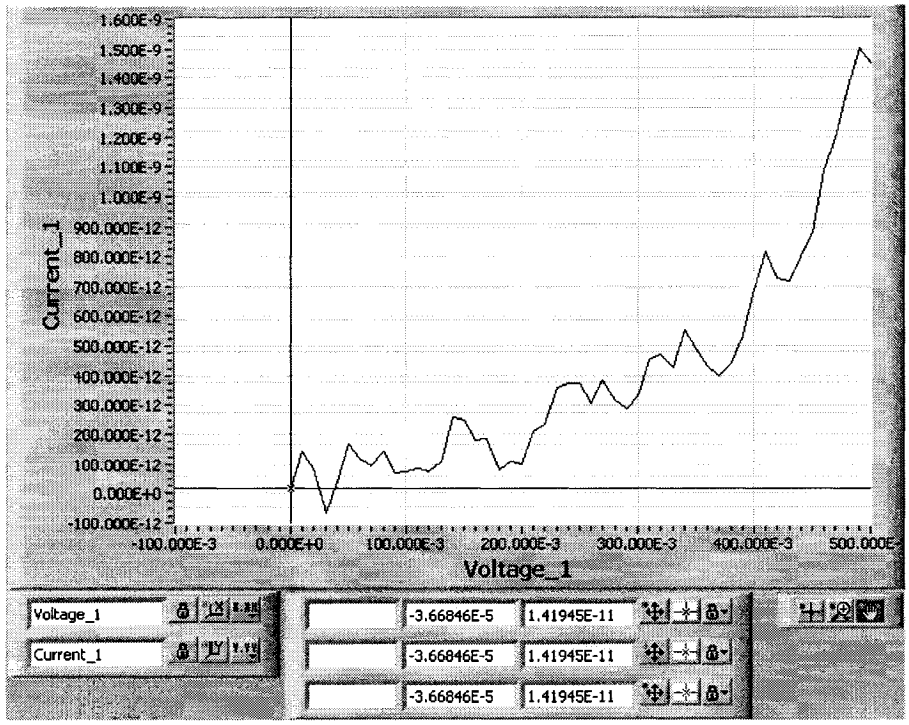

(a) Before annealing

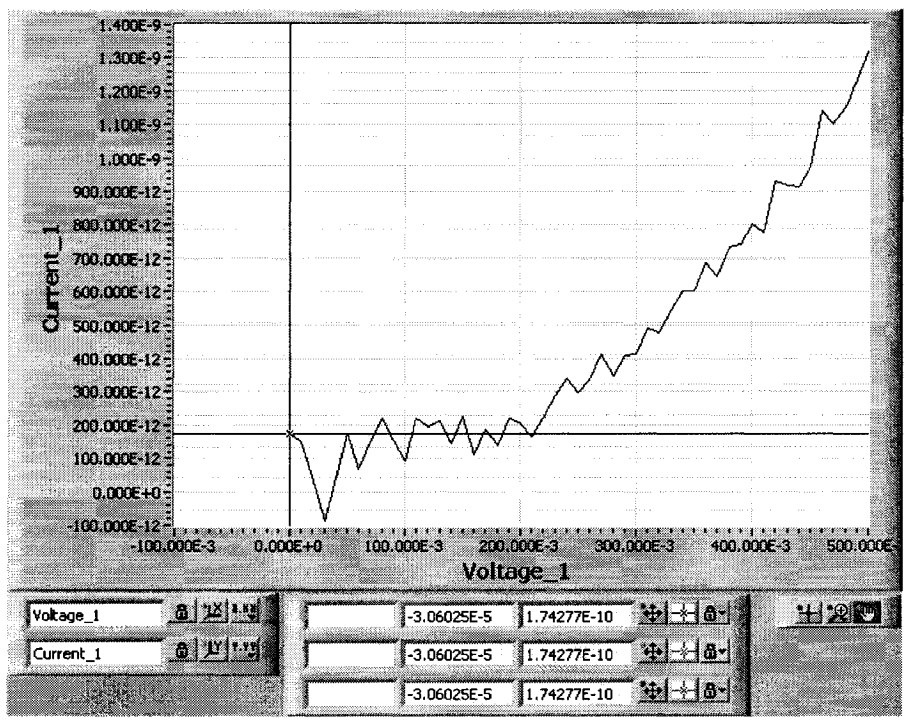

(b) After annealing

Figure 5.18 I ~ V characteristic curves of Sample 1

Sample 2:

I ~ V curves of Sample 2, before and after annealing, are shown in Figure 5.19. In Figure 5.19 (a), when the voltage increases from 0 V to 20 mV, the current increases from 0 A to 0.2 nA and then increases slowly. This current jump may be caused by pinholes inside the insulating layer. Once a voltage is applied on the device, the thin insulating layer experiences a high electrical field; pinholes may be conducted by this high electrical field and cause a current jump. The fact that increasing the voltage causes the current to increase exponentially shows that tunneling is dominated in this device.

After annealing, the I ~ V curve shows an exponential increase, and no sudden jump in the current were observed which means that the annealing process can remove some pinholes in aluminium oxidation layer. The current is also reduced by three orders of magnitude showing the good effect of the annealing process.

Sample 3:

I ~ V curves of Sample 3, before and after annealing, are shown in Figure 5.20. Typical exponential I ~ V characteristic curves show that as the voltage increases from 0 V to 500 mV, the tunneling current increases exponentially. At low bias, the current is very small (10^{-10} A) and flat, so the conductance is nearly independent of the bias up to about 100 mV. As explained in Chapter 2, at a very low biasing voltage, the I ~ V characteristic must be linear. This relationship is true for all the samples when tunneling is not dominant at low bias voltage.

$$J = J_0 V(A\phi^{1/2}/2 - 1)\exp(-A\phi^{1/2}) \qquad (2.8)$$

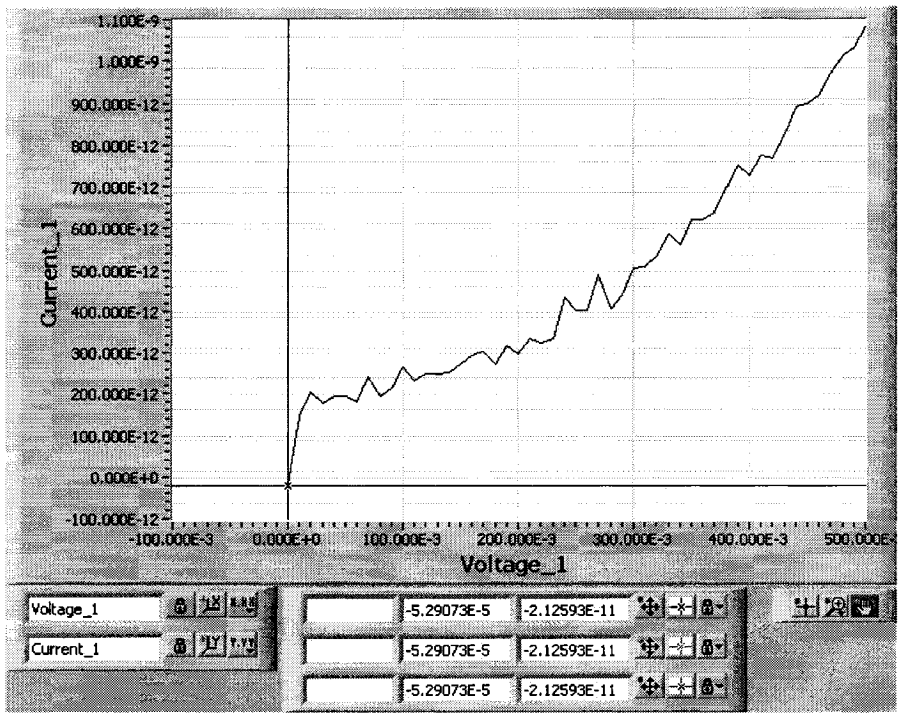

(a) Before annealing

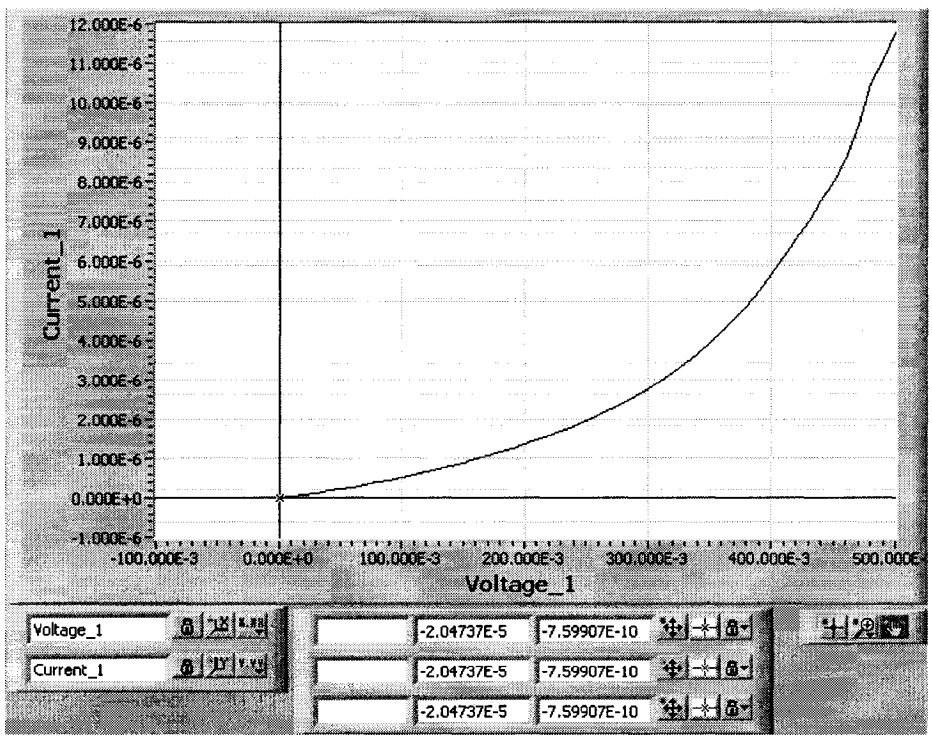

(b) After annealing

Figure 5.19 I ~ V characteristic curves of Sample 2

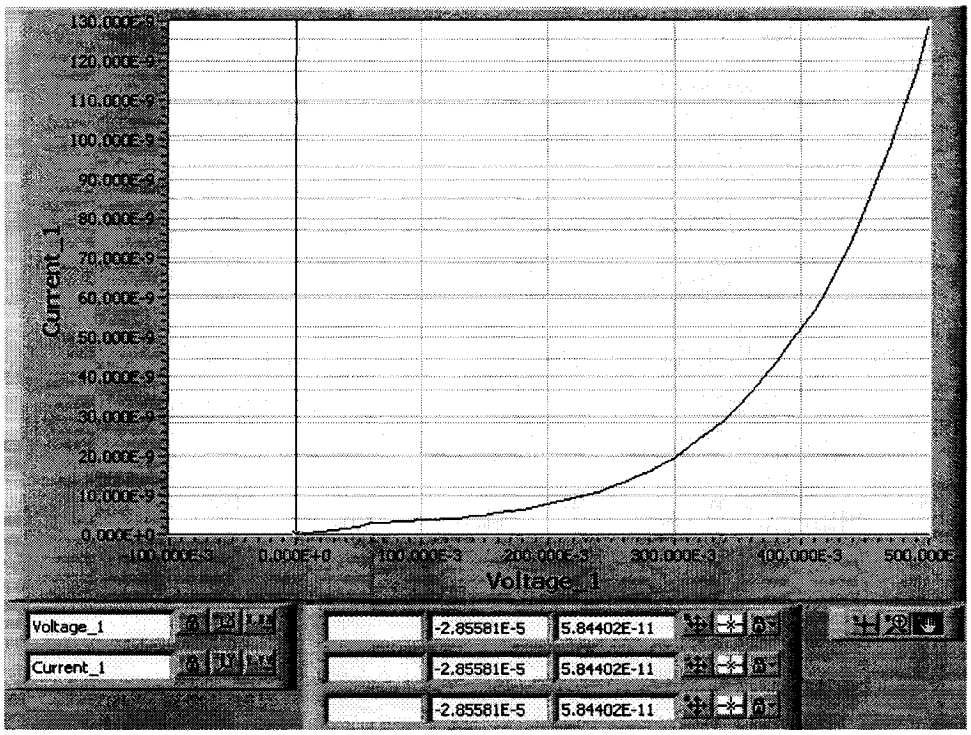

(a) Before annealing

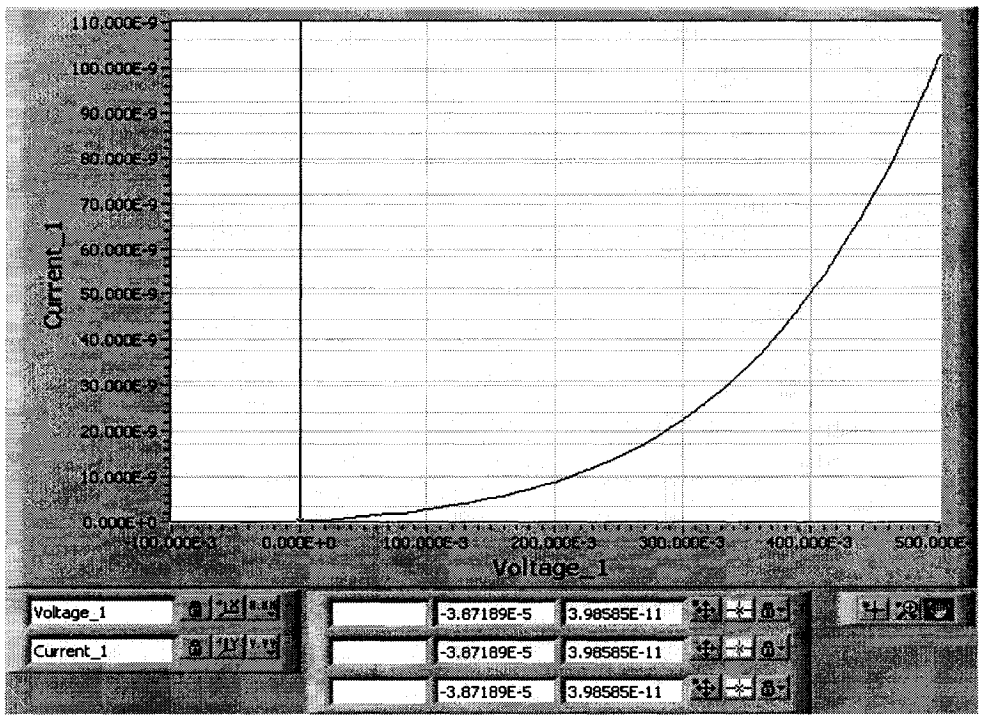

(b) After annealing

Figure 5.20 I ~ V characteristic curves of Sample 3

At the higher bias region, from 100 mV to 500 mV, an exponential dependence of conductance is observed. The I ~ V characteristic curves fitted the exponential relationship of the I ~ V in Equation (2.7) of tunneling. The current–voltage characteristic curve shows that tunneling is the major conduction process.

Sample 4:

I ~ V curves of Sample 4, before and after annealing, are shown in Figure 5.21. Sample 4 may have some defects during the fabrication, both the tunneling resistance vs. magnetic field and I ~ V characteristic measurement are not consistent with the theoretical prediction. The I ~ V characteristic curve, before annealing, shows both noise and pinholes effects. The current is very low compared with other samples. After annealing, the I ~ V curve shows almost a straight line which means there is a less tunneling effect. The *TMR* ratios in Table 5 are only 2.9% and 1.9% before and after annealing. The current in the sample is not fully due to the tunneling.

Sample 5:

I ~ V curves of Sample 5, before and after annealing, are shown in Figure 5.22. The curves are very close those corresponding to Sample 3. There are less noise and pinholes effects, and the tunneling effect is dominant. After annealing, the curve is smooth which shows a good effect of the annealing process. The *TMR* ratios in Table 5 demonstrate the good quality of the tunneling junction.

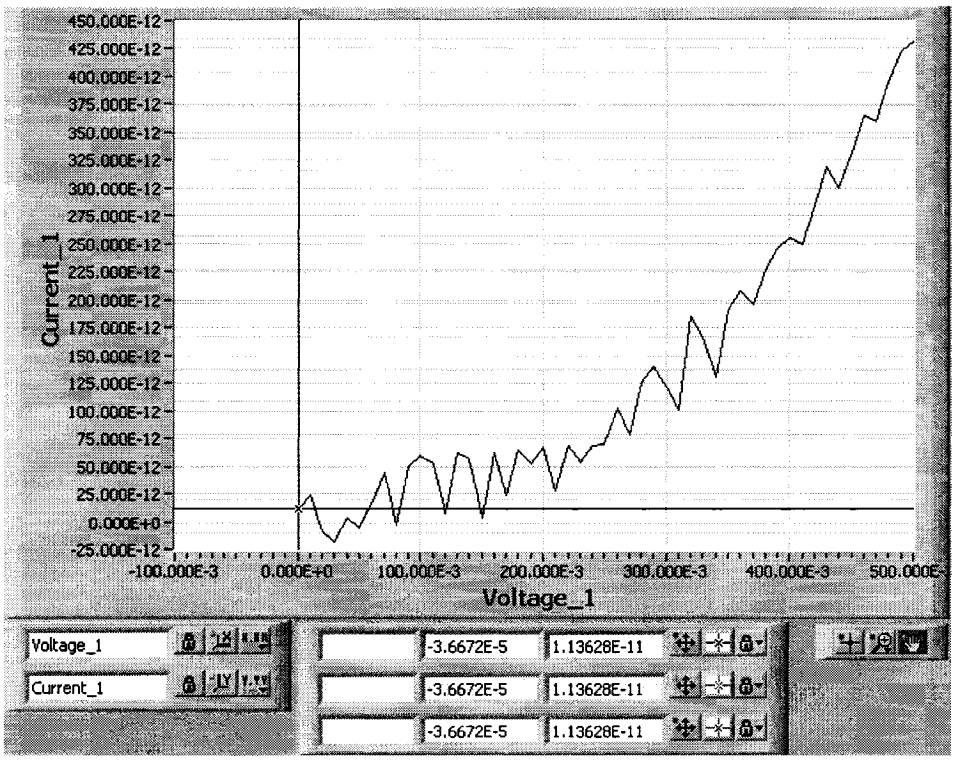

(a) Before annealing

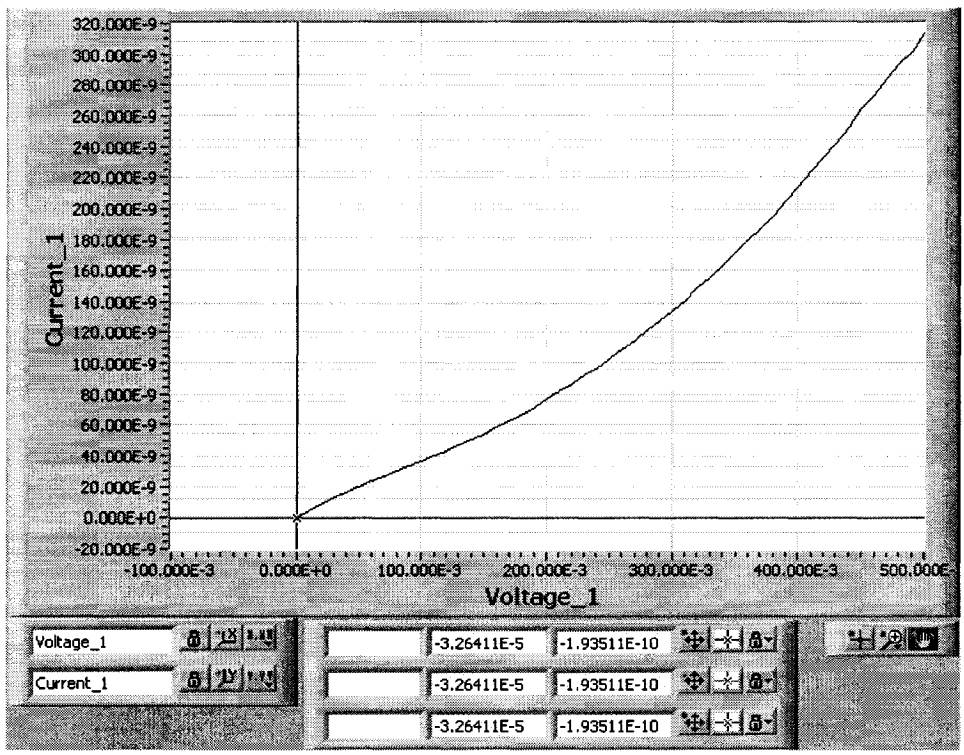

(b) After annealing

Figure 5.21 I ~ V characteristic curves of Sample 4

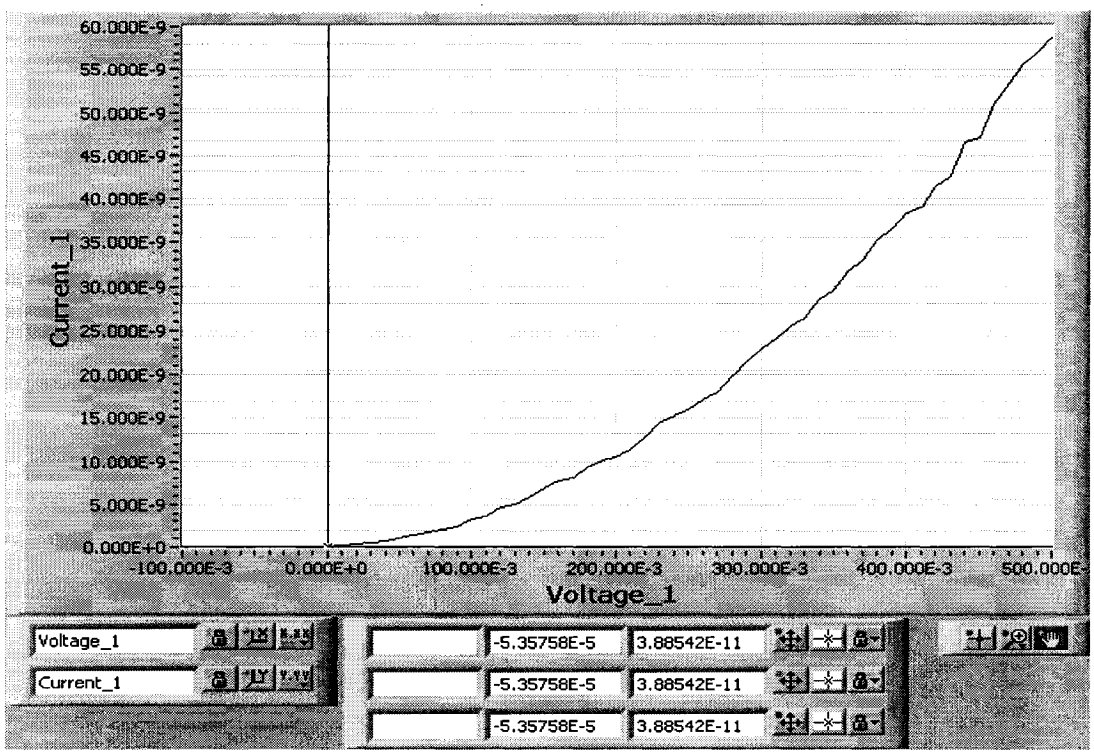

(a) Before annealing

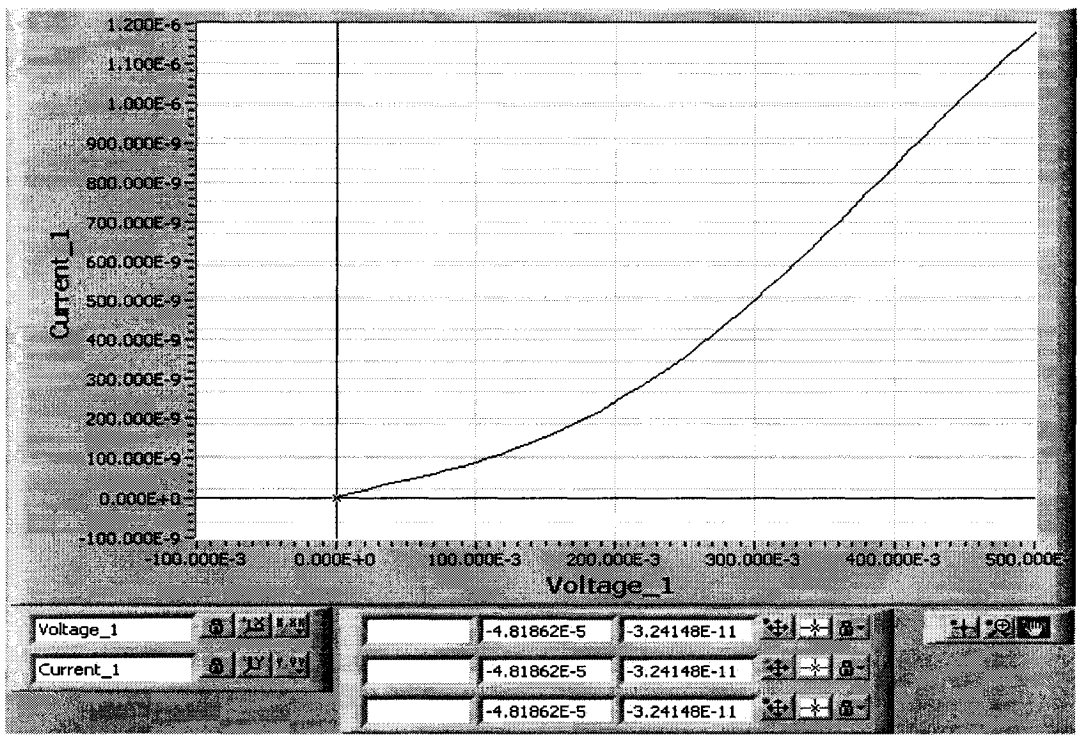

(b) After annealing

Figure 5.22 I ~ V characteristic curves of Sample 5

Sample 6:

I ~ V curves of Sample 6, before and after annealing, are shown in Figure 5.23. The results for the sample before annealing show that when the applied voltage is less than 430 mV the curve is exponential; however, for the applied voltage greater than 430 mV the current drops suddenly. The sudden change in current could be due to some pinholes existing inside the insulating layer. After annealing, the curve closes to a straight line; the resistance of the junction becomes a constant. Although we can find the maximum and minimum resistances as the external magnetic field changes, we can conclude that this is not a very successful tunneling junction.

Sample 7:

I ~ V curves of Sample 7, before and after annealing, are shown in Figure 5.24. Before and after annealing curves are close to straight lines, so the tunneling of carries through the insulating layer failed, although after the annealing some tunneling is observed.

Sample 8:

I ~ V curves of Sample 8, before and after annealing, are shown in Figure 5.25. Before annealing, the I ~ V characteristic curve shows a correct exponential increase curve, indicating a good tunneling effect through the sample. However, after annealing, the curve becomes a straight line that means that there is no tunneling junction between the top and the bottom electrodes. According to the results and the discussion in section 5.3.2, the resistance becomes very large. The annealing process of the tunneling junction is also not successful.

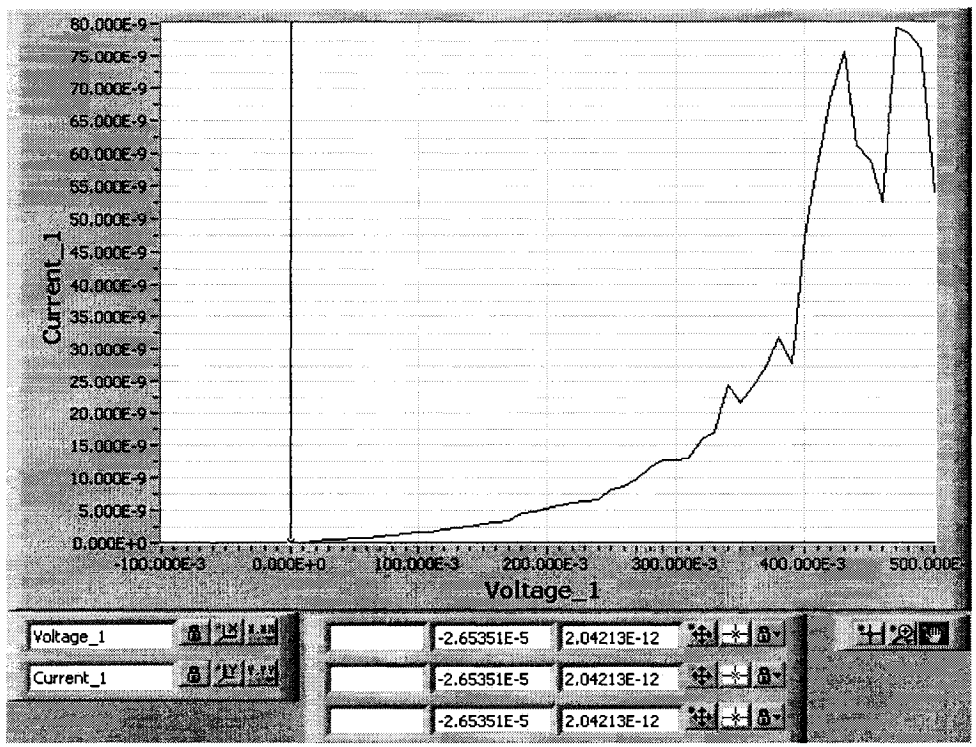

(a) Before annealing

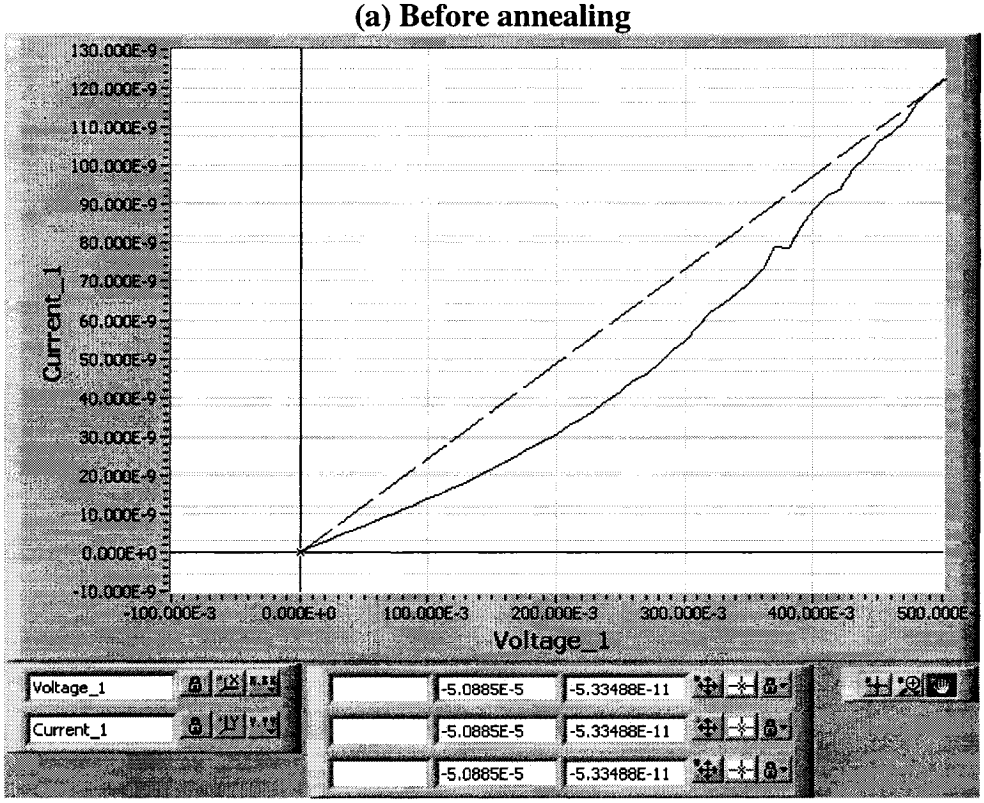

(b) After annealing

Figure 5.23 I ~ V characteristic curves of Sample 6

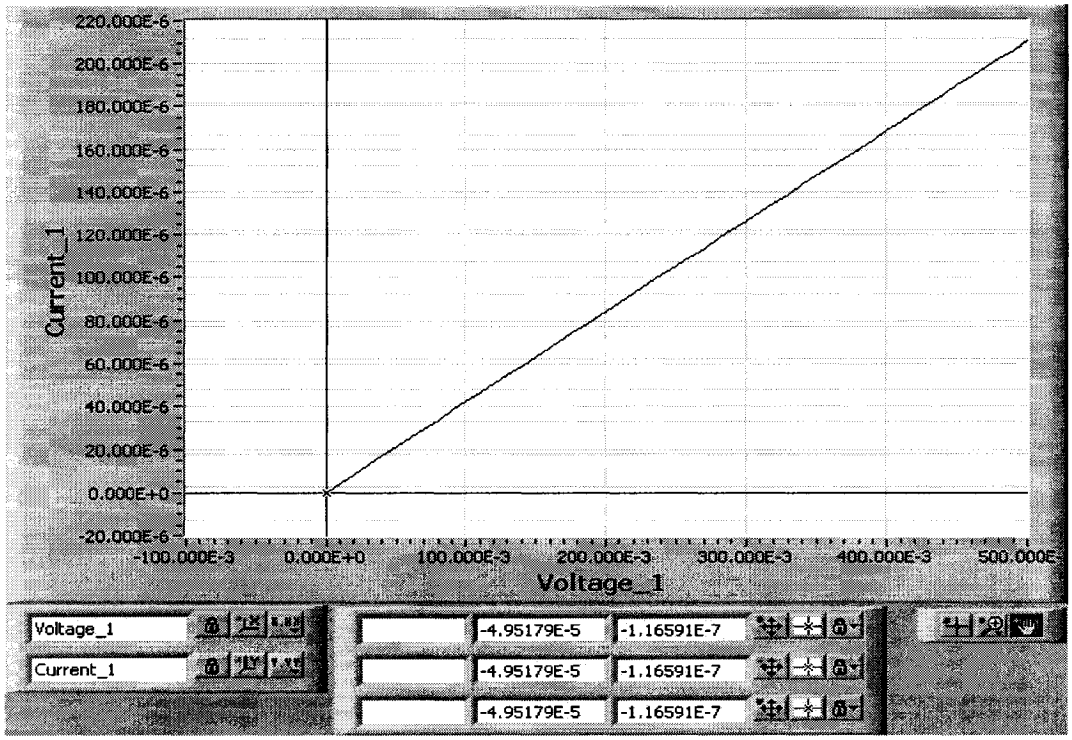

(a) Before annealing

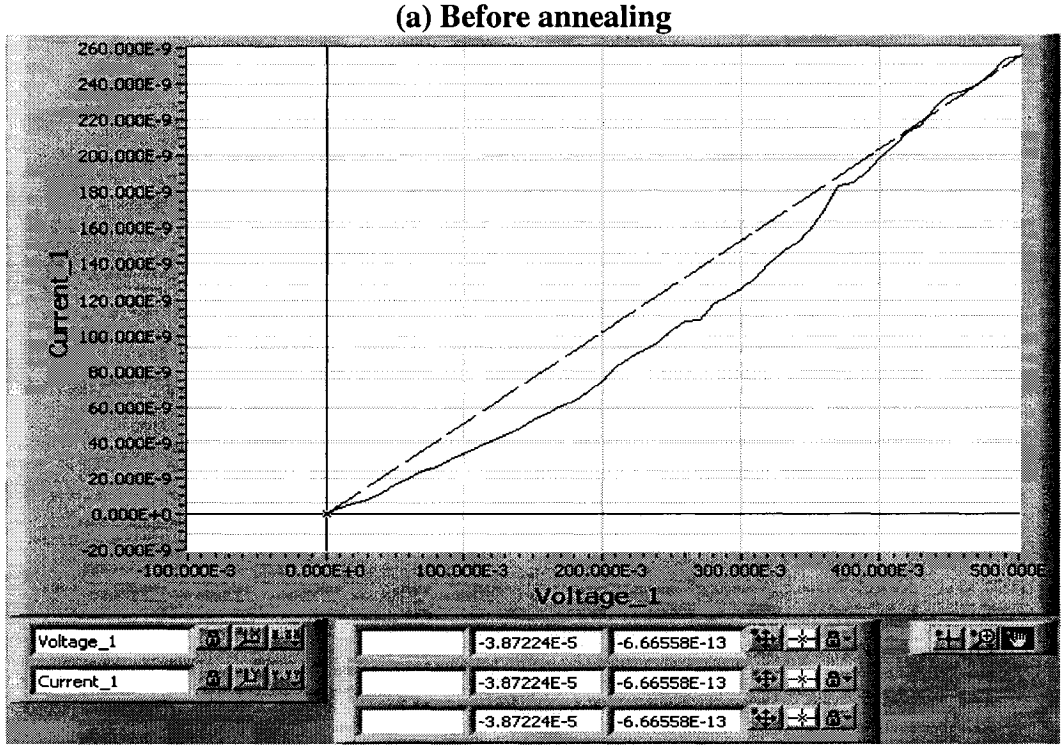

(b) After annealing

Figure 5.24 I ~ V characteristic curves of Sample 7

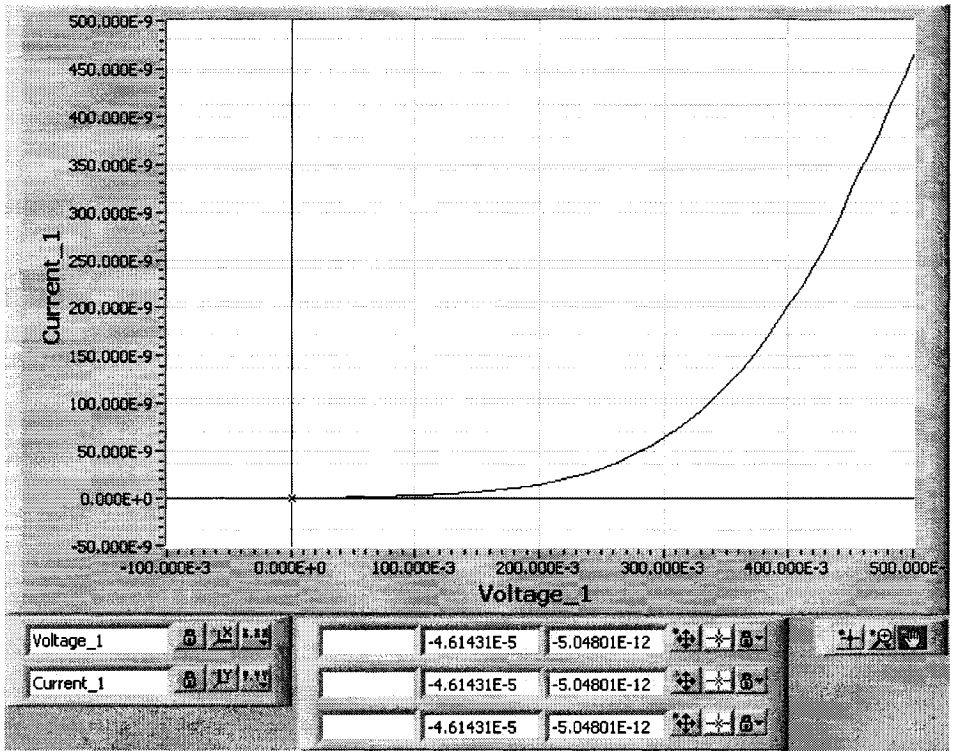

(a) Before annealing

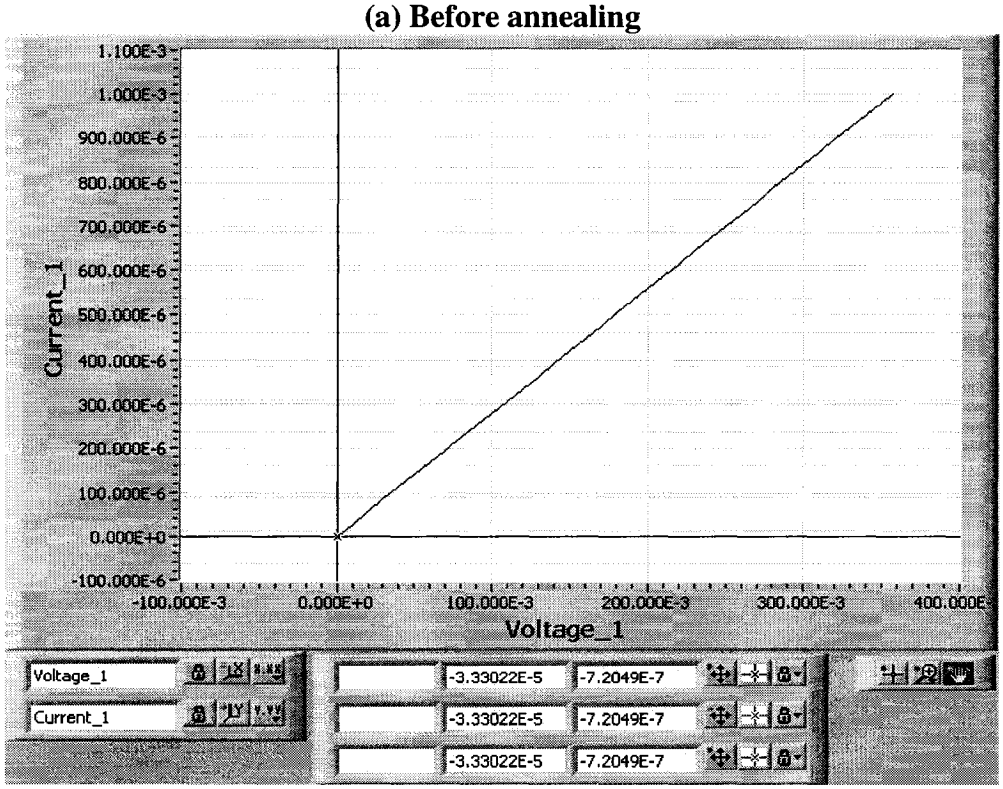

(b) After annealing

Figure 5.25 I ~ V characteristic curves of Sample 8

5.4.3 Summary

Most of the current-voltage curves show the exponential increase of currents as the voltages increase, except for Sample 7 and Sample 8. The results for some of the samples (Sample 1, Sample 2 and Sample 4) show that these samples suffer the pinholes effect. The annealing process improves the performance of the tunneling junctions very much; it reduces the magnitude of the noise, made the curves smoother and caused an increase in current. Generally, I ~ V curves of *AlN* have less defects compare to those of Al_2O_3.

CHAPTER 6

CONCLUSIONS

6.1 Research Conclusions

In this work, $Co_{70}Fe_{30}/AlX/Ni_{80}Fe_{20}$ structure magnetic tunneling junctions were designed, fabricated and characterized. *Al* layers were oxidized in a pure oxygen environment, in air and in 12% oxygen reactive sputtering, and *Al* layers were nitridized in a pure nitrogen environment for different periods of time and in 12% nitrogen reactive sputtering. The tunneling junction resistances vs. different magnetic strengths and field orientations were investigated; current-voltage characteristics of the junctions were measured from 0 V to 500 mV by a Sourcemeter. After the initial measurements, the samples were annealed at 200°C in a nitrogen environment for 30 minutes and characterized again. The tunneling resistances vs. magnetic field and the I~V characterization results were compared and discussed.

Based on the results of measurements, the followings are concluded:

- The fabricated magnetic tunneling junctions show that the tunneling junction resistances altered as the strength and the orientation of the external magnetic field changed. The current-voltage characteristic curves confirmed the tunneling currents through the junctions. At low bias voltage (0 V to 100 mV) there is less tunneling; the junction conductance is independent on the applied voltage and the I ~ V relationship is linear. At high bias voltage (100 mV to 500 mV), electron tunneling starts and the current increases exponentially as the bias voltage

increases. This demonstrates that the design and the fabrication of *MTJ*s were successful in this research.

- *Al* layers were oxidized / nitridized with different techniques and the results were compared and discussed. *AlN* layer has many advantages compared with Al_2O_3 layer. The process of nitridation is relatively slow (usually 5 to 30 minutes) and easy to control compared to the oxidation process (1 to 4 seconds), due to the lower nitrogen diffusion coefficient. As it is shown in Appendix C, in most materials, the diffusivity of oxygen is two to three times greater than that of nitrogen. The samples nitridized in a pure nitrogen environment have a higher *TMR* ratio. The annealing process improves the performance of the *TMR* ratio (up to 27 % at room temperature).

Finally, we can conclude that the nitridation of *Al* layers in a pure nitrogen environment results in a higher *TMR* ratios and less pinholes effect than in oxidation processes.

6.2 Contributions

The main contributions of this research are listed below:

- In this work, we designed and fabricated *MTJ*s with only five layers ($Ti/Cu/Co_{70}Fe_{30}/AlX/Ni_{80}Fe_{20}$) compared to those reported in the literature, [4] [6] [16] which used up to twelve layers to complete the device. This simple design lead us to focus on the characterizations of insulating layer and to eliminate the effects caused by the other layers.

- The simple design leads to a simple fabrication; some of the fabrication steps, *Cu* on *Ti* and *Al* on *CoFe*, can be done *in situ* to avoid contamination and oxidation.
- Because the fabrication was simple, the problems involved in design, in fabrication and in characterization can be solved quickly once the sample was fabricated.
- The junction resistances vs. magnetic field and the I ~ V characteristic were investigated and plotted.
- The two sets of results (before and after annealing process) were discussed, compared.

6.3 Future Works

To improve the *TMR* ratio of *MTJ*s, a lot of works has to be done in the future. Below are some suggestions for future works.

- To avoid any contamination from outside of the sputtering chamber, it is better to sputter the different layers *in situ*. A multi-gun sputtering system is needed for the multilayer *in situ* fabrication.
- Ferromagnetic material sputtering is very difficult in our sputtering system, especially for the thick layer deposition. For a thick layer sputtering, a special sputtering gun is needed to avoid the cancellation of the magnetic field inside the magnetron gun.
- In *Al* sputtering, a lower sputtering rate is expected in order to precisely control the thickness in a few angstroms.

REFERENCES

[1] W. J. Gallagher and S. S. P. Parkin, "Development of the magnetic tunnel junction MRAM at IBM: From first junctions to a 16-Mb MRAM demonstrator chip," *IBM Journal of Research & Development*, vol. 50, No. 1, pp. 5-20, January 2006.

[2] Saied Tehrani, Jon M. Slaughter, Mark DeHerrera, Brad N. Engel, Nicholas D. Rizzo, John Salter, Mark Durlam, Renu W. Dave, Jason Janesky, Brian Butcher, Ken Smith, and Greg Grynkewich, "Magnetoresistive Random Access Memory Using Magnetic Tunnel Junctions," *Proceedings of the IEEE*, vol. 91, No. 5, pp. 703-712, May 2003.

[3] S. Tehrani, B. Engel, J. M. Slaughter, E. Chen, M. DeHerrera, M. Durlam, P. Naji, R. Whig, J. Janesky, and J. Calder, " Recent Developments in Magnetic Tunnel Junction MRAM," *IEEE Transactions on Magnetics*, vol. 36, No. 5, pp. 2752-2757, September 2000.

[4] Brad N. Engel, Nicholas D. Rizzo, Jason Janesky, Jon M. Slaughter, Renu Dave, Mark DeHerrera, Mark Durlam and Saied Tehrani, "The Science and Technology of Magnetoresistive Tunneling Memory," *IEEE Transactions on Nanotechnology*, vol. 1, No. 1, pp. 32-38, March 2002.

[5] S. I. Kasatkin, A. M. Murav'jev, N. V. Plotnkkova, F. A. Pudonin, L. A. Azhaeva, Z. N. Sergeeva, and V. D. Khodzhaev, "Magnetic Nanostructures and Nanodevices with a Semiconductor or Dielectric Spacer," *Russian Microelectronics*, vol. 34, No. 1, pp. 47-53, 2005.

[6] Satoru Yoshimura, Toshihiro Shoyama, Toshiharu Nozawa, Masakiyo Tsunoda, and Migaku Takahashi, "Nitridation Process of Al Layer by Microwave-Excited Plasma and Large Magnetoresistance in Co-Fe/Al-N/Co-Fe Tunnel Junctions – As a Comparison With Oxidization Process," *IEEE Transactions on Magnetics*, vol. 40, No. 4, pp. 2290-2292, July 2004.

[7] Donald A Neamen, "Semiconductor Physics and Devices," 2nd, *McGraw-Hill Companies, Inc.* 1997.

[8] E. Y. Chen, R. Whig, J. M. Slaughter, D. Cronk, J. Goggin, G. Steiner, and S. Tehrani, "Comparison of oxidation methods for magnetic tunnel junction material," *Journal of Applied Physics*, vol. 87, No. 9, pp. 6061-6063, May 2000.

[9] J. M. De Teresa, A. Barthelemy, J. P. Contour, and A. Fert, "Role of the Barrier in Magnetic Tunnel Junctions," http://www.mariecurie.org/annals/volume1/deteresa.pdf as of April 17, 2007.

[10] M. Jullière, "Tunneling between ferromagnetic films," *Physics Letters A*, vol. 54, Issue 3, pp. 225-226, 1975.

[11] E. Snoeck, V. Serin, R. Fourmeaux, Z. Zhang and P. P. Freitas, "Transmission Electron Microscopy evidence of the growth of a magnetite layer acting as a spin filter in CoFe/Al_2O_3/CoFe magnetic tunnel junctions," *Journal of Applied Physics*, vol. 96, No. 6, pp. 3307-3311, September 2004.

[12] C. H. Ho, Minn-Tsong Lin, Y. D. Yao, S. F. Lee, C. C. Liao, F. R. Chen, and J. J. Kai, "Magnetoresistance of spin-dependent tunnel junctions with composite electrodes," *Journal of Applied Physics*, vol. 90, No. 12, pp. 6222-6225, December 2001.

[13] Takahiro Moriyama, "MTJ RAM design," University of Delaware, Physics and Astronomy, 2003.

[14] B. N. Engel, J. Akerman, B. Butcher, R. W. Dave, M. DeHerrera, M. Durlam, G. Grynkewich, J. Janesky, S. V. Pietambaram, N. D. Rizzo, J. M. Slaughter, K. Smith, J. J. Sun, and S. Tehrani, "A 4-MB Toggle MRAM Based on a Novel Bit and Switching Method," *IEEE Transactions on Magnetics*, vol. 41, No. 1, pp. 132-136, January 2005.

[15] Heejae Shim, J. M. Park, K. P. Kim, B. k. Cho, and Jin-Tae Kim, "Magnetic tunnel junctions with a tunnel barrier formed by N_2O plasma," *Applied Physics Letter*, vol. 83, No. 22, pp. 4583-4585, December 2003.

[16] Masakiyo Tsunoda, Kazuhiro Nishikawa, Satoshi Ogata, and Migaku Takahashi, "60% magnetoresistance at room temperature in Co-Fe/Al-O/Co-Fe tunnel junctions oxidized with Kr-O_2 plasma," *Applied Physics Letters*, vol. 80, No. 17, pp. 3135-3137, April 2002.

[17] http://www.erc.arizona.edu/education/MME%20Course%20Materials/MME%20Modules/Surface%20Prep%20Module/Wet%20Etching%20and%20Cleaning%20-%20Surface.ppt#263,14,Standard Clean for Silicon, as of April 17, 2007.

[18] James D. Plummer, Michael Deal, Peter B. Griffin, "Silicon VLSI technology: fundamentals, practice and modeling," *Upper Saddle River, NJ: Prentice Hall*, 2000

[19] "The Reactive DC-Magnetron Sputtering Process," http://ia.physik.rwth-aachen.de/research/sputtering/www-sputter-eng.pdf as of April 17, 2007.

[20] S. Miura, D Takahashi, M. Tsunoda and M. Takahashi, "Influence of Impurity Gas in the Sputtering Atmosphere on the Microstructure and the GMR in Co/Cu Multilayers," *IEEE Transactions on Magnetics*, vol. 34, No. 4, pp. 936-938, 1998.

[21] Michael Ziese and Martin J. Thornton, "Spin Electronics," *Berlin, New York, Springer,* c2001.

[22] D. C. Hurley, M. Kopycinska-Muller, E. D. Langlois, A. B. Kos, and N. Barbosa III, "Mapping substrate/film adhesion with contact-resonance-frequency atomic force microscopy," *Applied Physics Letters*, vol. 89, No. 2, July 10, 2006.

[23] http://hardness-testers.globalspec.com/Industrial-Directory/material_hardness as of April 17, 2007.

[24] Samuel D. Ekpe, Louis W. Bezuidenhout, and Steven K. Dew, "Deposition rate model of magnetron sputtered particles," *Thin Solid Film*, vol. 474, pp. 330-336, 2005.

[25] http://pvd-coatings.co.uk/theory-of-pvd-coatings-magnetron.htm as of April 17, 2007.

[26] http://www.aacg.bham.ac.uk/magnetic_materials/ as of April 17, 2007.

[27] http://www.gencoa.com/eNews/aug/loopmail.html as of September 28, 2006.

[28] F.Montaigne, J. Nassar, A. Vaures, F. Nguyen Van Dau, F. Petroff, A. Schuhl, and A. Fert, "Enhanced tunnel magnetoresistance at high bias voltage in double-barrier planar junctions," *Applied Physics Letters*, vol. 73, Issue 19, pp. 2829-2831, Nov. 1998.

[29] http://en.wikipedia.org/wiki/Hysteresis as of April 17, 2007.

[30] K. H. Shin, C. D. Graham, Jr. and Peter Y. Zhou "Asymmetric Hysteresis Loops in Co-based Ferromagnetic Alloys," *IEEE Transactions on Magnetics*, vol. 28, No. 5, pp. 2772-2774, September, 1992.

[31] Jagadeesh S. Moodera and Lisa R. Kinder "Ferromagnetic-insulator-ferromagnetic tunneling: Spin-dependent tunneling and large magnetoresistance in trilayer junctions," *Journal of Applied Physics,* vol. 79, No. 8, pp. 4724-4729, April 1996.

APPENDICES

APPENDIX A: Tunneling junction resistances vs. magnetic field and the *TMR* ratios

APPENDIX B: I ~ V characteristic measurements of the samples

APPENDIX C: Oxygen, nitrogen and hydrogen diffusivity

APPENDIX A

Tunneling junction resistances vs. magnetic field

and the *TMR* ratios

Sample 1:

Magnetic Field (Gauss)	Resistance (kΩ)	Resistance (kΩ) After Annealing	Magnetic Field (Gauss)	Resistance (kΩ)	Resistance (kΩ) After Annealing
0.6	89.1	125.3	91.7	87.5	122.6
0.6	89.5	126.1	57.1	85.8	122.5
8.1	89.7	125.6	4.8	82.5	122.3
9.1	90.3	126.4	0.6	83.4	122.1
14.8	90.6	127.3	-0.2	81.2	122.1
17.5	91.1	127.3	-3.4	82.6	122
21.3	91.5	127.4	-6	83.1	121.8
23.6	92.2	126.3	-21.7	83.5	121.7
34.4	92.5	126.2	-26.5	84.8	121.6
42.9	92.9	124.7	-38.7	85.7	121.8
52.1	93.6	123.1	-55.4	87.2	122.1
62.2	94.4	122.6	-67.4	87.1	122.3
72.3	95.1	122.4	-88.7	86.1	122.5
101.1	95.2	122.1	-105.4	85.4	123.3
102.9	93.7	122	-127.2	83.8	123.1
108.5	92.9	122.1	-151.5	83.2	122.9
113.3	92.5	122.1	-163.7	88.3	122.9
132	92.9	122.2	-171	90.2	123
153.4	92.4	122.3	-178.9	87.7	122.8
164.6	91.6	122.6	-155.1	87.2	122.6
171.6	91.9	122.4	-134.3	85.4	122.5
174.3	83	122.5	-46.2	88.4	121.6
175.5	82.8	124.9	-25.6	86.9	121.8
175	84.6	125	-1.6	85.1	121.9
172.5	86.1	125.3	**Max.**	**95.2**	**127.4**
176.1	81.9	125.2	**Min.**	**81.2**	**121.6**
163.2	81.8	123.3	***TMR***	**17.24%**	**4.77%**

Sample 2:

Magnetic Field (Gauss)	Resistance (kΩ)	Resistance (kΩ) After Annealing
0.4	3.021	65.6
0.9	3.023	65.6
5.2	3.019	64.7
15.7	3.024	63.4
98.8	3.031	62.4
144.9	3.025	62.1
160	3.02	61.9
161.7	3.008	61.6
185.8	2.991	61.6
187.4	2.984	61.6
204.2	3.011	61.5
223.2	3.024	61.5
199.3	2.995	61.6
118.1	2.993	62.1
77.3	2.991	62.5
52.1	3.001	62.6
29.2	3.013	62.2
10.2	3.024	62.1
6.2	3.018	61.9
0.9	3.018	61.7

Magnetic Field (Gauss)	Resistance (kΩ)	Resistance (kΩ) After Annealing
0.4	3.023	61.7
-0.9	3.022	61.5
-4.9	3.022	61.4
-12.6	3.023	60.9
-25.4	3.019	60.8
-50.7	3.019	60.3
-70.1	3.027	59.8
-91.3	3.035	59.5
-105.1	3.032	59.6
-135.5	3.035	59.4
-214.2	3.029	59.4
-223.8	2.996	59.7
-76.7	2.993	60.1
-48	3.013	60.8
-26	3.023	61.8
-16.5	3.03	62.6
-6.3	2.998	64.1
-0.2	2.998	67
0.4	3.001	67.1
Max.	**3.035**	**67.1**
Min.	**2.984**	**59.4**
TMR	**1.71%**	**12.96%**

Sample 3:

Magnetic Field (Gauss)	Resistance (MΩ)	Resistance (MΩ) After Annealing
0.1	23	6.56
17.2	22.9	7.02
33.7	22.95	7.05
86	23.23	7.21
127.1	23.23	7.42
137.2	23.1	7.43
156.3	23.01	7.52
199.4	22.76	7.28
204.3	22.73	7.09
206.2	22.6	7.97
189.9	22.55	7.14
151.5	22.65	7.47

Magnetic Field (Gauss)	Resistance (MΩ)	Resistance (MΩ) After
74.2	23.22	7.49
58.5	23.13	7.23
42.6	23.02	7.04
32.3	22.96	6.77
25.6	22.91	6.68
16.6	22.86	6.64
11.3	22.81	6.57
9.1	22.8	6.47
3	22.82	6.49
0.6	22.91	6.23
-0.7	22.73	6.28
-3.8	22.77	6.29
-13.9	22.79	6.64
-36.3	22.9	6.74
-63.8	23.11	7.04
-179.3	22.57	7.53
-231.2	22.34	6.73

-219.2	22.13	6.73	-42.4	22.95	6.68
-244.5	22.29	6.87	-34.3	22.9	6.44
-200.6	22.47	6.82	-25.3	22.84	6.47
-191.6	22.51	6.82	-20	22.54	6.37
-144.6	22.64	7.43	-17.7	22.82	6.35
-122.3	22.81	7.48	-9.2	22.73	6.28
-112.6	22.91	7.64	-3.9	22.74	6.39
-99.6	23.01	7.76	**Max.**	**23.23**	**7.97**
-85	23.13	7.73	**Min.**	**22.13**	**6.23**
-56.6	23.07	7.01	***TMR***	**4.97%**	**27.93%**

Sample 4:

Magnetic Field (Gauss)	**Resistance (MΩ)**	**Resistance (kΩ) After Annealing**	**Magnetic Field (Gauss)**	**Resistance (MΩ)**	**Resistance (kΩ) After Annealing**
0	0.913	112.86	-19.8	0.909	113.77
1.3	0.912	112.69	-26.2	0.906	113.65
7.1	0.915	112.85	-39.2	0.901	113.25
23.7	0.915	113.03	-62.1	0.9	112.7
80.9	0.915	112.6	-73.3	0.899	112.52
144.3	0.916	112.47	-137.4	0.9	111.71
194.4	0.913	112.33	-204.4	0.9	113.81
229.7	0.91	112.19	-214.6	0.899	113.83
230.2	0.906	112.35	-161.2	0.891	113.76
230.1	0.904	112.39	-38.9	0.894	113.62
234.4	0.9	112.36	-21.1	0.899	113.75
227.6	0.897	112.36	-9.3	0.901	113.73
36.5	0.899	112.68	-0.9	0.9	113.48
25.2	0.902	112.94	1.3	0.898	113.28
20.9	0.904	113.12	4.2	0.897	113.29
5.2	0.904	112.93	11.7	0.896	113.42
0.2	0.906	113.38	20.4	0.895	113.24
-0.2	0.912	113.54	37.9	0.892	112.84
-3.5	0.912	113.63	52.9	0.89	112.43
			Max.	**0.916**	**113.83**
			Min.	**0.89**	**111.71**
			TMR	**2.92%**	**1.90%**

Sample 5:

Magnetic Field (Gauss)	Resistance (MΩ)	Resistance (MΩ) After Annealing	Magnetic Field (Gauss)	Resistance (MΩ)	Resistance (MΩ) After Annealing
0.2	1.315	0.849	-219.8	1.337	0.808
1.3	1.311	0.876	-160.9	1.334	0.835
2.8	1.315	0.88	-51.8	1.314	0.793
11.9	1.315	0.875	-2	1.314	0.777
39.6	1.316	0.88	0	1.316	0.792
67.3	1.314	0.882	0.1	1.318	0.751
57.1	1.306	0.88	0.6	1.319	0.773
169.2	1.32	0.882	6.7	1.322	0.825
172	1.322	0.887	39.2	1.321	0.78
203.1	1.319	0.917	77.6	1.32	0.782
61.5	1.318	0.931	58.5	1.307	0.831
14.3	1.318	0.929	113.9	1.318	0.783
1.7	1.318	0.904	160.2	1.316	0.791
-5.7	1.326	0.884	184.4	1.312	0.806
-31.6	1.321	0.851	217.3	1.32	0.802
-99.2	1.321	0.795	41.7	1.322	0.802
-64.8	1.307	0.799	2.2	1.329	0.807
-62.6	1.301	0.812	0.6	1.336	0.815
-97.6	1.309	0.821	**Max.**	**1.337**	**0.931**
-125.3	1.317	0.813	**Min.**	**1.301**	**0.751**
-170	1.322	0.802	***TMR***	**2.77%**	**23.97%**
-198.3	1.325	0.829			

Sample 6:

Magnetic Field (Gauss)	Resistance (MΩ)	Resistance (kΩ) After Annealing	Magnetic field (Gauss)
0	0.117	52.16	0
-174	0.116	52.7	-1.4
-171	0.115	52.95	-3.2
-170	0.112	53.32	-8.3
-187	0.118	53.46	-72.5
-190	0.119	53.64	-120.2
187	0.118	53.8	-168
-155	0.116	54.18	-177.5
-160	0.115	53.58	-187.1
-156	0.114	53.46	-198.6
-133	0.113	51.8	-204.2
-130	0.112	52.93	-83.3
Max.	**0.119**	51.12	-20.6
Min.	**0.112**	48.32	-3.9
TMR	**6.25%**	47.93	0.2
		48.25	1.9
		48.68	57.3

48.94	136.1
49.72	172.3
49.84	189.9
50.93	196.8
51.32	204.1
51.37	220.9
54.18	**Max.**
47.93	**Min.**
13%	***TMR***

Sample 7:

Magnetic Field (Gauss)	Resistance (kΩ)	Resistance (kΩ) After Annealing	Magnetic Field (Gauss)	Resistance (kΩ)	Resistance (kΩ) After Annealing
56	3.291	60.27	20	3.291	62.06
141.7	3.29	60.35	1.5	3.292	62.15
197.6	3.289	60.44	-0.5	3.291	62.18
237	3.288	60.55	-8.6	3.291	62.16
232.3	3.287	60.6	-50.9	3.29	62.18
229.7	3.286	60.58	-153.4	3.292	61.57
221.3	3.285	60.59	-163.7	3.29	61.67
220	3.284	60.63	-167.4	3.291	61.68
217.3	3.282	60.68	-173.9	3.289	61.74
206.6	3.281	60.75	-200.5	3.288	61.78
203.3	3.282	60.79	-222.7	3.287	61.81
202.4	3.283	60.73	-230.1	3.286	
200.4	3.284	60.79	-225.8	3.285	
194.6	3.285	60.75	-227.8	3.286	
186.7	3.286	60.84	-234.4	3.287	
173.1	3.287	60.82	-239.5	3.288	
163.6	3.288	60.86	-212.1	3.289	61.93
138.5	3.289	60.98	-172.2	3.29	61.92
138.4	3.29	60.99	-112.9	3.291	61.93
101.2	3.291	61.04	-59.7	3.292	62.09
71.2	3.292	61.84	**Max.**	**3.292**	**62.18**
			Min.	**3.281**	**60.27**
			TMR	**0.34%**	**3.17%**

Sample 8:

Magnetic (Gauss)	Field	Resistance (kΩ)		
0.1		12.09	103.8	12.06
5.1		12.09	142.4	12.06
25.5		12.07	212.8	12.06
66.7		12.06	180	12.13
			168.6	12.16
			91	12.06

28	12.08
4.7	12.09
0.2	12.09
-4.6	12.08
-29.9	12.07
-62.7	12.06
-157.5	12.05
-212.9	12.06
Max.	**12.16**
Min.	**12.05**
TMR	**0.91%**

APPENDIX B

I ~ V characteristic measurements of the samples

Sample 1:

Voltage (V)	Current (A) (Before annealing)	Current (A) (After annealing)	Voltage (V)	Current (A) (Before annealing)	Current (A) (After annealing)
-3.67E-05	1.42E-11	1.74E-10	2.50E-01	3.75E-10	2.97E-10
9.96E-03	1.41E-10	1.49E-10	2.60E-01	3.07E-10	3.37E-10
2.00E-02	8.21E-11	4.59E-11	2.70E-01	3.87E-10	4.13E-10
3.00E-02	-6.58E-11	-8.81E-11	2.80E-01	3.18E-10	3.50E-10
4.00E-02	4.10E-11	4.19E-11	2.90E-01	2.86E-10	4.09E-10
5.00E-02	1.64E-10	1.72E-10	3.00E-01	3.33E-10	4.15E-10
6.00E-02	1.20E-10	6.59E-11	3.10E-01	4.54E-10	4.88E-10
7.00E-02	9.22E-11	1.50E-10	3.20E-01	4.74E-10	4.76E-10
8.00E-02	1.42E-10	2.20E-10	3.30E-01	4.30E-10	5.46E-10
9.00E-02	6.84E-11	1.54E-10	3.40E-01	5.55E-10	6.02E-10
1.00E-01	7.55E-11	9.05E-11	3.50E-01	4.92E-10	6.00E-10
1.10E-01	8.51E-11	2.19E-10	3.60E-01	4.34E-10	6.84E-10
1.20E-01	7.55E-11	1.94E-10	3.70E-01	3.98E-10	6.43E-10
1.30E-01	1.08E-10	2.11E-10	3.80E-01	4.43E-10	7.32E-10
1.40E-01	2.56E-10	1.46E-10	3.90E-01	5.36E-10	7.40E-10
1.50E-01	2.50E-10	2.25E-10	4.00E-01	6.91E-10	8.04E-10
1.60E-01	1.82E-10	1.11E-10	4.10E-01	8.14E-10	7.74E-10
1.70E-01	1.86E-10	1.87E-10	4.20E-01	7.27E-10	9.30E-10
1.80E-01	7.90E-11	1.38E-10	4.30E-01	7.16E-10	9.16E-10
1.90E-01	1.08E-10	2.20E-10	4.40E-01	8.02E-10	9.15E-10
2.00E-01	9.98E-11	2.05E-10	4.50E-01	8.78E-10	9.75E-10
2.10E-01	2.12E-10	1.64E-10	4.60E-01	1.09E-09	1.14E-09
2.20E-01	2.34E-10	2.19E-10	4.70E-01	1.20E-09	1.10E-09
2.30E-01	3.61E-10	2.89E-10	4.80E-01	1.37E-09	1.15E-09
2.40E-01	3.76E-10	3.40E-10	4.90E-01	1.50E-09	1.23E-09
			5.00E-01	1.45E-09	1.32E-09

Sample 2:

Voltage (V)	Current (A) (Before annealing)	Current (A) (After annealing)	Voltage (V)	Current (A) (Before annealing)	Current (A) (After annealing)

-5.29E-05	-2.13E-11	-7.60E-10	2.60E-01	4.04E-10	2.11E-06
9.95E-03	1.48E-10	3.55E-08	2.70E-01	4.88E-10	2.25E-06
2.00E-02	2.05E-10	7.53E-08	2.80E-01	4.05E-10	2.41E-06
3.00E-02	1.77E-10	1.19E-07	2.90E-01	4.41E-10	2.59E-06
4.00E-02	1.95E-10	1.67E-07	3.00E-01	5.05E-10	2.77E-06
5.00E-02	1.93E-10	2.19E-07	3.10E-01	5.08E-10	2.97E-06
6.00E-02	1.82E-10	2.75E-07	3.20E-01	5.31E-10	3.18E-06
7.00E-02	2.43E-10	3.34E-07	3.30E-01	5.88E-10	3.42E-06
8.00E-02	1.95E-10	3.96E-07	3.40E-01	5.61E-10	3.66E-06
9.00E-02	2.14E-10	4.61E-07	3.50E-01	6.20E-10	3.93E-06
1.00E-01	2.65E-10	5.29E-07	3.60E-01	6.20E-10	4.23E-06
1.10E-01	2.32E-10	6.00E-07	3.70E-01	6.38E-10	4.54E-06
1.20E-01	2.50E-10	6.73E-07	3.80E-01	7.01E-10	4.87E-06
1.30E-01	2.47E-10	7.47E-07	3.90E-01	7.51E-10	5.25E-06
1.40E-01	2.52E-10	8.26E-07	4.00E-01	7.27E-10	5.67E-06
1.50E-01	2.74E-10	9.07E-07	4.10E-01	7.76E-10	6.10E-06
1.60E-01	2.94E-10	9.90E-07	4.20E-01	7.68E-10	6.54E-06
1.70E-01	3.03E-10	1.08E-06	4.30E-01	8.27E-10	7.01E-06
1.80E-01	2.72E-10	1.17E-06	4.40E-01	8.91E-10	7.51E-06
1.90E-01	3.18E-10	1.26E-06	4.50E-01	8.97E-10	8.01E-06
2.00E-01	2.97E-10	1.37E-06	4.60E-01	9.17E-10	8.55E-06
2.10E-01	3.33E-10	1.47E-06	4.70E-01	9.69E-10	9.43E-06
2.20E-01	3.23E-10	1.58E-06	4.80E-01	1.02E-09	1.05E-05
2.30E-01	3.36E-10	1.70E-06	4.90E-01	1.03E-09	1.11E-05
2.50E-01	4.03E-10	1.96E-06	5.00E-01	1.08E-09	1.18E-05

Sample 3:

Voltage (V)	Current (A) (Before annealing)	Current (A) (After annealing)	Voltage (V)	Current (A) (Before annealing)	Current (A) (After annealing)
-2.86E-05	5.84E-11	3.99E-11	1.90E-01	7.01E-09	8.01E-09
9.96E-03	4.32E-10	1.94E-10	2.00E-01	7.78E-09	8.92E-09
2.00E-02	7.53E-10	4.12E-10	2.10E-01	8.39E-09	9.77E-09
3.00E-02	1.19E-09	6.72E-10	2.20E-01	9.23E-09	1.09E-08
4.00E-02	1.49E-09	8.57E-10	2.30E-01	1.00E-08	1.20E-08
5.00E-02	2.00E-09	1.11E-09	2.50E-01	1.22E-08	1.45E-08
6.00E-02	2.78E-09	1.43E-09	2.60E-01	1.33E-08	1.58E-08
7.00E-02	3.07E-09	1.73E-09	2.70E-01	1.48E-08	1.72E-08
8.00E-02	3.27E-09	1.95E-09	2.80E-01	1.61E-08	1.89E-08
9.00E-02	3.42E-09	2.34E-09	2.90E-01	1.77E-08	2.05E-08
1.00E-01	3.79E-09	2.72E-09	3.00E-01	1.96E-08	2.25E-08
1.10E-01	3.63E-09	3.15E-09	3.10E-01	2.20E-08	2.45E-08
1.20E-01	3.90E-09	3.63E-09	3.20E-01	2.45E-08	2.68E-08
1.30E-01	4.16E-09	4.02E-09	3.30E-01	2.68E-08	2.88E-08
1.40E-01	4.67E-09	4.58E-09	3.40E-01	2.93E-08	3.14E-08
1.50E-01	4.95E-09	5.19E-09	3.50E-01	3.22E-08	3.39E-08
1.60E-01	5.50E-09	5.70E-09	3.60E-01	3.58E-08	3.68E-08
1.70E-01	6.01E-09	6.43E-09	3.70E-01	3.95E-08	3.97E-08
1.80E-01	6.46E-09	7.21E-09	3.80E-01	4.37E-08	4.32E-08

3.90E-01	4.80E-08	4.68E-08	4.50E-01	8.22E-08	7.26E-08
4.00E-01	5.23E-08	5.04E-08	4.60E-01	9.13E-08	7.78E-08
4.10E-01	5.67E-08	5.44E-08	4.70E-01	9.86E-08	8.37E-08
4.20E-01	6.17E-08	5.87E-08	4.80E-01	1.08E-07	8.97E-08
4.30E-01	6.77E-08	6.30E-08	4.90E-01	1.17E-07	9.64E-08
4.40E-01	7.47E-08	6.77E-08	5.00E-01	1.29E-07	1.03E-07

Sample 4:

Voltage (V)	Current (A) (Before annealing)	Current (A) (After annealing)	Voltage (V)	Current (A) (Before annealing)	Current (A) (After annealing)
-3.67E-05	1.14E-11	-1.94E-10	2.60E-01	1.03E-10	1.09E-07
9.96E-03	2.43E-11	4.27E-09	2.70E-01	7.74E-11	1.15E-07
2.00E-02	-8.09E-12	8.50E-09	2.80E-01	1.25E-10	1.21E-07
3.00E-02	-1.80E-11	1.25E-08	2.90E-01	1.40E-10	1.27E-07
4.00E-02	4.07E-12	1.62E-08	3.00E-01	1.22E-10	1.34E-07
5.00E-02	-5.86E-12	1.98E-08	3.10E-01	1.01E-10	1.40E-07
6.00E-02	1.54E-11	2.33E-08	3.20E-01	1.85E-10	1.48E-07
7.00E-02	4.38E-11	2.67E-08	3.30E-01	1.65E-10	1.56E-07
8.00E-02	-3.02E-12	3.00E-08	3.40E-01	1.30E-10	1.63E-07
9.00E-02	4.93E-11	3.33E-08	3.50E-01	1.90E-10	1.71E-07
1.00E-01	5.86E-11	3.65E-08	3.60E-01	2.08E-10	1.80E-07
1.10E-01	5.25E-11	3.98E-08	3.70E-01	1.95E-10	1.87E-07
1.20E-01	7.31E-12	4.33E-08	3.80E-01	2.26E-10	1.95E-07
1.30E-01	6.22E-11	4.67E-08	3.90E-01	2.45E-10	2.05E-07
1.40E-01	5.68E-11	5.04E-08	4.00E-01	2.55E-10	2.14E-07
1.50E-01	3.06E-12	5.40E-08	4.10E-01	2.49E-10	2.24E-07
1.60E-01	6.16E-11	5.81E-08	4.20E-01	2.85E-10	2.33E-07
1.70E-01	2.43E-11	6.24E-08	4.30E-01	3.19E-10	2.42E-07
1.80E-01	6.41E-11	6.66E-08	4.40E-01	3.00E-10	2.52E-07
1.90E-01	5.17E-11	7.14E-08	4.50E-01	3.33E-10	2.65E-07
2.00E-01	6.69E-11	7.65E-08	4.60E-01	3.65E-10	2.74E-07
2.10E-01	2.74E-11	8.16E-08	4.70E-01	3.60E-10	2.84E-07
2.20E-01	6.89E-11	8.67E-08	4.80E-01	3.94E-10	2.94E-07
2.30E-01	5.39E-11	9.21E-08			3.02E-07
2.40E-01	6.85E-11	9.67E-08			3.13E-07

Sample 5:

Voltage (V)	Current (A) (Before annealing)	Current (A) (After annealing)	Voltage (V)	Current (A) (Before annealing)	Current (A) (After annealing)
-5.36E-05	3.89E-11	-3.24E-11	7.00E-02	1.73E-09	6.07E-08
9.95E-03	1.95E-10	1.22E-08	8.00E-02	2.10E-09	6.97E-08
2.00E-02	2.91E-10	2.03E-08	9.00E-02	2.48E-09	7.68E-08
3.00E-02	5.30E-10	2.81E-08	1.00E-01	3.25E-09	8.92E-08
4.00E-02	7.03E-10	3.60E-08	1.10E-01	3.60E-09	1.00E-07
5.00E-02	9.91E-10	4.39E-08	1.20E-01	4.68E-09	1.12E-07
6.00E-02	1.31E-09	5.21E-08	1.30E-01	5.01E-09	1.24E-07

1.40E-01	5.85E-09	1.38E-07	3.30E-01	2.64E-08	5.98E-07
1.50E-01	6.80E-09	1.52E-07	3.40E-01	2.83E-08	6.31E-07
1.60E-01	7.66E-09	1.67E-07	3.50E-01	2.96E-08	6.65E-07
1.70E-01	8.10E-09	1.84E-07	3.60E-01	3.16E-08	7.00E-07
1.80E-01	9.15E-09	1.99E-07	3.70E-01	3.30E-08	7.36E-07
1.90E-01	1.00E-08	2.20E-07	3.80E-01	3.53E-08	7.73E-07
2.00E-01	1.04E-08	2.40E-07	3.90E-01	3.67E-08	8.08E-07
2.10E-01	1.13E-08	2.62E-07	4.00E-01	3.82E-08	8.42E-07
2.20E-01	1.28E-08	2.83E-07	4.10E-01	3.91E-08	8.80E-07
2.30E-01	1.44E-08	3.07E-07	4.20E-01	4.13E-08	9.16E-07
2.40E-01	1.51E-08	3.31E-07	4.30E-01	4.25E-08	9.50E-07
2.60E-01	1.71E-08	3.84E-07	4.40E-01	4.65E-08	9.85E-07
2.70E-01	1.80E-08	4.10E-07	4.50E-01	4.71E-08	1.02E-06
2.80E-01	1.98E-08	4.41E-07	4.60E-01	5.09E-08	1.05E-06
2.90E-01	2.14E-08	4.70E-07	4.70E-01	5.33E-08	1.08E-06
3.00E-01	2.29E-08	5.01E-07	4.80E-01	5.55E-08	1.12E-06
3.10E-01	2.40E-08	5.33E-07	4.90E-01	5.72E-08	1.15E-06
3.20E-01	2.54E-08	5.65E-07	5.00E-01	5.87E-08	1.18E-06

Sample 6:

Voltage (V)	Current (A) (Before annealing)	Current (A) (After annealing)	Voltage (V)	Current (A) (Before annealing)	Current (A) (After annealing)
-2.65E-05	2.04E-12	-5.33E-11	2.40E-01	6.67E-09	3.91E-08
9.94E-03	8.36E-11	1.40E-09	2.60E-01	8.75E-09	4.42E-08
2.00E-02	2.25E-10	2.83E-09	2.70E-01	9.89E-09	4.60E-08
3.00E-02	3.70E-10	4.26E-09	2.80E-01	1.17E-08	4.88E-08
4.00E-02	4.52E-10	5.45E-09	2.90E-01	1.27E-08	5.19E-08
5.00E-02	5.91E-10	6.82E-09	3.00E-01	1.27E-08	5.47E-08
6.00E-02	7.41E-10	8.34E-09	3.10E-01	1.30E-08	5.83E-08
7.00E-02	9.28E-10	9.55E-09	3.20E-01	1.60E-08	6.16E-08
8.00E-02	1.09E-09	1.10E-08	3.30E-01	1.70E-08	6.42E-08
9.00E-02	1.26E-09	1.24E-08	3.40E-01	2.45E-08	6.64E-08
1.00E-01	1.67E-09	1.38E-08	3.50E-01	2.17E-08	6.95E-08
1.10E-01	1.70E-09	1.52E-08	3.60E-01	2.42E-08	7.31E-08
1.20E-01	2.01E-09	1.68E-08	3.70E-01	2.74E-08	7.88E-08
1.30E-01	2.23E-09	1.81E-08	3.80E-01	3.20E-08	7.86E-08
1.40E-01	2.40E-09	1.97E-08	3.90E-01	2.77E-08	8.40E-08
1.50E-01	2.92E-09	2.14E-08	4.00E-01	4.72E-08	8.87E-08
1.60E-01	3.25E-09	2.32E-08	4.10E-01	5.91E-08	9.21E-08
1.70E-01	3.33E-09	2.51E-08	4.20E-01	6.85E-08	9.39E-08
1.80E-01	4.49E-09	2.70E-08	4.30E-01	7.58E-08	9.88E-08
1.90E-01	4.77E-09	2.87E-08	4.40E-01	6.11E-08	1.02E-07
2.00E-01	5.25E-09	3.05E-08	4.50E-01	5.87E-08	1.06E-07
2.10E-01	5.74E-09	3.26E-08	4.60E-01	5.24E-08	1.08E-07
2.20E-01	6.21E-09	3.46E-08	4.70E-01	7.92E-08	1.11E-07
2.30E-01	6.39E-09	3.68E-08	4.80E-01	7.84E-08	1.16E-07
			4.90E-01	7.60E-08	1.20E-07
			5.00E-01	5.40E-08	1.23E-07

Sample 7:

Voltage (V)	Current (A) (Before annealing)	Current (A) (After annealing)	Voltage (V)	Current (A) (Before annealing)	Current (A) (After annealing)
-4.95E-05	-1.17E-07	-6.67E-13	2.60E-01	1.09E-04	1.08E-07
9.95E-03	4.10E-06	2.84E-09	2.70E-01	1.14E-04	1.09E-07
2.00E-02	8.31E-06	5.38E-09	2.80E-01	1.18E-04	1.17E-07
3.00E-02	1.25E-05	8.19E-09	2.90E-01	1.22E-04	1.21E-07
4.00E-02	1.67E-05	1.15E-08	3.00E-01	1.26E-04	1.26E-07
5.00E-02	2.10E-05	1.62E-08	3.10E-01	1.31E-04	1.31E-07
6.00E-02	2.52E-05	1.96E-08	3.20E-01	1.35E-04	1.39E-07
7.00E-02	2.94E-05	2.36E-08	3.30E-01	1.39E-04	1.47E-07
8.00E-02	3.36E-05	2.67E-08	3.40E-01	1.43E-04	1.51E-07
9.00E-02	3.78E-05	3.02E-08	3.50E-01	1.47E-04	1.58E-07
1.00E-01	4.20E-05	3.37E-08	3.60E-01	1.52E-04	1.70E-07
1.10E-01	4.62E-05	3.71E-08	3.70E-01	1.56E-04	1.83E-07
1.20E-01	5.04E-05	4.10E-08	3.80E-01	1.60E-04	1.85E-07
1.30E-01	5.46E-05	4.40E-08	3.90E-01	1.64E-04	1.91E-07
1.40E-01	5.89E-05	4.76E-08	4.00E-01	1.68E-04	1.99E-07
1.50E-01	6.31E-05	5.24E-08	4.10E-01	1.73E-04	2.06E-07
1.60E-01	6.73E-05	5.58E-08	4.20E-01	1.77E-04	2.13E-07
1.70E-01	7.15E-05	6.06E-08	4.30E-01	1.81E-04	2.17E-07
1.80E-01	7.57E-05	6.26E-08	4.40E-01	1.85E-04	2.28E-07
1.90E-01	7.99E-05	6.87E-08	4.50E-01	1.90E-04	2.34E-07
2.00E-01	8.41E-05	7.37E-08	4.60E-01	1.94E-04	2.36E-07
2.10E-01	8.84E-05	8.20E-08	4.70E-01	1.98E-04	2.39E-07
2.20E-01	9.26E-05	8.80E-08	4.80E-01	2.02E-04	2.45E-07
2.30E-01	9.68E-05	9.13E-08			2.54E-07
2.40E-01	1.01E-04	9.57E-08			2.55E-07

Sample 8:

Voltage (V)	Current (A) (Before annealing)	Current (A) (After annealing)	Voltage (V)	Current (A) (Before annealing)	Current (A) (After annealing)
-4.61E-05	-5.05E-12	-7.20E-07	1.40E-01	5.88E-09	3.91E-04
9.95E-03	1.30E-10	2.72E-05	1.50E-01	6.83E-09	4.19E-04
2.00E-02	4.49E-10	5.52E-05	1.60E-01	8.06E-09	4.47E-04
3.00E-02	6.38E-10	8.33E-05	1.70E-01	9.42E-09	4.75E-04
4.00E-02	7.97E-10	1.11E-04	1.80E-01	1.11E-08	5.03E-04
5.00E-02	1.09E-09	1.39E-04	1.90E-01	1.30E-08	5.32E-04
6.00E-02	1.44E-09	1.67E-04	2.00E-01	1.50E-08	5.60E-04
7.00E-02	1.75E-09	1.95E-04	2.10E-01	1.74E-08	5.88E-04
8.00E-02	2.09E-09	2.23E-04	2.20E-01	2.05E-08	6.16E-04
9.00E-02	2.59E-09	2.51E-04	2.30E-01	2.36E-08	6.44E-04
1.00E-01	3.12E-09	2.79E-04	2.40E-01	2.73E-08	6.72E-04
1.10E-01	3.66E-09	3.07E-04	2.60E-01	3.68E-08	7.28E-04
1.20E-01	4.28E-09	3.35E-04	2.70E-01	4.22E-08	7.56E-04

2.80E-01	4.89E-08	7.84E-04	4.00E-01	2.02E-07	1.00E-03
2.90E-01	5.57E-08	8.13E-04	4.10E-01	2.21E-07	1.00E-03
3.00E-01	6.36E-08	8.41E-04	4.20E-01	2.42E-07	1.00E-03
3.10E-01	7.23E-08	8.69E-04	4.30E-01	2.64E-07	1.00E-03
3.20E-01	8.16E-08	8.97E-04	4.40E-01	2.91E-07	1.00E-03
3.30E-01	9.26E-08	9.25E-04	4.50E-01	3.22E-07	1.00E-03
3.40E-01	1.05E-07	9.53E-04	4.60E-01	3.51E-07	1.00E-03
3.50E-01	1.17E-07	9.82E-04	4.70E-01	3.75E-07	1.00E-03
3.60E-01	1.31E-07	1.00E-03	4.80E-01	4.05E-07	1.00E-03
3.70E-01	1.46E-07	1.00E-03			1.00E-03
3.80E-01	1.65E-07	1.00E-03			1.00E-03
3.90E-01	1.83E-07	1.00E-03			

APPENDIX C

Oxygen, nitrogen and hydrogen diffusivity

Table below is copy from: http://www.diffusion-polymers.com/Gas%20Diffusion.htm

gas diffusion & industrial cases

See table below for some diffusion figures of gaseous permeants in polymers. This is a small selection of our total available experimental figures, for specific figures click: support. To read an interesting example of the industrial application of the tabled figures, click: INDUSTRIAL CASE.

Gas Diffusion Table						
Experimental Conditions	Temperature:		25 degrees Celsius (298 Kelvin)		Figures are applicable at 298 Kelvin and in the range of 0.1 - ~ 3 Bar. Please contact us for other process conditions.	
	Pressure:		1 Bar (1 E5 Pa)			
	Activity of Permeant		1			
Polymer	Permeant	Solubility	Diffusivity	Alpha*	Permeability**	
[-]	[-]	m3 stp / m3 x bar	m2 / s	[-]	[m3 stp / m3 x bar] x [m2/s]	gram / m s
PET (Poly Ethylene Terephthalate)	CO2	1.4	5.4 E-14	-	7.6 E-14	1.5 E-10
	O2	0.091	5.6 E-13	-	5.1 E-14	7.2 E-11
	N2	0.032	1.4 E-13	-	3.6 E-15	4.4 E-12
	H2	0.081	8.0 E-12	-	6.4 E-13	5.7 E-11
PP (Poly Propylene)	CO2	0.17	1.4 E-11	-	2.4 E-12	4.7 E-9
	O2	0.029	2.5 E-11	-	7.4 E-13	1.0 E-9
	N2	0.17	1.1 E-12	-	1.9 E-13	2.3 E-10
HDPE (High Density Poly Ethylene)	CO2	0.29	1.2 E-11	-	3.5 E-12	6.8 E-9
	O2	0.046	1.7 E-11	-	7.8 E-13	1.1 E-9

	H2	0.073	2.6 E-11	-	1.9 E-12	1.7 E-10
LDPE (Low Density Poly Ethylene)	CO2	0.25	3.7E-11	-	9.4 E-12	1.8 E-8
	O2	0.050	4.6 E-11	-	2.3 E-12	3.2 E-9
	N2	0.021	3.2 E-11	-	6.4 E-13	7.9 E-10
	H2	0.16	4.7 E-11	-	7.6 E-12	6.8 E-10
PC (Poly Carbonate)	CO2	5.0	9.6 E-13	-	4.8 E-12	9.3 E-9
	O2	0.36	4.2 E-12	-	1.5 E-12	2.1 E-9
	N2	0.077	2.6 E-12	-	2.0 E-13	2.5 E-10
PS (Poly Styrene)	CO2	0.80	5.8 E-12	-	4.6 E-12	8.9 E-9
	O2	0.15	1.1 E-11	-	1.7 E-12	2.4 E-9
	N2	0.021	9.6 E-12	-	2.0 E-13	2.5 E-10
PVC (Poly Vinyl Chloride)	CO2	0.47	2.5 E-13	-	1.2 E-13	2.4 E-10
	O2	0.029	1.2 E-12	-	3.5 E-14	4.9 E-11
	N2	0.023	3.8 E-13	-	8.7 E-15	1.1 E-11
	H2	0.026	5.0 E-11	-	1.3 E-12	1.2 E-10
Butyl Rubber (Poly Isobutylene, used for inner tubes, etc.)	CO2	0.67	5.8 E-12	-	3.9 E-12	7.9 E-9
	O2	0.12	8.1 E-12	-	9.7 E-13	1.4 E-9
	N2	0.054	4.5 E-12	-	2.4 E-13	3.0 E-10
	H2	0.035	1.5 E-10	-	5.3 E-12	4.7 E-10

* Alpha is an empirical Fickian plasticizing factor.

The Fickian diffusivity follows from: D = D0 x EXP (permeant volume fraction / alpha).